Alma Mater Studiorum - Università di Bologna

DOTTORATO DI RICERCA IN

INGEGNERIA BIOMEDICA, ELETTRICA E DEI SISTEMI

Ciclo 34

Settore Concorsuale: 09/E4 - MISURE

Settore Scientifico Disciplinare: ING-INF/07 - MISURE ELETTRICHE E ELETTRONICHE

METROLOGICAL CHARACTERIZATION OF SENSORS AND INSTRUMENTATION FOR DISTRIBUTION GRID MONITORING AND ELECTRICAL ASSET DIAGNOSTICS

Presentata da: Diego Cavaliere

Coordinatore Dottorato

Michele Monaci

Supervisore

Gaetano Pasini

Co-supervisore

Lorenzo Peretto

Esame finale anno 2022

Index

List of Figures

List of Tables

List of Acronyms

AC	Alternate Current
ADC	Analog-to-Digital Converter
AWG	Arbitrary Waveform Generator
CLT	Central Limit Theorem
DAC	Digital-to-Analog Converter
DAQ	Data Acquisition Board
DC	Direct Current
DFT	Discrete Fourier Transform
DMM	Digital Multimeter
DSO	Distribution System Operator
DSP	Digital Signal Processor
DT	Digital Twin
EM	Energy Meter
EMS	Energy Management System
EMUT	Energy Meter under test
FE	Frequency Error
GUM	Guide to the expression of uncertainty in measurement
HIL	Hardware-in-the-Loop
HV	High Voltage
IT	Instrument Transformer
ICT	Inductive Current Transformer
IIT	Inductive Instrument Transformer
IVT	Inductive Voltage Transformer
LPIT	Low-Power Instrument Transformer
LV	Low Voltage
MC	Monte Carlo
MID	Measuring Instruments Directive
MV	Medium Voltage
PCC	Point of Common Coupling
PLL	Phase-Locked Loop
PDF	Probability Density Function
PMS	Pole-Mounted Acquisition System
PMU	Phasor Measurement Unit
PPS	Pulse Per Second
RFE	Rate of Change of Frequency Error
RMS	Root Mean Square
ROCOF	Rate of Change of Frequency
RTS	Real-Time Simulator
SA	Surge Arrester
SE	State Estimation
THD	Total Harmonic Distortion
TUT	Transformer under test
TVE	Total Vector Error
UAV	Unmanned Aerial Vehicle
UTC	Coordinated Universal Time

Introduction

The present dissertation collects the main research activities carried out during my 3-year Ph.D. program and their results. The dissertation's subject is related to the role of the measurements applied to the modern power systems' issues. The ambition is to cover different measurement application fields: both the distribution grid monitoring and the electrical assets diagnostics. In particular, the overarching theme is the metrological characterization of sensors and instrumentation applied in these contexts, attempting to add something new to the existing scientific literature. The modern power networks already need a large amount of information to be operated and day by day new information is required to improve the operation performance. Moreover, it is also fundamental that the available information is reliable and accurate. Therefore, the role of metrology is crucial. Hence, understanding better the sensors and the instrumentation employed by the power system operators and studying new solutions are justified. The dissertation is organized in five chapters, which are briefly described. The first chapter introduces the "Smart Grid" concept, which is the paradigm followed by the modern power systems. It is discussed how the role of the measurements is strictly linked both with this concept and its development, since they actively contribute to the monitoring of the grid and its assets. Moreover, in Chapter 1 are presented some notions regarding the main issues that constitute a challenge for the effectiveness and the reliability of the distribution power system operations, such as the outdoor electrical assets degradation, the power quality disturbances, and the grid state monitoring: these issues are the ones that have primarily driven my research activity. In Chapter 2, the sensors and the instrumentation mostly involved in the metrological characterization studies of this dissertation are described, such as instrument transformers, energy meters and phasor measurement units. Chapter 3 reports the main concepts of metrology, presenting the methodology employed to evaluate the measurement uncertainty in the whole research work. After that, Chapter 4 and Chapter 5 are the core of the dissertation. In Chapter 4, the research on the measurement applied to the electrical asset diagnostics is presented. An innovative drone-based measurement system is proposed for monitoring medium voltage surge arresters. This system is described, the tests, and its metrological characterization are presented. Chapter 5, instead, deals with the research regarding the measurements applied to the grid monitoring and it is made of three parts. The first part concerns the metrological characterization of the low-voltage electronic energy meters' operation under off-nominal power conditions. Original test procedures have been designed for both frequency and harmonic distortion as influence quantities, aiming at defining realistic scenarios. Consequently, the tests have been performed to assess whether the energy meters' performance is affected by these conditions, using the percentage error index. The second part deals with medium voltage inductive current transformers. An in-depth investigation on their accuracy behavior in presence of current distortion is carried out, by acquiring realistic waveforms from the network and applying them to these sensors. The composite error index and its approximated version have been employed for this

analysis. Based on the same test setup, a closed-form expression for the measured current total harmonic distortion uncertainty estimation has been experimentally validated. The metrological characterization of a virtual phasor measurement unit is the subject of the third and last part: first, a calibrator has been designed and the uncertainty associated with its steady-state reference phasor in different conditions has been evaluated coherently with the relevant standard; then, this calibrator acted as a reference, and it has been used to thoroughly characterize the phasor measurement unit implemented within a real-time simulator. Finally, the dissertation ends with the conclusions that can be drawn from the overall research work.

Chapter 1 Distribution Power Network Monitoring and Measurements

In this Chapter, a brief presentation of the modern distribution networks is given, focusing especially on the issues that justify the need and the implementation of monitoring and measurement apparatuses. First, a basic overview of the Smart Grid concept is introduced; after that, some of the relevant problems and challenges faced in the distribution power systems management are described. These elements provide the reader with the context and the reasons supporting the research work presented in Chapter 4 and Chapter 5.

1.1 The Modern Power Network: "Smart Grid"

In recent years the power systems have been evolving towards a totally new paradigm, if compared to the 20th-century concept. Powerful drivers such as the information and communication technologies, the network operators' asset management objectives, the decarbonization and ecological policies are pushing this transformation [1]. The ultimate goal is the so-called "Smart Grid" vision. Several definitions of Smart Grid can be found, since it is a rich set of different aspects [1]–[4]. The definition chosen by the European Commission [4] is: *"a Smart Grid is an electricity network that can cost efficiently integrate the behavior and actions of all users connected to it – generators, consumers and those that do both – in order to ensure economically efficient, sustainable power system with low losses and high levels of quality and security of supply and safety"*. Moreover, a concise but effective comparison between the Smart Grid and the traditional grid implementation paradigms is summarized in Table 1.1 [2].

Table 1.1 Smart Grid vs traditional grid implementation paradigms.

Traditional Grid	**Smart Grid**
Electromechanical	Digital
One-way communication	Two-way communication
Centralized generation	Distributed generation
Few sensors	Sensors throughout
Manual monitoring	Self-monitoring
Manual restoration	Self-healing
Failures and blackouts	Adaptive and islanding
Limited control	Pervasive control
Few customer choices	Many customer choices

Different listings of the Smart Grid objectives are proposed as well. However, all of them agree on the following aspects: i) reducing the environmental impact of the entire power system; ii) improving the reliability and safety of the system and quality of the service; iii) enabling the transition to distributed energy resources and fostering new technologies; iv) involving the consumers as active players in the energy market and raising awareness of their role in the power grid operation. Many considerations could be made on the Smart Grid definition, since it is evident the large number of the involved branches of knowledge that are required to interact among each other. However, the point of view adopted in the present dissertation is the asset managers' and power system operators' one. In other words, how to have awareness of the distribution network operating status by means of a smart infrastructure, in order to deliver a high-quality energy service, and at the same time keeping the running costs acceptable? The fast rise of distributed energy sources, electric vehicles and charger stations, and the overall growth of the electric power demand, while a lot of legacy grid infrastructures are still present, make the challenge harder:

- two-way power flows, scarcely programmable distributed renewable-energy generation plants characterized by low inertia hinder the grid stability.
- electronic loads contaminate the electric power quality, especially in the electric vehicle case, where large amount of power can be suddenly absorbed.
- ageing and degradation of the existing assets lead to failures and unavailability of the service.

To face these issues the solution is the synergy among measurements, telecommunications, and control automations. In this way it is possible to: i) remotely get reliable information about the health and the state variables of the overall system; ii) elaborate the information, providing useful data as input for both the control algorithms and management; iii) finally, maintain and remotely operate the grid accordingly.

1.1.1 The Role of Measurements in the Smart Grid

It follows that the influence of the electrical measurement applications on the Smart Grid development is crucial and they deserve thorough research [5], [6]. In fact, a power system required to automatically monitor and control itself not only needs a widespread presence of sensors and measuring instruments deployed across the grid, but they must be properly calibrated, granting suitable-quality measurement results. In this context, two categories of measurements could be identified, according to their final application: measurements for the diagnostics and the measurements for the grid monitoring. The aim of the measurements for the diagnostics is providing the electrical technology expert with pieces of information useful for inferring the health status and possibly the residual life estimate of the electrical asset installed across the grid (i.e., transformers, surge arresters, switchgears, cable insulation, cable joints, etc.). While the aim of the measurements for the grid monitoring is strictly supplying electrical measurement (voltages, currents, phase angles, energies, etc.) as

input for actuators and power system control algorithms, which perform almost real-time analysis of the grid state to keep its stability and promptly react to anomalies, such as faults. A glaring example of the applied measurements for the Smart Grid, is the smart metering infrastructure. It consists of a huge number of revenue energy meters, installed at strategic nodes (e.g., customer connection points, substations, etc.) and, among other functionalities, they transmit the measured data for billing to the system operators' data concentrators. The uncertainty affecting the transmitted energy measurements directly translates into financial uncertainty [6], other than lack of knowledge in the decision-making algorithms employed in the power grid control rooms. Consequently, the measurement chain composed of sensors and instrumentation shall be characterized with a well-established uncertainty. Moreover, it is not sufficient to conduct the metrological characterization study in the so-called "reference conditions", but also in conditions where different influence quantities are present, which are not uncommon in real-world scenarios.

1.2 Distribution Power Network Issues

In this Section, a deeper focus on some of the main distribution power network issues continuously confronted by the system operators is presented. The choice fell on the problems directly linked to the electrical assets and grid state monitoring, where the metrology expert contribution can really tip the balance thanks to proper measurement systems design and characterization. First, an overview on the degradation and diagnostics of outdoor electrical assets is given; second, some of the main power quality phenomena and their consequences are discussed, referring also to the main related standards; finally, the principal grid state monitoring operations are recalled and the link with the metrological performance of the sensors and instrumentation is underlined.

1.2.1 Electrical Assets Degradation and Diagnostics

The system operators need to manage the assets composing the energy distribution infrastructure. Often these are installed in outdoor environment and in remote rural areas (e.g., pole-mounted transformers and switchgears, insulators, overvoltage suppressors, etc.), but also in difficult-to-reach locations, such as underground cables and cable joints. If one component abruptly fails, it could cause a service unavailability, causing economic loss to the interrupted customers. The energy regulatory authorities[1] are called to oversee the electrical energy market to foster it, guaranteeing competitiveness and quality of service on behalf of the

[1] The Italian authority is called Autorità di Regolazione per Energia Reti e Ambiente (ARERA). The European authorities cooperate within the Council of European Energy Regulators (CEER), aiming to a competitive and sustainable European energy market.

system operators. Since the availability of the service is fundamental, the system operators are incentivized to invest on good asset management practices, namely, the diagnostics and preventive maintenance.

Concerning the outdoor infrastructures, they are inevitably subjected for long periods to stress due to factors typical of the place in which they are located. These factors are of various nature, but they can be divided into two categories: the environmental ones and meteorological ones. The former are related to the contact with elements such as flora, fauna, and contaminants. The latter are essentially agents such as wind, ice, heat, direct lightning strikes and humidity. Taken together, these elements can both directly cause faults that require immediate intervention (e.g., tree falling on a live line) and accelerate the aging process of the infrastructures (e.g., deposit of contaminants on insulators and consequent ignition of discharges). Some examples of outdoor components of the distribution network and the mechanisms that can lead to faults are:

- The conductors of the lines, typically stranded, are subjected to: direct lightning strikes possibly causing alterations of the strands and eventually cracking them; corrosion, triggered by humidity and pollutants (true for aluminum-steel conductors) [7]; mechanical fatigue, due both to the oscillatory motions forced by the wind [8], [9], and to the load of the weight of the ice that can form around the conductors.
- The insulators can be subject to: overvoltages caused by lightning strikes; thermal and mechanical cycles which, by weakening the insulator structure, prompt the creation of cracks in which moisture and other substances can penetrate, compromising the reliability. In addition, the deposit of contaminants (sand, salt, industrial pollutants) together with humidity, can reduce considerably the surface resistance, thus inducing the triggering of discharges that can damage the insulator itself [10], [11]. Finally, some failures are caused by more unexpected external factors, such as biological agents, fauna, and vandalism.
- The pole-mounted transformers are step-down medium-voltage (MV) to low-voltage (LV) transformers located approximately at the level of the power lines, fixed on special poles or platforms. After a near lightning strike event, the induced impulsive overvoltage could determine insulation failure [12]. Being placed outdoors, some failure mechanisms may be more frequent than in the case of indoor installations. For example: cracks on the casing resulting in oil leaks, damage to critical external components such as bushing, loose and/or corroded electrical connections.
- The pole-mounted switchgears, as well as the isolators, fail due to surface and corona discharges eased by the deposit of contaminants on the surface [13]. In addition, failures caused by loose contacts and rusty components are not uncommon [14].
- The wooden poles are subject to decay phenomena, metal structures can corrode or lose mechanical fasteners (e.g., bolts). These degradation mechanisms must be identified promptly

both to prevent the live line and/or equipment mounted on the structure from falling to the ground, and to avoid dangers for the safety of linemen when they carry out operations working at height.

- The metal-oxide surge arresters are made of metal-oxide disks which are fit into a polymeric or porcelain enclosure, typically installed close to the MV side of the distribution transformers to protect them from potentially dangerous overvoltages. As for the insulators, superficial deposits of contaminants can trigger flashovers and the enclosure, especially the polymeric ones, are sensitive to the environmental stress. Nevertheless, the major threat is when a failure affects the metal-oxide disks, which are not visible from the outside. In fact, in these conditions, overvoltages would directly hit the transformer.

To prevent failures that could cause the interruption of the service, it is necessary to conduct an effective preventive monitoring activity. But it can be observed that to carry out a widespread control of these devices, it would be necessary to install monitoring systems for each component across the network. However, an overhead network can cover thousands of kilometers and such a solution would not be practical and cost effective. Therefore, it is inevitable to send linemen crews to conduct targeted on-site inspections. The visual observation allows the quick identification of anomalies along the line: broken insulators, compromised mechanical components, vegetation close to energized conductors, external damage to transformers, and switchgears, etc. It is also common to use other measuring instruments that allow rapid checks, such as thermal imaging cameras and ultraviolet cameras [10], [15]. Through thermography it is possible to identify situations such as altered joints and connections, currents on insulators, surge arresters' defects, low oil level in transformers, etc. On the other hand, the observation of the ultraviolet spectrum allows the identification of surface discharges and the corona effect. In the specific case of the surge arresters, the leakage current flowing towards ground under normal operation could be monitored to gain information on the device's health. The most common ways of conducting the inspections are the ground-based or flight inspections [16], [17]. The ground-based inspections consist in linemen crews who, on foot or by land vehicles, move along the stretch of the line to be examined. Conversely, the flight inspection is traditionally conducted by means of helicopters, which allows the on-board expert technicians to observe from a close distance the electrical infrastructures. However, both solutions have drawbacks. The need to inspect long line segments from the ground is critical for linemen: the lines often extend across rough and difficult-to-access terrains. Hence, they find themselves moving on foot on uneven grounds, which is a difficult working condition that can compromise the outcome of the inspection itself. The helicopter inspections, other than being expensive and not always feasible (e.g., presence of inhabited areas and livestock), are risky for the safety of the crew: in fact, an effective inspection requires a low-speed low-height flight in proximity of the live lines.

In recent years, Unmanned Aerial Vehicles (UAVs), also known as drones, have gained increasing popularity in civilian applications as well as in military ones [18]. This fact is not surprising, since the UAVs are suitable for a large number of operations in which the action of man or traditional aircraft is risky and/or inefficient. Consequently, using UAVs for remote sensing activities aimed at monitoring the power lines seems a smart technological solution. In [19] it is indicated that UAV-based inspections are faster than ground inspections and that it can provide results with similar or better quality than those deriving from more expensive helicopter inspections. The system operators have already shown real interest in this innovative approach, as documented by the presence of case studies [20] and pilot trials (in Italy, e-distribuzione has recently started to use UAVs [21]). Work on this topic has been done and it is reported in Chapter 4.

1.2.2 Power Quality

The power quality topic cannot be neglected with the intention of discussing the importance of measurements in the modern power network. In fact, the spread of the distributed energy resources and electronic devices cause disturbances to the voltage and current at the nodes, inducing deviations from the rated parameters. Moreover, the customers are progressively more interested in the power quality that they can expect from the system operators and the latter, in turn, know that the power quality disturbances have consequences on the network management, since they affect the electrical assets, the connected loads and the measuring apparatuses. Therefore, it is of paramount importance both accurately detect these phenomena and performing accurate measurements when the disturbances are just influence quantities. A very common type of disturbance is the harmonic distortion. The non-linear loads, such as electric drives and all the system containing static power converters, absorb non-sinusoidal currents even though a sinusoidal voltage is supplied. When the current draw become relevant, this can even result in a voltage distortion at the point of common coupling (PCC). The current harmonic distortion can produce excessive heating of the electrical assets, while voltage distortion can increment the electric field stress on the assets, reducing their designed life [22], [23]. Hence, it is crucial to accurately measure voltages and currents in these conditions. However, care must be taken to ensure that the sensors and the instrumentation are able to effectively transduce and measure also the distorted waveforms. In fact, this is not obvious, and it can depend on many factors. One of them it is the device physical nature (as in the sensors case), but also the measurement algorithm implementation constitutes a limit, as far as the digital instrumentation is concerned. All these elements explain why a cautious metrological characterization is needed.

To prevent excessive “pollution” of the voltages and currents across the network, several technical standards have been issued by different organizations covering the power-quality-related problems from different points of view. In this dissertation, the standard EN 50160 [24] and the standard IEEE Std 519 [25]

have been used as a reference for the metrological characterization activities presented in the following Chapters, since they point out useful knowledge regarding the expected disturbance scenarios. Below an overview of the relevant contents is presented.

1.2.2.1 EN 50160 Standard

The CENELEC's standard EN 50160 [24] is titled "Voltage characteristics of electricity supplied by public electricity networks". The latest version has been released in 2010 with the latest amendment published in 2019. The standard prescribes the limits of many different power quality disturbance phenomena that can affect the transmission and the distribution networks. Since the present dissertation deals with distribution networks only, the requirements concerning high-voltage (HV) networks are ignored. The rated voltage and frequency values for LV and MV systems are summarized in Table 1.2

Table 1.2 Voltage and frequency rated values for LV and MV networks according to EN 50160.

	LV	MV
Frequency [Hz]	50	50
Voltage [V]	230	1000 ÷ 36000

The disturbance phenomena are classified as: "continuous phenomena", if the deviations from the nominal value occur continuously over time; or "voltage events", if the deviation from the nominal waveshape are significant and sudden. The summary of all the typologies of the disturbance phenomena is given in Table 1.3.

Table 1.3 Disturbance phenomena classification in LV/MV networks according to EN 50160.

Continuous Phenomena	Voltage Events
• Power frequency variations • Supply voltage variations • Rapid voltage changes • Supply voltage unbalance • Harmonic voltage • Interharmonic voltage • Mains signalling voltage[2]	• Interruptions of the supply voltage • Supply voltage dips and swells • Transient overvoltages • Mains communication voltages

[2] It applies only to MV networks.

Given the importance of the power frequency variations and the harmonic voltage magnitude in the metrological analysis conducted in the next Chapters, detailed information on the EN 50160 standard's prescription regarding these two continuous phenomena are reported in the following. Concerning the constraints on the power frequency variations, they are the same for LV and MV systems and are listed in Table 1.4.

Table 1.4 Power frequency variations limits for LV/MV networks according to EN 50160.

Systems with synchronous connection to an interconnected system:	
50 Hz ± 1 % 50 Hz + 4 % / - 6 %	during 99.5 % of a year. during 100 % of the time.
Systems with no synchronous connection to an interconnected system:	
50 Hz ± 2 % 50 Hz ± 15 %	during 99.5 % of a year. during 100 % of the time.

Table 1.4 shows that more allowance is given to frequency variations in systems isolated from the mainland networks and, consequently, characterized by low inertia. With respect to the harmonic voltage magnitude limitations, the EN 50160 standard identifies a limit for each harmonic component, as listed in Table 1.5 for both MV and LV networks. The h stands for the harmonic component order number, while u_h represents the harmonic voltage component RMS normalized by the fundamental power frequency component.

Table 1.5 Normalized harmonic voltage limits for LV/MV networks according to EN 50160.

Odd Harmonics				Even Harmonics	
Not multiples of 3		Multiples of 3			
h [-]	u_h [%]	h [-]	u_h [%]	h [-]	u_h [%]
5	6.0	3	5.0	2	2.0
7	5.0	9	1.5	4	1.0
11	3.5	15	1.0[3], 0.5[4]	6 … 24	0.5
13	3.0	21	0.75		
17	2.0				
19	1.5				
23	1.5				
25	1.5				

[3] It applies to LV networks.
[4] It applies to MV networks.

The limitations apply for the 95 % of the week. The analysis of harmonic content is often conducted "globally" by considering all the components together and summarized in the total harmonic distortion (*THD*) index:

$$THD = \sqrt{\sum_{h=2}^{h_{max}} (x_h)^2}, \tag{1.1}$$

where, h_{max} is the highest harmonic order considered and $x_h = u_h$. The THD shall be less than or equal to 8 %. The standard does not consider the harmonic orders above the 40th (i.e., usually h_{max}= 40) and it prescribes limitations only up to the 25th order. The knowledge on the phenomena populating the frequency range between 2 kHz and 150 kHz (i.e., the frequency range between the upper limit of the power quality band and the lower limit of the CISPR's conducted emissions band) is still to be consolidated and there is significant research work ongoing [26].

1.2.2.2 IEEE Std 519 Standard

The IEEE's standard IEEE Std 519 [25] is titled "IEEE Recommended Practice and Requirements for Harmonic Control in Electric Power Systems" and the latest version has been released in 2014. This standard guides the power system designers in the scenario where non-linear loads are connected to the network. In fact, as opposed to EN 50160, the IEEE Std 519's recommendations regard both the current and voltage harmonic distortion limits at the PCC between the system operators and the customers. As consequence, the good practices defined in the standard shall be followed both by the customers, preventing excessive current distortion from their loads, and by the system operators, limiting the voltage distortion of the supply, even by reducing the impedance characteristics of their system. The IEEE Std 519 covers all the voltage levels, but coherently with the choice made in the Paragraph 1.2.2.1, only the prescriptions regarding the LV and MV systems are reported. The harmonic voltage distortion limitations are listed in Table 1.6, where *U* is the voltage at the PCC, u_h is the harmonic voltage component RMS normalized by the fundamental power frequency component at the PCC, *THD* is the same as the one defined in Eq. (1.1) with h_{max} = 50 and $x_h = u_h$.

Table 1.6 Normalized harmonic voltage and THD limits for LV/MV networks according to IEEE Std 519.

Voltage *U* at the PCC [kV]	u_h [%]	*THD* [%]
$U \leq 1.0$	5.0	8.0
$1 < U \leq 69$	3.0	5.0

The limitations apply for the 95 % of the week, while exceptions are given on the 99 % of the day with values up to 1.5 times the Table 1.6's values. The harmonic current distortion limitations are instead listed in Table 1.7, where: i_h is the harmonic current component RMS normalized by the fundamental power frequency component at the PCC, h is the harmonic component order number, and *THD* is the one defined in Eq. (1.1), where $h_{max} = 50$ and $x_h = i_h$.

Table 1.7 Normalized current and THD limits for LV/MV networks according to IEEE Std 519.

	i_h [%] (odd harmonics)					
I_{SC}/I_L	$3 \leq h < 11$	$11 \leq h < 17$	$17 \leq h < 23$	$23 \leq h < 35$	$35 \leq h < 50$	*THD*
< 20	4.0	2.0	1.5	0.6	0.3	5.0
20 < 50	7.0	3.5	2.5	1.0	0.5	8.0
50 < 100	10.0	4.5	4.0	1.5	0.7	12.0
100 < 1000	12.0	5.5	5.0	2.0	1.0	15.0
> 1000	15.0	7.0	6.0	2.5	1.4	20.0

I_{SC} = maximum short-circuit current at the PCC.
I_L = maximum demand load current (fundamental frequency component) at the PCC.

Note: the even harmonics are limited to 25 % of the odd harmonic limits above.

The limitations apply for the 95 % of the week, while exceptions are given on the 99 % of the week and on the 99 % of the day with values up to 1.5 times and 2 times, respectively, the Table 1.7's values. Finally, the standard provides additional information on interharmonic voltage distortion, voltage notches and disturbance caused on nearby telecommunication lines.

1.2.3 Distribution Grid State Monitoring

With respect to the measurements for grid monitoring applications, additional elements on the topic are given in this Section, underlining the strong connection between the measurement and the power system sciences. The system operators must carry out a focal task, that is the state estimation (SE) of the network [27]. The successful SE allows them to maintain the network in a stable state, guaranteeing the energy supply to every connected load. Collecting via telemetry the various measurement from the installed instrumentation and the switches statuses, the energy management system (EMS) running the SE algorithm determines the optimal solution for the system state. There are major differences between the SE task in transmission and distribution networks. In general, the distribution networks are distinguished: first, by a radial topology, even though they are evolving towards a meshed topology to enhance the flexibility and the quality of the service, but also to allow for more distributed generation; second, by a substantial lower density of installed measuring instruments compared to the HV power systems. This causes a more intensive usage of the so-called pseudo measurements, which consist of historical data, short-term forecasts, generation dispatch and so on, resulting in a much more approximated SE solution. As the distribution networks are evolving towards the smart grid

model, new technologies are progressively installed, such as phasor measurement units [28], [29] and smart energy meters [30]–[32]. Given the economical budget limitations and the need of maximizing the results, research has been conducted not only to find the optimal placement for this new equipment, but also on the impact of the measurement uncertainty on the SE results [33]–[35]. Better SE results guarantee more network availability, because the impact of faults and other conditions affecting the normal safe operating status can be avoided or at least mitigated. Correct and reliable identification of the fault locations reduce the downtime due to maintenance time, improving the system operators' results. Another relevant consequence of the deployment of effective measurement instrumentation is the spotting of non-technical losses, defined as those energy losses due to energy thefts or malfunctioning meters. Finally, the metrological characterization of the measurement instrumentation employed in such critical applications is fundamental, as well as the one for the electrical assets diagnostics, and it will be discussed in Chapter 5.

Chapter 2 Sensors and Instrumentation for Power Network Monitoring

The present Chapter offers an overview of the state-of-the-art electrical sensors and instrumentation for the distribution power network monitoring, especially focusing on those studied during the 3-years PhD program activities. Some of them already play a central role in the nowadays distribution network, such as the inductive instrument transformers and the electronic energy meters; the others are gaining more attention and progressively new installations can be observed, this is the case of low-power instrument transformers, energy meters with smart features and, finally, the phasor measurement units.

2.1 Instrument Transformers

The instrument transformers (ITs) are the most common sensors for measuring currents and voltages in the distribution networks nodes. Their role is to adapt or transduce the measured quantity at the primary side of the device into an electrical quantity whose power can be managed by the input of the cascaded measuring instrumentation. The ITs can be basically categorized in different types, as sketched in Figure 1, and they will be further discussed in the following.

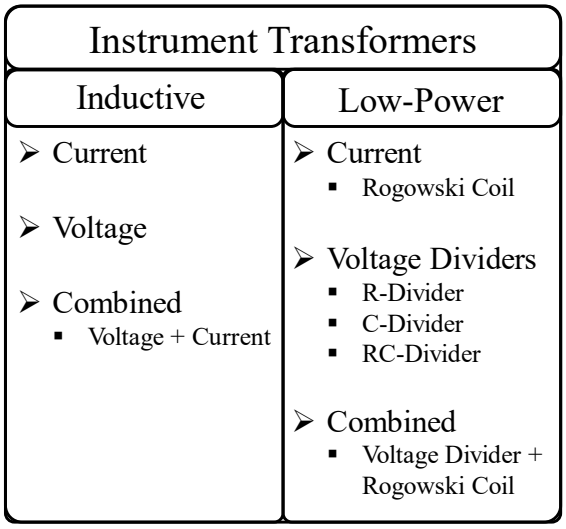

Figure 1 Classification of the instrument transformer types.

2.1.1 Inductive Instrument Transformers

The inductive instrument transformers (IITs) are traditional electric power transformers specifically designed for electrical measurement applications and they are the most common and traditionally employed devices across the MV and HV networks. The IITs are divided in two categories: the protective IITs and the measuring IITs. The protective IITs are the ones whose output signal is fed into the protective relays, and they

will not be discussed further. Hence, for sake of brevity, the measuring IITs will be simply referred as IITs, if not stated otherwise. The IITs characteristics are illustrated on their name plate, where the accuracy class and the rated output can be found. The rated output is defined in the standard EN 61869-1:2009 [36] as "*the value of the apparent power at a specified power factor which the instrument transformer is intended to supply to the secondary circuit at the rated secondary current (or voltage) and with rated burden connected to it*". As for the accuracy class, it is defined as "*a designation assigned to an instrument transformer the ratio error and phase displacement of which remain within specified limits under prescribed conditions of use*". These two definitions are fundamental from the metrological point of view since they outline the operating point of the IIT together with the error affecting the current (or voltage) scaling. As one can imagine, the error in sinusoidal conditions is about both the amplitude and the phase of the transduced quantity. This twofold aspect is evaluated by means of the ratio error and the phase displacement. More details will be given in the Paragraphs below.

2.1.1.1 Inductive Current Transformers

The inductive current transformers (ICTs), as the inductive voltage transformers (IVTs), are basically made by two windings (called "primary" and "secondary" windings) wound around a ferromagnetic core. However, with respect to ICTs, the primary winding often consists of a single turn embodied either by a bar in series with the conductor carrying the current to be measured, or by the conductor itself. In the latter case, the ICT is made of a toroidal ferromagnetic core on which only the secondary winding is wound, and the primary winding conductor passes straight through the toroid's hole. In Figure 2 a LV toroidal ICT (left) and an indoor MV ICT (right) are shown.

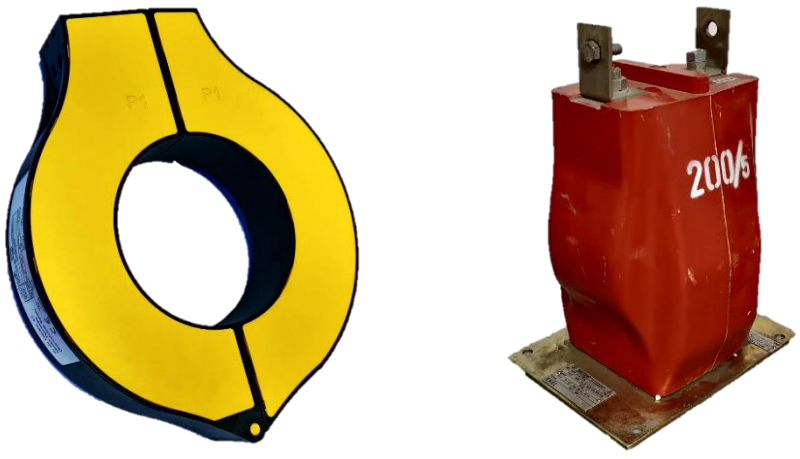

Figure 2 Inductive current transformer examples: a LV toroidal ICT (left) and an indoor MV ICT (right).

The primary winding is installed in series with the current to be measured, while the secondary is closed on a resistive load, called burden. In Figure 3 the typical ICT insertion schematic is represented, where *B* identifies the burden.

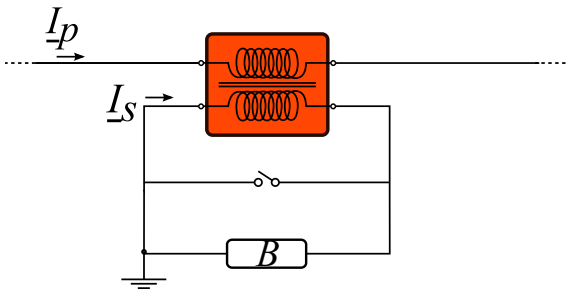

Figure 3 Inductive current transformer insertion schematic.

To minimize the influence of the ICT on the system connected at the primary side, the ICT's turn ratio is much less than 1 and the secondary is almost short-circuited by the burden. If the secondary is accidentally open circuited, the step-up-like transformation ratio determines an induced voltage at the secondary terminals which could be destructive for the winding insulation, consequently a protection control is needed. Moreover, the secondary winding is electrically grounded to drain away possibly dangerous capacitive currents and thus guaranteeing the electrical safety of the system [37], [38].

As mentioned before, the accuracy class definition depends on the ratio error and the phase displacement parameters. The ratio error ε_I is defined as [36], [39] "*the error which an instrument transformer introduces into the measurement and which arises from the fact that the actual transformation ratio is not equal to the rated transformation ratio*" and the following equation holds:

$$\varepsilon_I = \frac{k_{r_I}|\underline{I}_s| - |\underline{I}_p|}{|\underline{I}_p|} \times 100\ \%, \tag{2.1}$$

where, k_{r_I} is the ICT rated transformation ratio; $|\underline{I}_p|$ is the actual primary current RMS; $|\underline{I}_s|$ is the actual secondary current RMS when $|\underline{I}_p|$ is flowing. Whereas, the ICT phase displacement $\Delta\varphi_I$ is defined as [36], [39] "*difference in phase between the primary current and the secondary current phasors, the direction of the phasors being so chosen that the angle is zero for an ideal transformer. The phase displacement is said to be positive when the secondary current phasor leads the primary current phasor*", then:

$$\Delta\varphi_I = \angle\underline{I}_s - \angle\underline{I}_p, \tag{2.2}$$

where $\angle \underline{I}_p$ and $\angle \underline{I}_s$ are the phase angles of the secondary and primary current phasors $\underline{I}_s$ and $\underline{I}_p$, respectively.

Both the relationships expressed in Eqs. (2.1) and (2.2), which are strictly defined for sinusoidal waveforms only, can be further clarified with the help of the simplified transformer phasors vector diagram shown in Figure 4; where, $\underline{\Phi}_M$ is the phasor corresponding to the magnetizing flux, and $\underline{I}_0$ is the current phasor representing the sum of the magnetizing current and the current modeling the joule losses in the iron core.

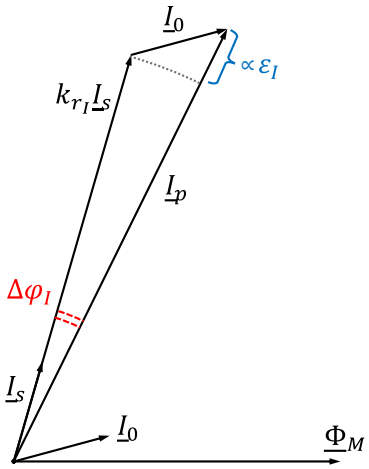

Figure 4 Inductive current transformer simplified phasors vector diagram.

The vector diagram emphasizes how the measurement error parameters strongly depend on $\underline{I}_0$. Thus, a well-designed ICT requires a high-permeability, finely laminated and high-resistivity ferromagnetic core. It is interesting to point out that there is no significant dependance on the windings ohmic resistance and on the leakage fluxes. Typical ICT rated output values go from few VA up to few tens of VA and the standard current outputs are 1 A and 5 A. As for the ratio error and phase displacement, the maximum limits for each accuracy class are prescribed in [39] and listed in Table 2.1.

Table 2.1 Ratio error and phase displacement limits for ICTs according to EN 61869-2.

Accuracy Class	Ratio error ± %						Phase displacement									
							± Minutes					± Centiradians				
	at current (% of rated)						at current (% of rated)					at current (% of rated)				
	1	5	20	50	100	120	1	5	20	100	120	1	5	20	100	120
0.1	-	0.4	0.2	-	0.1	0.1	-	15	8	5	5	-	0.45	0.24	0.15	0.15
0.2	-	0.75	0.35	-	0.2	0.2	-	30	15	10	10	-	0.9	0.45	0.3	0.3
0.2 S	0.75	0.35	0.2	-	0.2	0.2	30	15	10	10	10	0.9	0.45	0.3	0.3	0.3
0.5	-	1.5	0.75	-	0.5	0.5	-	90	45	30	30	-	2.7	1.35	0.9	0.9
0.5 S	1.5	0.75	0.5	-	0.5	0.5	90	45	30	30	30	2.7	1.35	0.9	0.9	0.9
1	-	3.0	1.5	-	1.0	1.0	-	180	90	60	60	-	5.4	2.7	1.8	1.8
3	-	-	-	3	-	3	-	-	-	-	-	-	-	-	-	-
5	-	-	-	5	-	5	-	-	-	-	-	-	-	-	-	-

2.1.1.2 Inductive Voltage Transformers

The inductive voltage transformers (IVTs) are step-down electric power transformers and their construction is strongly dependent on the insulation design, which is required to withstand the voltage difference between the high-voltage terminal and the lower voltage parts. For HV applications, where the voltage difference imposes a burdensome design, a capacitive divider stage is commonly added before the IVT primary winding terminals. This specific design is called capacitor voltage transformer. In Figure 5, an indoor (left) and an outdoor (right) MV IVTs are shown.

Figure 5 MV Inductive voltage transformer examples, indoor (left) and outdoor (right) designs.

The primary winding is installed in parallel with the voltage to be measured, while the secondary is closed on the burden. In Figure 6 the typical IVT insertion schematic is represented, where *B* identifies the burden.

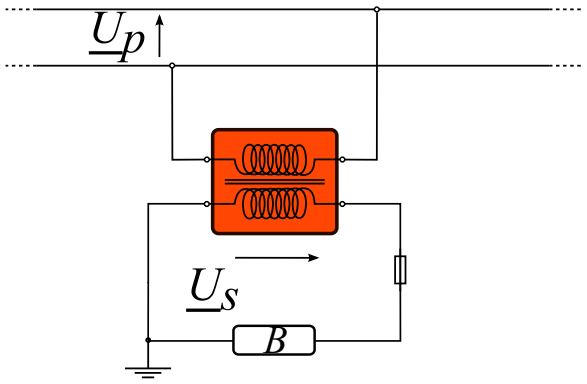

Figure 6 Inductive voltage transformer insertions schematic.

As for the ICTs, also the IVTs must minimize their influence on the system connected at the primary side. Consequently, the IVT's turn ratio is much greater than 1 and the secondary is closed on a high-impedance

burden. To avoid large current absorption, a current limiting system is installed at the secondary side of the IVT. The secondary winding is electrically grounded for safety as well.

The ratio error ε_U and the phase displacement $\Delta\varphi_U$ definitions for IVTs are identical to the ones for ICTs, but this time for voltages, as in Eq. (2.3) and Eq. (2.4):

$$\varepsilon_U = \frac{k_{r_U}\left|\underline{U}_s\right| - \left|\underline{U}_p\right|}{\left|\underline{U}_p\right|} \times 100\ \%, \tag{2.3}$$

$$\Delta\varphi_U = \angle\underline{U}_s - \angle\underline{U}_p, \tag{2.4}$$

where, k_{r_U} is the IVT rated transformation ratio, $\left|\underline{U}_p\right|$ is the actual primary voltage RMS, $\left|\underline{U}_s\right|$ is the actual secondary voltage RMS when $\left|\underline{U}_p\right|$ is applied, $\angle\underline{U}_p$ and $\angle\underline{U}_s$ are the phase angles of the secondary and primary voltage phasors $\underline{U}_s$ and $\underline{U}_p$, respectively. In Figure 7 a simplified transformer phasors vector diagram graphically represents the errors of Eqs. (2.3) and (2.4). The complex quantity $\underline{Z}_{tot}$ denotes the total effective winding impedance of the IVT.

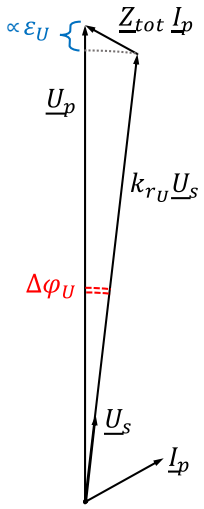

Figure 7 Inductive voltage transformer simplified phasors vector diagram.

Figure 7 shows that the IVT measurement error parameters ε_U and $\Delta\varphi_U$ depend on both $\underline{Z}_{tot}$ and $\underline{I}_p$; the latter, in turn, is equal to the vector sum of $\underline{I}_0$ and $\underline{I}_s$ referred to the primary side. Hence, it is evident a much more complex relationship between the constructive aspects and the error parameters. In general, for a good IVT design, the windings shall present a low resistivity and an effective coupling with a high-performance ferromagnetic core. The typical IVT rated output values goes from few VA up to a hundred VA and the common standard voltage outputs are 100 V or 100/√3 V, depending on the insertion. The ratio error and phase displacement limits for each accuracy class are prescribed in [40] and listed in Table 2.2.

Table 2.2 Ratio error and phase displacement limits for IVTs according to EN 61869-3.

Class	Voltage (ratio) error ± %	Phase displacement	
		±Minutes	±Centiradians
0.1	0.1	5	0.15
0.2	0.2	10	0.3
0.5	0.5	20	0.6
1.0	1.0	40	1.2
3.0	3.0	-	-

2.1.2 Low-Power Instrument Transformers

During the last decades a new generation of ITs has been developed and they are referred to as low-power instrument transformers (LPITs). The architecture of the LPITs is substantially different from the traditional IITs since it is based on very different technologies. In fact, the LPITs could be composed of different stages, both active and passive, also including the integration of digital systems. These differences between LPITs and IITs allow for the highlighting of the advantages and disadvantages of this new generation ITs compared to the traditional ones. Not surprisingly, the accuracy specifications of LPITs are still expressed by means of the ratio error and the phase displacement, computed by means of the input and the output quantity. In presence of digital stages, the evaluation of the LPITs' phase displacement could be more cumbersome compared to the IIT case. Below a brief description of some of the most common implementations for current and voltage measurements in distribution networks is given.

2.1.2.1 Rogowski Coil

The Rogowski coil is a transducer that converts alternating currents in alternating voltages. It is made of a non-ferromagnetic toroidal core around which an insulated wire is wound to form a coil. The toroidal core acts just as mechanical support for the coil and a soft plastic sheath embeds the whole thing. Some examples of Rogowski coils are displayed in Figure 8. From left to right: a flexible, split-core LV solution, a MV combined LPIT featuring a Rogowski coil within the resin body, a rigid window-like design.

Figure 8 Different Rogowski coil examples. From left to right: flexible, split-core LV solution, a MV combined LPIT featuring a Rogowski coil within the resin body, a rigid not-openable design.

The working principle is based on the Faraday's law of induction: the conductor carrying the current to be measured passes through the hole delimited by the toroidal support and the current's time-varying magnetic flux links to the coil, producing a voltage between the coil terminals. Often the coil is electrically shielded, and a third terminal connected to the shield is available. The toroidal core is usually built in a split-core solution, but also not-openable cores can be found. Given the weak magnetic coupling due to the low magnetic permeability of the core, the Rogowski coil is intrinsically not very sensitive (a few kiloampere current at power frequency, would result typically in tens or few hundreds of millivolts). Moreover, the output voltage is proportional to the derivative of the current, this requires an integrating stage, which can be implemented in an analog or a digital solution, depending on the design constraints. As conclusion, the Rogowski coil is cheap, very light, flexible, and easy to install, ensuring galvanic separation. Most of all, thanks to the excellent linearity due to the absence of iron, it is capable of measuring currents characterized by wide dynamics and frequency bandwidth. This feature is very important in the Smart Grid power quality scenarios, especially if compared to the ICTs, which are subjected to iron core saturation and bandwidths limited to few kHz. Despite its advantageous characteristics, the Rogowski coil has some drawbacks compared to the ICTs: it needs signal conditioning which requires a power supply, it suffers external electromagnetic disturbances and the relative position between the core and the conductor affects the measurement result.

2.1.2.2 Voltage Dividers

The voltage dividers, as the IVTs, scale down the primary voltage to a secondary voltage that can be managed by the instrumentation connected to the transducer. As it can be deduced by their name, they are simple resistive, capacitive, resistive-capacitive voltage dividers. In MV applications the capacitive dividers are frequently used since they work up to MHz and almost no heat losses are present. Their accuracy is limited by the non-ideal behavior of the dielectric material, and they must be properly shielded. In contrary of the

resistive dividers, the purely capacitive dividers cannot be employed in direct current applications. They are lightweight and much less bulky than IVTs, but often active signal conditioning circuit is needed. Some pictures of MV capacitive dividers are reported in Figure 9. From left to right: an indoor MV capacitive divider, an outdoor MV capacitive divider, an outdoor MV combined LPIT featuring a capacitive divider.

Figure 9 MV voltage divider examples. From left to right: an indoor MV capacitive divider, an outdoor MV capacitive divider, an outdoor MV combined LPIT featuring a capacitive divider.

2.2 Energy Meters

The electrical energy meters (EMs) are the devices accountable for the recording of the electric loads' energy consumption, with a well-defined accuracy. Needless to say, this operation is crucial for correct energy billing and power network load knowledge. Historically, the EMs were electromechanical devices: a torque, proportional to the electric power absorbed at the load terminals, drives a rotating disk, which in turn increments the count of a mechanical register. Such a device has many drawbacks, and it is not suitable for the Smart Grid development: it requires the human intervention for reading the register and it can only measure the absorbed active energy. The progressive integration of electronic and digital components in the EMs' design have opened up for the implementation of a large number of sophisticated functionalities. In fact, as a first step, the digital sampling and computing have allowed for voltage, current, reactive and active power measurements. The game-changing technology to make the EMs "smart" is the secure two-way communication interface [1], [41]. This enables the system operators to remotely retrieve the measured quantities from the EMs distributed network, perform bi-directional billing with prosumers, and take actions such as modifying customers' service-level parameters and also disconnecting them. Moreover, the two-way communication feature coordinated with proper measurement procedures and control algorithms would enable system fault and non-technical losses detection and diagnosis, demand-side management, power quality control, and other advanced operations. In Figure 10 the typical schematic of a modern single-phase EM is presented. Two voltage signals proportional to the load current i and to the load voltage v, respectively, are

appropriately filtered (BF) and amplified (A) before being sampled by an analog-to-digital converter (ADC). The digitized samples are then stored in memory (M) and a digital signal processor (DSP) performs the computation for the required measurements. Finally, the microprocessor (μP) manages the display (D) and the communication with the system operator's data concentrator. For LV EMs, the voltage transducer is typically a voltage divider, and the current sensor is a resistive shunt. When high currents and voltages must be measured, the EM's interface with the active line are ITs and their output is acquired. After that, the voltage and current sampling from the ADCs must be simultaneous, otherwise the instantaneous power would be wrongly measured. Moreover, if active/reactive power measurement are required, then a phase-locked loop (PLL) is needed to synchronize the sampling to the mains frequency. Usually, there are LED indicators on the device interface blinking every time the measured energy increases by one unit (e.g., one blink for 1 Wh of active energy absorbed).

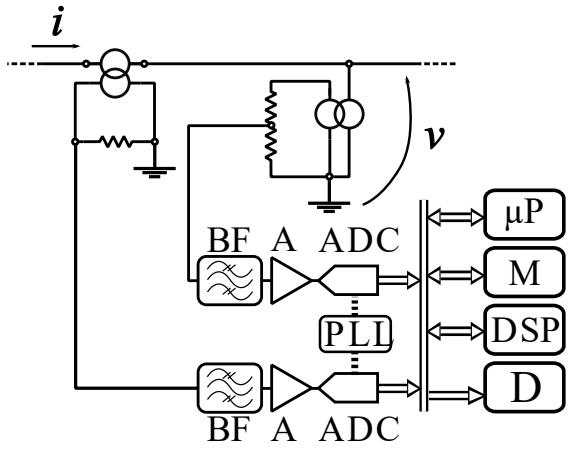

Figure 10 Modern energy meter generic schematic.

The EM calibration is quite delicate, because the electric energy depends on the following different quantities: voltage, current and time. A common procedure is the employment of a standard reference energy meter that reads the LED light pulses emitted by the tested EM. The EM accuracy is expressed as a relative error and typical electronic EM accuracy classes go from 0.5 % up to 2.5 %. More will be discussed in Section 5.1, where the relevant standards are presented too.

2.3 Phasor Measurement Units

The pursuance of the Smart Grid demands the development of applications capable of enhancing the power network monitoring. These applications can be accomplished by deploying many intelligent devices that communicate among each other, gathering pieces of information to depict the status of the monitored power network portion. To obtain this unified picture, the devices must be coordinated by sharing a common

time reference, i.e., they must be synchronized. Such a solution empowers the recording of the events and electric quantities in wide areas, hence advanced fault analysis and study of the network operating status evolution can be carried out. This topic is central in the development of smart substations, intelligent relay equipment, LPITs coupled with stand-alone merging units, and the IEC 61850 standard [42] actual implementation in general. However, these new technologies require a thorough characterization from the timing point of view, assessing how good is the synchronization with the unified time reference. In the next years, this will be a major challenge to be faced by the metrology applied to the power systems. One of the most important instruments in the scenario presented above is the phasor measurement unit (PMU). The PMU is a measurement device or function in a multifunction device that outputs a synchronized phasor, frequency, rate of change of frequency (ROCOF) from voltage and/or current signals and a time synchronizing signal [43], [44]. The time synchronizing signal is usually an accurate Coordinated Universal Time (UTC) timestamp, which is necessary to tag the measured output quantities. In PMU applications, the generic alternating voltage or current signal x is modeled as:

$$x(t) = X_M(t)\cos[2\pi f_0 t + \phi(t)] + D(t)\,, \tag{2.5}$$

where, t is the time and $t = 0$ matches the UTC second occurrence, X_M is the cosine amplitude; f_0 is the rated power frequency, ϕ is the phase angle and D is the sum of all disturbances, such as noise, harmonics, etc. The definition of PMU introduces three measurands: the synchronized phasor, the frequency and the ROCOF; all of them are explained in the following. The synchronized phasor (or synchrophasor) $\underline{X}$ is an extension of the traditional phasor concept to a time-referenced and dynamic context and its expression is:

$$\underline{X}(t) = \frac{X_M(t)}{\sqrt{2}} e^{-j\phi(t)}\,. \tag{2.6}$$

The synchrophasor links the phasor's phase angle ϕ to the UTC, stating as null phase the phase of a sinusoidal waveform which shows its maximum value in correspondence of the UTC second rollover. Second, the RMS $\frac{X_M}{\sqrt{2}}$ and ϕ of the synchrophasor are defined as time-dependent quantities: this because the real-world power system signals are not perfect steady-state sinusoids and the synchrophasor's time dependance takes that into account. A graphical representation is given in Figure 11. In the upper part of the plot, a sinusoidal signal (normalized by its amplitude) has its peak value at $t = 0$, corresponding to the UTC second occurrence, and at $t = t^*$ there is a 15 % step-increase of the magnitude and a 45° phase variation. In terms of synchrophasors, the sinusoidal signal is represented by $\frac{1}{\sqrt{2}}\angle 0$ (bottom-left polar plot) for $0 < t < t^*$ and by $\frac{1.15}{\sqrt{2}}\angle 45$ (bottom-right polar plot) for $t \geq t^*$.

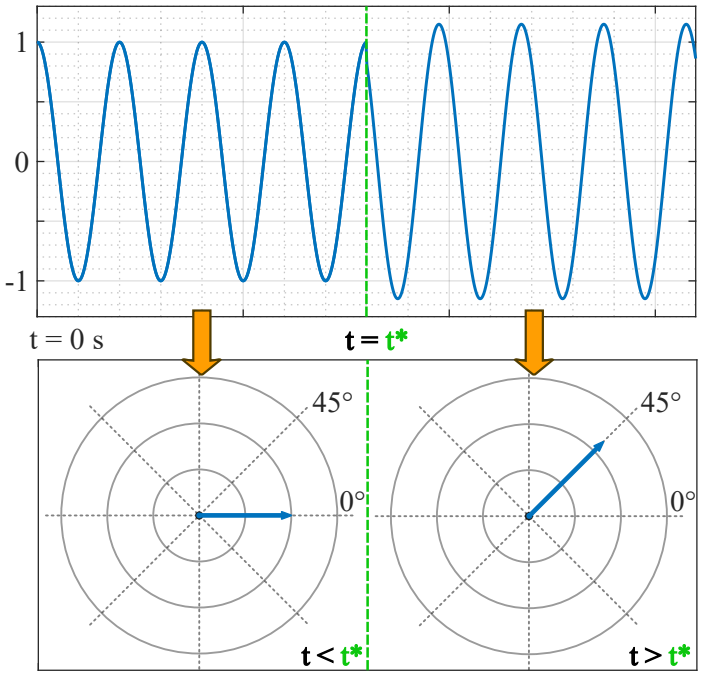

Figure 11 Time-varying synchrophasor representation.

The frequency is defined as:

$$f(t) = f_0 + \Delta f = f_0 + \frac{1}{2\pi}\frac{d\phi(t)}{dt}, \tag{2.7}$$

where Δf is the frequency variation with respect to f_0. Of course, the frequency variation influences directly $\phi(t)$. Finally, the ROCOF is just the frequency time-variation so:

$$ROCOF(t) = \frac{df(t)}{dt} = \frac{1}{2\pi}\frac{d^2\phi(t)}{dt^2}. \tag{2.8}$$

The PMU shall forward to the data concentrator the synchrophasor, the frequency and the ROCOF measurements tagged with the UTC timestamp corresponding to the time instant they refer to. These data packets are sent at rates that are multiples or sub-multiples of the rated power frequency: this rate is called reporting rate and it is usually denoted with F_s. The metrological performance of PMUs is characterized by means of quite simple indexes defined in the IEEE Std 60255-118-1 [43]. Each index is related to one of the measured quantities listed above, that is, the synchrophasor, the frequency and the ROCOF. The first one is the total vector error (TVE), which is defined as:

$$TVE = \frac{|\hat{\underline{X}} - \underline{X}|}{|\underline{X}|} = \sqrt{\frac{(\hat{X}_r - X_r)^2 + (\hat{X}_i - X_i)^2}{(X_r)^2 + (X_i)^2}}, \tag{2.9}$$

where, $\underline{\hat{X}}$ is the measured synchrophasor, $\underline{X}$ is the reference synchrophasor and the subscripts r and i indicate the real and imaginary part respectively of the synchrophasor. The TVE quantifies the deviation of the measured synchrophasor from the reference one and it is usually expressed in percent. Assuming a 50-Hz system and no errors affecting the magnitude of $\underline{\hat{X}}$, a phase angle error of approximately 0.57° between $\underline{\hat{X}}$ and $\underline{X}$ would cause an unacceptable value of the TVE. Since the phase angle error of 0.57° translates into a time error of approximately 32 μs, it is shown how tight the timing requirements are for the synchrophasor measurements. The frequency and the ROCOF measurements are characterized with a simple absolute error, the frequency error (FE) and the ROCOF error (RFE), which are respectively expressed in Eqs. (2.10) and (2.11):

$$FE = \hat{f} - f \ , \tag{2.10}$$

$$RFE = \hat{ROCOF} - ROCOF \ ; \tag{2.11}$$

the hat accent symbol marks the measured value as in Eq. (2.9). It follows from Eqs. (2.6), (2.7) and (2.8) that also the TVE, the FE and the RFE are defined as time-dependent quantities. The maximum tolerated values for the aforementioned indexes depend on the PMU class, as defined by the IEC 60255-118-1 standard. The document describes the M class and the P class: the M-class PMU is the one dedicated to measurement and monitoring applications, where accuracy is privileged; whereas, the P-class PMU are fast-response PMUs for protection applications. In Table 2.3 the TVE limits prescribed by the standard for steady-state synchrophasor measurements are listed, for both P-class and M-class PMU. In Table 2.4, instead, the limitations on the FE and the RFE are reported.

Table 2.3 TVE limits for steady-state measurements according to IEC 60255-118-1.

Influence quantity	Reference condition	Minimum range of influence quantity over which PMU shall be within given TVE limit			
		P-class		M-class	
		Range	Max TVE [%]	Range	Max TVE [%]
Signal Frequency	f_0	f_0± 2.0 Hz	1	f_0± 2.0 Hz for F_s< 10 f_0± F_s/5 for 10 ≤ F_s <25 f_0± 5.0 Hz for F_s ≥ 25	1
Signal Magnitude Voltage	100 % rated	80 % to 120 % rated	1	10 % to 120 % rated	1
Signal Magnitude current	100 % rated	10 % to 200 % rated	1	10 % to 200 % rated	1
Harmonic distortion (single harmonic)	<0.2 % THD	1 %, each harmonic up to 50th	1	10 %, each harmonic up to 50^{th}	1
Out of band interference signal	<0.2 % of the input signal magnitude		None	10 % of input signal magnitude for F_s ≥ 10. No requirement for F_s < 10.	1.3
Out-of-band interference testing: The input test signal frequency f_{in} is varied between f_0 and ± 10 % of F_s/2 with the maximum variation limited to ± 5 Hz.					

Table 2.4 FE and RFE limits for steady-state measurements according to IEC 60255-118-1.

Influence quantity	Reference condition	Minimum range of influence quantity over which PMU shall be within given FE and RFE limits			
		P-class		M-class	
Signal Frequency	f_0	Range: $f_0 \pm$ 2.0 Hz		Range: $f_0 \pm$ 2.0 Hz for $F_s < 10$ $f_0 \pm F_s/5$ for $10 \leq F_s < 25$ $f_0 \pm$ 5.0 Hz for $F_s \geq 25$	
		Max |FE| [Hz]	Max |RFE| [Hz/s]	Max |FE| [Hz]	Max |RFE| [Hz/s]
		0.005	0.4	0.005	0.1
Harmonic distortion (single harmonic)	<0.2 % THD	1 %, each harmonic up to 50th		10 %, each harmonic up to 50th	
		Max |FE| [Hz]	Max |RFE| [Hz/s]	Max |FE| [Hz]	Max |RFE| [Hz/s]
	F_s >20	0.005	0.4	0.025	No requirements
	$F_s \leq$20	0.005	0.4	0.005	No requirements
Out of band interference signal	<0.2 % of the input signal magnitude	-		Interfering signal 10 % of signal magnitude	
		-	-	Max |FE| [Hz]	Max |RFE| [Hz/s]
		-	-	0.01	No requirements

The reference synchrophasor is usually a simulated signal, if a PMU algorithm is tested; whereas, if an actual PMU device is tested, the reference synchrophasor is the one produced by a calibrator. The latter is the case of the calibration conducted in the research activity discussed in Section 5.3. Finally, a generic architecture of a PMU hardware implementation is shown in Figure 12. The main aspect to underline is the usage of the absolute timing reference (coming from either a GPS receiver, or an IRIG-B or IEEE 1588 peripherals) to drive the ADC and acquiring samples synchronous to the timing reference. Concerning the element called "Estimator", the scientific literature is rich of synchrophasor estimation algorithms, based on different techniques, such as the discrete Fourier transform, Kalman filters, etc. More considerations will be made within the context of Section 5.3.

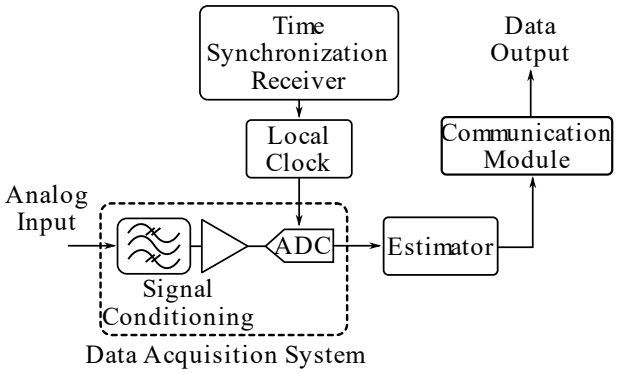

Figure 12 Phasor measurement unit hardware schematic diagram.

Chapter 3 Uncertainty Evaluation Fundamentals

This Chapter's goal is offering a theoretical background for the metrological characterization of measuring instruments and sensors. Some of the main concepts of the metrology science are summarily discussed, highlighting the uncertainty and its analysis. Special attention is reserved for the "Guide to the expression of uncertainty in measurement" (GUM), which constitutes an acknowledged reference guideline for engineers and scientists who daily deal with measurements and experimental activities.

3.1 Measurement Process and Uncertainty

The International Vocabulary of Metrology (VIM) [45] defines the measurement as "*process of experimentally obtaining one or more quantity values that can reasonably be attributed to a quantity*". The quantity to be measured, called measurand, is in turn defined as "*property of a phenomenon, body, or substance, where the property has a magnitude that can be expressed as a number and a reference*", where the reference is typically a measurement unit in physical applications [46]. Hence, the measurement process creates a bridge between the empirical word, made of phenomena and physical events, and the symbolic world, made of models aiming to describe the phenomena with numbers. However, this connection is not ideal nor trivial and many factors can affect it. In fact, after the identification of the measurand, both the experimental process and the modelling process introduce non-idealities. During the experimental process, the measurand, the measuring instrument and the surrounding environment interact among each other (e.g., the laboratory temperature changes the measuring instrument characteristics, the measuring instrument interacts with the measurand and alters it, etc.). The modelling process employs mathematical relationships to describe the whole measurement context: the model's mathematical approximations, the incomplete knowledge of the measurand and of the experimental setup inevitably impact the quality of the information obtainable from the measurement process. These considerations and the definitions from the VIM suggest that the measurement result is not complete if only a number together with a measurement unit is reported: indeed, additional information quantifying the quality of the measurement result must be expressed too. This information comes from the modern concept of uncertainty, which is addressed in the GUM as for its evaluation. The GUM states that "uncertainty" means doubt and it reflects the lack of knowledge of the value of the measurand [47]. The operational definition of the measurement uncertainty given by the VIM is *"parameter, associated with the result of a measurement, that characterizes the dispersion of the values that could reasonably be attributed to the measurand"*. What is the "dispersion of the values" involved in the definition and where does it come from?

In this Section it has been already mentioned that the uncertainty raises from the incomplete knowledge and the modelling approximations of the set composed of the measurand, the measurement instrument and the measurement environment. The effects generating uncertainty could influence the measurement result in two different ways and, hence, are identified as systematic effects and random effects [46], [47]. The systematic effects are generally caused by the influence quantities and, if the measurement procedure is repeated in the same conditions, and the influence quantities do not change, it is not possible to detect them. Nevertheless, by varying the influence quantities and/or changing the measurement procedure, they can be spot and corrected. The GUM stresses the fact that, in order to properly evaluate the uncertainty, the systematic effects correction must be done first. The correction of the systematic effects means that modelling and experimental activity is carried out to evaluate and quantify the compensation. However, this compensation can only reduce the systematic effects because the procedure for the correction is affected by uncertainty as well. The random effects, instead, are attributable to unpredictable or stochastic temporal and spatial variation of influence quantities. They cannot be compensated but, on the other hand, their effect can be mitigated by increasing the number of repeated observations and their statistical expected value is zero.

3.2 Guide to the Expression of Uncertainty in Measurement (GUM)

After the definition of the uncertainty and its meaning in Section 3.1, this Section is about how to express the uncertainty of a measurement result. The "Guide to the expression of uncertainty in measurement" (GUM) is a document developed by the major international metrological authorities with the goal of defining a consensual approach for the measurement uncertainty evaluation [47]. Such a shared methodology is fundamental for international trade and measurement comparisons. Nowadays, the GUM's approach is widely considered as the state-of-the-art one. The statistics is the tool chosen by the GUM for managing the uncertainty evaluation. In particular, the uncertainty components are quantified as the variance or the standard deviation of probability distribution functions (PDFs), which can be obtained either from observed frequency distributions or from *a-priori* assumed PDFs. The former method is referred as Type A, while the second as Type B. If the uncertainty of a measurement result is expressed as a standard deviation, it is then called standard uncertainty and the notation is $u(x_i)$, where x_i is the estimate for the generic quantity X_i. The subscript i is introduced for the generalization to N quantities shown in the next Sub-Section.

3.2.1 Evaluating Standard Uncertainty

First, the Type A method for the uncertainty evaluation is considered. If it is possible to observe a measurand X_i, behaving as a random variable, for n times and these n observations $X_{i,k}$ are independent and

taken in the same conditions, then x_i, the best estimate of the expected value of X_i, is the arithmetic mean (or average) $\overline{X_i}$:

$$\overline{X_i} = \frac{1}{n}\sum_{k=1}^{n} X_{i,k}. \tag{3.1}$$

The $X_{i,k}$ observations are scattered about their average $\overline{X_i}$ due to the random variation of influence quantities: the experimental standard deviation $s(X_{i,k})$ characterizes this variability, and it is given by

$$s(X_{i,k}) = \sqrt{\frac{1}{n-1}\sum_{j=1}^{n}(X_{i,j} - \overline{X_i})}, \tag{3.2}$$

where $j, k = 1, \dots, n$. The central limit theorem (CLT), which is enounced in Paragraph 3.2.1.1, enables to determine the experimental standard deviation of the mean as:

$$u(x_i) = s(\overline{X_i}) = \frac{s(X_{i,k})}{\sqrt{n}}. \tag{3.3}$$

The Eq. (3.3) is used to evaluate the standard uncertainty $u(x_i)$ and, consequently, it quantifies how well $\overline{X_i}$ estimates the measurand. Finally, to successfully apply the Type A method a sufficiently high number of observations is needed, often $n \geq 30$ is considered as acceptable.

The Type B method is very different from Type A since the information regarding the relevant knowledge on the measurand is obtained from *a-priori* considerations. Examples of these considerations are [47]: past measurement data, calibration certificates, instrumentation specifications, knowledge developed with experience on the behavior of materials and instruments. It is evident the strong link with practice and personnel qualification. To eventually estimate the standard uncertainty, the available information should allow for reasonable assumption both on the shape of the PDF representing the measurand X_i and on the probability that the measurand lies in a defined interval [46], [47]. For instance, the manufacturer's accuracy specifications of a measurement instrument often declare a range in which the measurand is contained at high probability. If no information on the shape of the PDF is given, then it is proper to suppose it as a uniform distribution, because the measurand could lie anywhere in the range. Under this assumption, the expected value x_i of the measurand X_i is the center of the range and the standard uncertainty is:

$$u(x_i) = \frac{a}{\sqrt{3}}, \tag{3.4}$$

where a is the half-amplitude value of the range stated by the manufacturer's accuracy specifications. This value usually depends on parameters, such as the gain error, non-linearity error and offset error, obtained from the calibration of the measurement instrument.

If the uncertainty affecting a quantity is evaluated both with Type A and Type B methods, or/and the measurand is a quantity indirectly obtained from other measurands (i.e., measuring the resistance of a resistor with a voltmeter and an ammeter), then techniques for combining the uncertainties are needed.

If Y is a measurand obtained indirectly by the measurement of N other measurands X_i, there will be a relationship f, such as

$$Y = f(X_1, \dots, X_i, \dots, X_N)\,. \tag{3.5}$$

Coherently with the notation adopted above, the estimate of Y is $y = f(x_1, \dots, x_i, \dots, x_N)$ and it may be obtained from:

$$y = \overline{Y} = \frac{1}{n}\sum_{k=1}^{n} Y_k = \frac{1}{n}\sum_{k=1}^{n} f\left(X_{1,k}, \dots, X_{i,k}, \dots, X_{N,k}\right), \tag{3.6}$$

where Y_k are the n independent determination of Y, based on the n complete sets of the N directly measured quantities. The estimated standard deviation associated with y is called combined standard uncertainty and it is denoted as $u_c(y)$, which can be computed from the standard uncertainties $u(x_i)$ associated with the directly measured N input estimates, whether they have been obtained by means of Type A or Type B methods. In general, the N random variables X_i representing the measurands could present a certain degree of correlation and the $u_c(y)$ is then computed as:

$$u_c(y) = \sum_{i=1}^{N}\left(\frac{\partial f}{\partial x_i}\right)^2 u^2(x_i) + 2\sum_{i=1}^{N-1}\sum_{j=i+1}^{N}\frac{\partial f}{\partial x_i}\frac{\partial f}{\partial x_j}u(x_i)\,u\left(x_j\right)r\left(x_i, x_j\right), \tag{3.7}$$

where $-1 \le r\left(x_i, x_j\right) \le 1$ is the estimated correlation coefficient and it expresses the degree of correlation between x_i and x_j. The Eq. (3.7), also known as uncertainty propagation law, is derived from a first order Taylor series expansion, hence it holds if f is fairly linear for small deviations around the estimates of the input quantities. Finally, the Eq. (3.7) does not provide any information regarding the PDF of y.

In applications requiring reliable measurement results, often the estimate of the expanded uncertainty U is needed. The expanded uncertainty is *"a quantity defining an interval about the result of a measurement that may be expected to encompass a large fraction of the distribution of values that could reasonably be attributed to the measurand"* [47]. The expanded uncertainty U is given by:

$$U = ku_c(y), \tag{3.8}$$

where k denotes the coverage factor. The "*fraction*" mentioned in the definition is the probability that the interval $[y - U, y + U]$ contains Y. It can be viewed as the level of confidence of the interval defined by y and U if assumptions on the distribution can be made. In the Paragraphs below, two powerful tools useful also to determine the distribution shape of y are presented.

3.2.1.1 Central Limit Theorem

The central limit theorem (CLT) [47] states that the distribution of $Y = \sum_{i=1}^{N} c_i X_i$ will be approximately normal with expected value $E(Y) = \sum_{i=1}^{N} c_i E(X_i)$ and variance $\sigma^2(Y) = \sum_{i=1}^{N} c_i^2 \sigma^2(X_i)$, if the X_i are independent and none of the X_i is dominant over the others. Of course, $E(X_i)$ and $\sigma^2(X_i)$ are the expected value and the variance of X_i. The bigger the N the more the normal distribution is approached. However, it can be shown that the convolution of three equal uniform distributions already yields an approximately normal distribution. Obviously, the sum of any number of normal distributions yields a normal distribution.

3.2.1.2 Monte Carlo Numeric Simulation

If either the analytical solution of Eq. (3.7) is too complex, or the relationship f is complicated, or the CLT cannot be applied, then the Monte Carlo (MC) numerical simulation comes to help in the uncertainty expression process. The Supplement 1 to the GUM [48] discusses this method and it presents the steps to perform the uncertainty evaluation accordingly. The idea behind this method is to propagate the PDFs of the directly measured input quantities X_i through the relationship f defined in Eq. (3.5). The result approximates the PDF of Y, from which the estimates of the expected value y, the combined standard uncertainty $u_c(y)$ and the expanded uncertainty U can be obtained. The MC computational step-procedure is summarized below:

1. select the number M of MC trials to be made. The general rule is selecting $M > \frac{10^4}{1-p}$, where p is the desired coverage probability of the final measurement result.
2. Generate M vectors $\boldsymbol{x}_r$, where $r = 1,2, \dots M$, by sampling from the PDFs assigned to the set of the N input quantities X_i. The vector $\boldsymbol{x}_r = x_{1,r}, x_{2,r}, \dots, x_{M,r}$ contains the r-th realization of each X_i.
3. For each vector $\boldsymbol{x}_r$, the relationship f is evaluated to obtain the corresponding value $y_r = f(\boldsymbol{x}_r)$. This operation yields M model values of the output quantity Y.

4. The M model values y_r are sorted into strictly increasing order. The result is a discrete approximation of the PDF describing Y.
5. Such PDF allows the computation of the estimate y of Y and the standard uncertainty $u(y)$ associated with y as follows:

$$y = \frac{1}{M}\sum_{r=1}^{M} y_r \,, \tag{3.9}$$

$$u^2(y) = \frac{1}{M-1}\sum_{r=1}^{M} (y_r - y)^2. \tag{3.10}$$

6. Finally, the PDF is used to determine an appropriate coverage interval for Y, coherently with the chosen coverage probability p.

The MC method is valid and can be applied only if the following conditions hold:

i. f is continuous with respect to the input quantities X_i around their best estimates x_i;
ii. the distribution function for Y is continuous and strictly increasing;
iii. the PDF for Y is:
    a. continuous over the interval for which this PDF is strictly positive;
    b. unimodal (single-peaked);
    c. strictly increasing (or zero) to the left of the mode and strictly decreasing (or zero) to the right of the mode;
iv. the expected value and the variance of Y exists;
v. a sufficiently large value of M is used.

Chapter 4 Measurements for Electrical Assets Diagnostics

As introduced in Chapter 1, one of the two main roles of the measurements for the Smart Grid is supporting the electrical asset diagnostics. This objective can be pursued by: first, developing measurement instrumentation to acquire physical quantities called "diagnostic markers"; second, characterizing the implemented measurement chain from the metrological point of view. The present Chapter reports the research conducted following these two ideas, whose results have been published in [49]. In particular, the focus has been set on the development of an innovative measurement system for carrying out MV surge arresters diagnostics by monitoring the surge arrester leakage current. The main innovative concept behind this measurement system is the fact that it is a UAV-based system, which allows for the implementation of a widespread distributed system for outdoor MV assets monitoring situated in areas with low-density population, such as the rural ones.

4.1 UAV-based Instrument for MV Surge Arresters Diagnostics

An important and common device implemented in both transmission and distribution networks is the surge arrester (SA). It is used to protect electrical assets from overvoltage transients. The causes of such phenomena are multifold: lightning, switching events, faults, etc. As for their manufacturing, in the last decades SAs have undergone structural changes, which modified their properties. For example, the resistive part changed from a SiC to a metal oxide technology. Moreover, the SAs external housing once was made of porcelain while now it is simple silicone material. Although the improvements reduced the costs and extended the life of the SAs; some drawbacks still affect their life cycle. As an example, when a SA suffers a fault the silicone housing material does not allow a visual detection of the fault itself (as it was possible with the porcelain one). Hence, utilities operators cannot find and replace the faulted SAs by in-field visual inspection. Furthermore, the constant application of the rated AC voltage on the element causes the well-known leakage current which contribute to the SA aging. The scientific literature provides several interesting works on the current detection and monitoring of SAs. In [50] the leakage current flowing through the SA is measured by using fiber-optic technology. In [51], [52] instead, a new method to isolate the dangerous leakage current component is provided. In addition, [53], [54] present studies where thermo-cameras images of SAs are combined with the leakage current third harmonic to estimate the "health" status of the arresters. In this research, a pole-mounted microcontroller-based system for the leakage current detection in SAs has been presented. The measurement system is designed to be mounted on MV poles along with the device to be monitored: the SA. The measurement system is based on a microcontroller unit equipped with a current sensor and the signal analysis is performed in the frequency domain. Finally, the measurement system transmits the

measurement data to an UAV dedicated to the remote data collection. The goal of this research is to validate the technological feasibility of developing a distributed measurement system that monitors pole-mounted electrical assets and in which the pivotal element is an UAV collecting the data from the pole-mounted acquisition system.

This Section is structured as follows: Sub-Section 4.1.1 describes the measurement system, detailing in particular the drone, the pole-mounted acquisition system and their communication. All the experimental tests performed on the proposed system are listed in Sub-Section 4.1.2. The Sub-Section 4.1.3 presents and discusses the obtained results, while some conclusions are drawn in Sub-Section 4.1.4.

4.1.1 Measurement System Description

The developed test setup used to replicate the normal operation of a SA is shown in Figure 13.

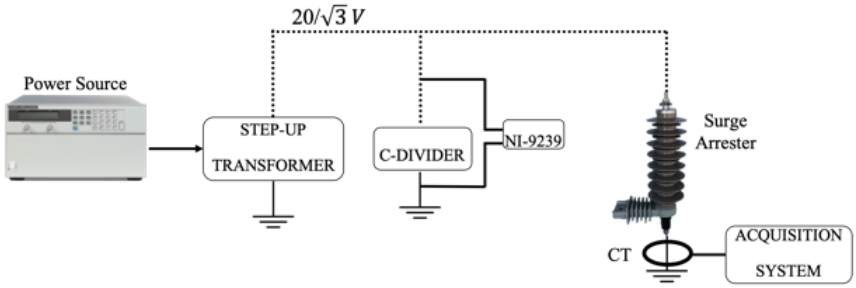

Figure 13 Simple schematic of the setup for measuring the SA leakage current.

It consists of:

- a programmable power source Agilent 6813B, which features up to 300 V RMS, 1750 VA from DC to 1 kHz. It assures a proper stability for the input sinusoidal voltage applied to the step-up voltage transformer. The voltage output channel features a gain error of 0.15 % and an offset error of 300 mV (at 50 Hz). The frequency accuracy is 0.01 % + 10 µHz.
- A step-up voltage transformer, which features 15/0.1 kV, 20 VA. Its low voltage terminals are connected to the power source. It rises the output voltage of the power source to the rated voltage of the surge arrester under test.
- The surge arrester under test; its rated voltage and breakdown current are 24 kV and 10 kA, respectively. In addition, it features a salt-proof external shell and an opening device which interrupts the circuit in less than 400 ms.

- The pole-mounted acquisition system (PMS). It is a STM32F411RE microcontroller-based instrument developed on the hardware employed for the energy meter presented in [55], which is briefly recalled in the following. It has been adapted for the current measurement on SAs and a LoRa®-based communication has been implemented. The LoRa® technology has been chosen because it can be implemented on low-power devices, it is possible to transmit data over long distances (some kilometers) and it operates on license-free frequency bands.
- A capacitive divider used to reduce the applied voltage for its measurement. It features a nominal ratio of 5981:1.
- A NI9239 24-bit Data Acquisition (DAQ) board, to measure the actual voltage applied to the SA. It is a ±10 V range DAQ which features a sample rate of 50 kSa/s, a gain error of ±0.03 % and an offset error of ±0.008 %.
- A NORATEL toroidal transformer TA015/06 used as a current sensor. Its main characteristics are listed in Table 4.1.
- A laptop (i7-8565U Processor, 16 GB RAM) for the measurement evaluation and computation.

Table 4.1 NORATEL toroidal transformer main characteristics

Frequency	50 Hz
Diameter	64.5 mm
Max Ambient Temperature	40 °C
Power	15 VA
Height	30.5 mm
Accuracy	1 %

In Figure 14 instead, the system for the data collection from the PMS to the drone is depicted. It consists of the UAV and the PMS communicating with the LoRa® technology. In the following subsections, details on the drone, the PMS and their communication are provided.

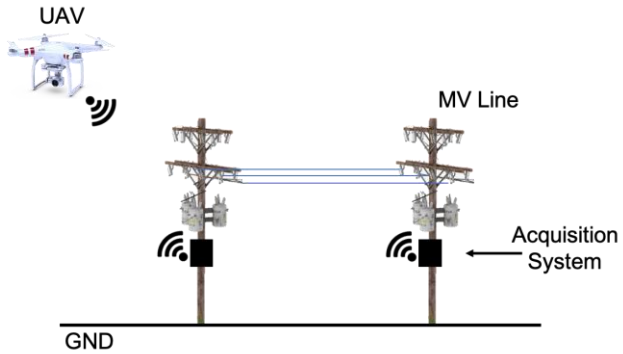

Figure 14 Schematic of the measurement data collection using the UAV.

4.1.1.1 Drone Technology and Wireless Communication

The UAVs (or drones) are day by day more integrated in several industrial application, increasing their efficiency and effectiveness. Different kind of UAV employments are listed in [56], including agriculture which has taken lot of advantages from their introduction [57]. Another example is provided by dangerous tasks, as the radioactive source analysis [58], which otherwise could not be performed. As almost all technology, also UAVs have some drawbacks. In particular, two of them are critical: UAVs cannot flight during bad weather conditions [59] and the beyond-visual-line-of-sight flight is not possible in many countries, or it requires difficult-to-obtain permits. The company Cardtech S.r.l. owns a fleet of drones and they have collaborated with our research group for this research activity. The fleet is composed by multirotor, fixed-wing and helicopter UAVs. Each kind of UAV has its peculiarities in terms of speed, flight duration and control flexibility. To satisfy the measurement requirements of the presented work, they have been equipped with the Aurel XTR-8LR100 transceiver module based on SX1276 chipset and LoRa® communication [60], [61]. This solution provides ultra-long-range communication, high interference immunity, high sensitivity and very low power consumption. The transceiver characteristics are listed in Table 4.2. The same kind of transceiver module has been integrated in the PMS to complete the communication chain.

Table 4.2 XTR-8LR100 communication system technical specifications.

Frequency range	869.4 – 869.65 MHz 868 – 868.6 MHz
Size	37x18x2.2 mm
Max Emitted Power	100 mW
Operating Temperature	-20 to +70 °C
Channels	7
Standard distance	6000 m
Operating Voltage	3.3 V

For sake of clarity and considering that the measurement data are transferred from the PMS to the UAV, the LoRa® module installed on the drone will be denoted as the receiver (RX), while the one installed in the PMS as the transmitter (TX).

4.1.1.2 The Pole-Mounted Acquisition System (PMS)

The PMS is based on the same hardware architecture employed for the multifunction energy meter developed in [55]. Its main purpose was to measure the energy in a LV three-phase system. The solution presented in [55] is based on a 32-bit microcontroller linked with an energy metering integrated circuit via I^2C bus and equipped with a Bluetooth module for connectivity. It can operate with 6 channels simultaneously at

8 kSa/s for the current and voltage measurement with an accuracy up to 0.1 %. For the present research, the device has been upgraded by the integration of the LoRa® communication module. Even though the device was equipped with Rogowski coils for the current measurement, for the SA monitoring application a toroidal ICT has been adopted. Given the magnitude and the bandwidth of the signal to be acquired, the ICT guarantees a better signal to noise ratio compared to the Rogowski coil. Moreover, to maximize the sensitivity of the sensor, the output voltage has been taken from the series of the two 115 V windings.

4.1.2 Experimental Tests

In this Sub-Section, three different experimental tests are described: the current sensors characterization, the current measurement on the SA and the validation of the communication between the PMS and the drone.

4.1.2.1 PMS - Current Sensor Characterization

A diagram of the measuring instrument characterization setup is shown in Figure 15.

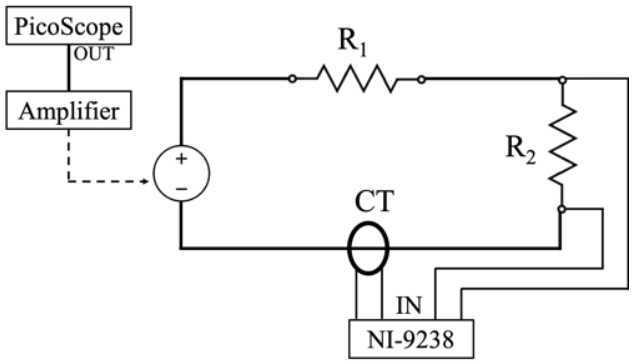

Figure 15 Schematic of the ICT characterization setup.

It consists of:

- the function generator (FG), embedded in the PicoScope 5442D (plus x10 custom amplifier to reach the required 1-13 V range), which provides sine wave signals at different frequencies and voltage amplitudes. The frequency range of the FG is 0.025 Hz to 20 MHz and the output voltage is ±2 V;
- a R_1 = 13.5 kΩ resistor in series to the FG, in order to reduce the current magnitude to the range of the one flowing in the ground terminal of the SA;

- a high-accuracy resistor R_1 = 0.5 kΩ obtained from the parallel of two VFR b1739-Z201T 1 kΩ resistors, featuring 0.01 % accuracy;
- the toroidal ICT connected to the PMS, used for the SA current measurement.

The test has been done generating 260 different sine wave signals, resulting from the combination of: (i) 20 frequency values (from 50 Hz to 1 kHz, with 50 Hz steps); (ii) 13 voltage amplitudes (from 1 V to 13 V, with 1 V steps). Then, the current flowing through the ICT I_m, has been obtained by dividing the voltage measured at the high accuracy resistor terminals V_{R2} by the resistor itself. As for the ICT output, the voltage at its secondary terminals V_{CT} has been acquired. Both voltages V_{R2} and V_{CT} have been acquired by two input channels of the NI9238 DAQ board at 50 kSa/s, 1 s time record. The NI9238 is a ±0.5 V range DAQ which features: sample rate of 50 kSa/s, gain error of ±0.07 % and offset error of ±0.005 %. For each of the 260 input signals, 30 measurements have been collected. By adopting the same setup presented in Figure 15, an additional characterization has been done. In particular, to consider the possible lower amplitudes of the third harmonic component in the SA leakage current, the resistors values have been changed. In other words, the characterization has been repeated with R_1 = 10 MΩ and R_2 = 1 kΩ, 0.01 % accuracy.

4.1.2.2 Current Measurements

By using the setup of Figure 13, the leakage current of the SA has been measured. The power source fed the step-up transformer to obtain up to 20/√3 kV voltage applied on the SA. This value has been chosen since 20 kV is the typical nominal value for line-to-line voltage in Italian distribution networks. The voltage is reduced and measured by mean of capacitive-divider and the DAQ, respectively. Afterwards, 30 measurements of the ICT output voltage have been acquired to compute the leakage current.

4.1.2.3 Wireless Communication Test

To test the communication between the PMS (TX) and the drone (RX), the RX has been moved along a track in urban/semi-urban landscape, while its geographical position has been tracked with a GPS. The goal of the test was to validate the quality of the data transmission when the distance and the relative speed between the RX and TX is varying. Therefore, a telegram containing a data payload of 250 bytes has been cyclically sent to RX, using a 1second cycle. The quality of the communication has been assessed by means of a byte error ratio (*BER*), for each received packet, which in this context has been defined as:

$$BER = \frac{\text{number of byte errors}}{\text{total number of received bytes}} \times 100\ \%\,. \tag{4.1}$$

4.1.3 Experimental Results

4.1.3.1 PMS - Current Sensor Characterization Results

Results of both the characterization test, in terms of measured reference current, are listed in Table 4.3. It contains the mean values $\tilde{I}_m$ of I_m and their associated uncertainty u_I for the two frequencies of interest, 50 Hz and 150 Hz.

Table 4.3 Mean values and uncertainty of the reference current I_m for the two frequencies of interest (50 Hz and 150 Hz).

	Frequency [Hz]			
	50		150	
Test Voltage [V]	$\tilde{I}_m$ [µA]	u_I [µA]	$\tilde{I}_m$ [µA]	u_I [µA]
1	49.12	0.05	0.35	0.01
2	98.31	0.07	0.71	0.01
3	147.36	0.09	1.06	0.01
4	196.5	0.1	1.41	0.02
5	245.6	0.1	1.76	0.02
6	294.6	0.2	2.11	0.02
7	343.7	0.2	2.47	0.02
8	392.8	0.2	2.82	0.02
9	442.0	0.2	3.17	0.02
10	491.1	0.2	3.52	0.02
11	540.2	0.3	3.87	0.02
12	589.3	0.3	4.22	0.02
13	638.1	0.3	4.58	0.02

Figure 16 and Figure 17 show the ensemble of parametric curves representing the average ICT output voltage $\tilde{V}_{CT}$ plotted against frequency. The former refers to the high-current range (obtained with R_1 = 13.5 kΩ and R_2 = 0.5 kΩ), while the latter refers to the low-current range, specific for the third harmonics (R_1 = 10 MΩ and R_2 = 1 kΩ).

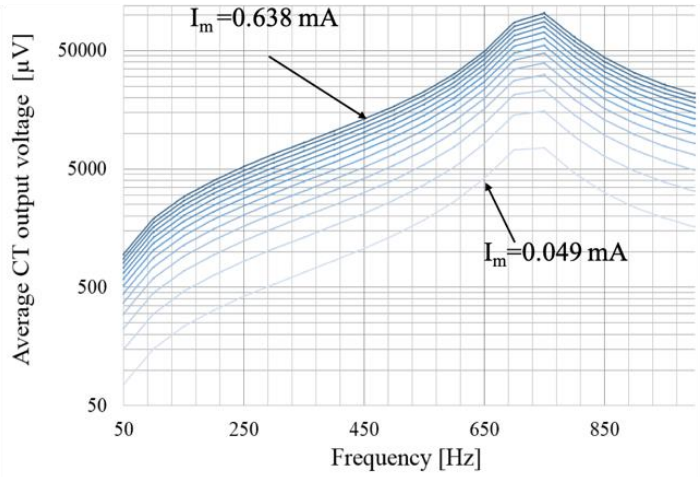

Figure 16 ICT output voltage vs. frequency with I_m as varying parameter. Case: R_1 = 13.5 kΩ and R_2 = 0.5 kΩ.

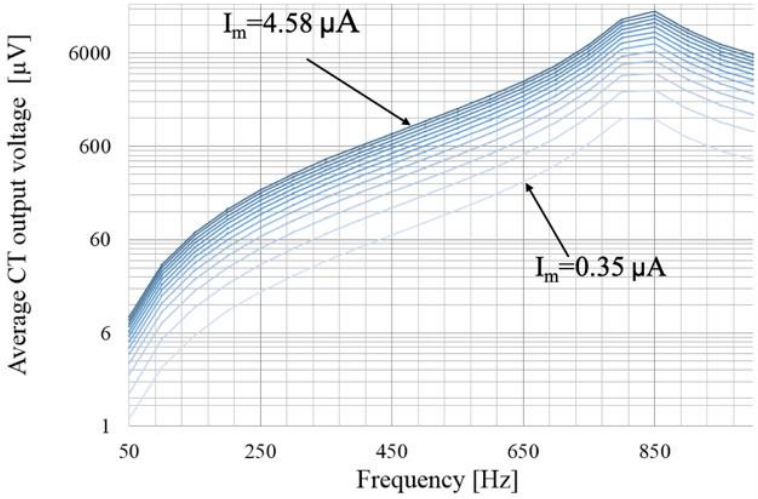

Figure 17 ICT output voltage vs. frequency with I_m as varying parameter. Case: R_1 = 10 MΩ and R_2 = 1 kΩ.

In both Figure 16 and Figure 17 the parameter is the current $I_m$and it can be noticed that:

- the higher the current, the higher the curve, denoting a monotonic behavior of $\tilde{V}_{CT}$. In particular, the latter ranges from (about) 76 μV to 950 μV at 50 Hz (in Figure 16) and from 6 μV to 72 μV at 150 Hz (in Figure 17).
- the measurement device under test reaches its peak sensitivity in correspondence of 750 Hz in Figure 16 and of 850 Hz in Figure 17.

To preliminary evaluate the $\tilde{V}_{CT}$ measurement goodness, the related standard deviation of the mean σ_{VC} has been computed. Results confirms that little variations of the quantities of interests can be detected with the

proposed setup. As a matter of fact, for all the current values within the measured range, all the computed σ_{VC} where below 1 µV and 0.1 µV, for the cases of Figure 16 and Figure 17, respectively. This holds for both the frequencies of interest, 50 and 150 Hz, while in the 700 – 850 Hz range the highest dispersion of the measurement is experienced. Once the σ_{VC} has been evaluated, it has been possible to compute the transfer function of the presented measurement device. This quantity has been named K_{PMS} and defined as the ratio of the primary current I_m to the output voltage V_{CT}, as follows:

$$K_{PMS} = \frac{I_m}{V_{CT}}. \tag{4.2}$$

The average value of K_{PMS}, referred to as $\widetilde{K}_{PMS}$, and its uncertainty u_K have been computed from the quantities measured in the characterization test. They are displayed as the blue curves in both Figure 18, for 50 Hz, and in Figure 19, for 150 Hz.

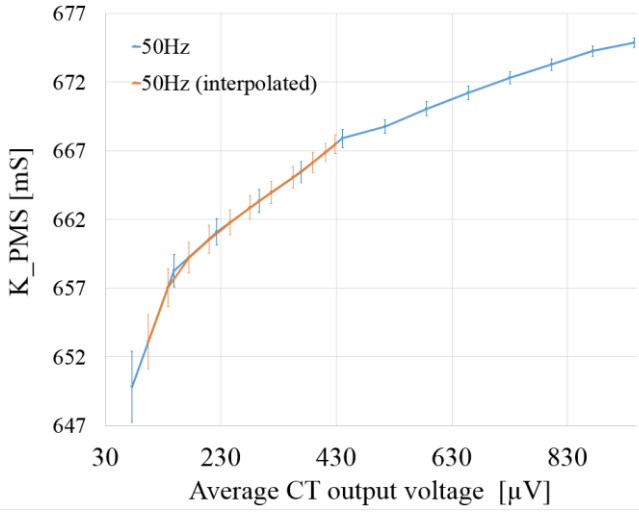

Figure 18 $\widetilde{K}_{PMS}$ at 50 Hz obtained from the characterization (blue curve) and the interpolation (orange curve).

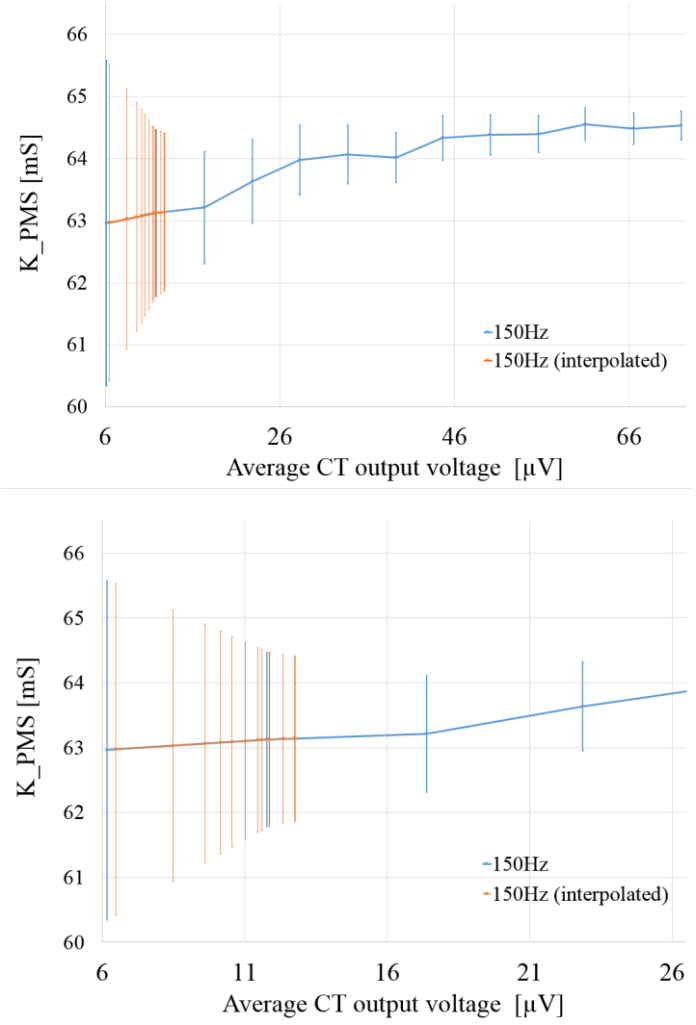

Figure 19 $\tilde{K}_{PMS}$ at 150 Hz obtained from the characterization (blue curve) and the interpolation (orange curve). The bottom plot is a magnification of the left-most part of the upper plot.

In both figures it can be highlighted that the toroidal transformer is working with a very low primary current, hence in correspondence of an operating point in the very beginning of the B-H iron curve. Hence, implying a predominant magnetization current contribution. In Figure 19, the upper graph represents the entire range of measurements performed during the characterization process. Instead, a zoom over the interest range in the bottom graph is presented.

4.1.3.2 Current Measurement

Once the transfer function K_{PMS} is known, the leakage current I_{leak} flowing through the SA can be computed by starting from the measured voltage V_{CT} at the ICT terminals. To compute the conversion, and for each measured voltage, the $\tilde{K}_{PMS}$ has been interpolated in correspondence of the measured $\tilde{V}_{CT}$; then its

associated uncertainty u_K has been computed. The obtained values are displayed as orange curves in both Figure 18 and Figure 19 for 50 Hz and 150 Hz, respectively. Finally, by means of Eq. (4.2) the leakage currents have been computed and listed in Table 4.4.

Table 4.4 Mean values and standard deviations of $\bar{I}_{Leak}$ for the two frequencies of interest (50 Hz and 150 Hz).

	Frequency [Hz]			
	50		150	
Test Voltage [kV]	$\tilde{I}_{Leak}$ [µA]	u_{IL} [µA]	$\tilde{I}_{Leak}$ [µA]	u_{IL} [µA]
3	68.2	0.2	0.57	0.02
4	91.2	0.2	0.60	0.02
5	114.9	0.2	0.63	0.02
6	138.2	0.2	0.66	0.03
7	162.6	0.2	0.69	0.03
8	186.0	0.3	0.71	0.03
9	210.7	0.3	0.69	0.03
10	236.0	0.3	0.71	0.04
11	259.6	0.3	0.74	0.04
11.55	274.4	0.3	0.77	0.04
12	285.9	0.3	0.77	0.04

Table 4.4 contains the mean values $\tilde{I}_{Leak}$ of the current along with their associated uncertainty u_{IL} for both the frequencies of interest, 50 and 150 Hz. The results presented in Paragraphs 4.1.3.1 and 4.1.3.2 suggest that the presented measurement device equipped with the ICT is suitable to be employed as a monitoring device for the leakage current of the MV SAs employed in the distribution network. However, given the magnitude of the ICT output voltage, a proper signal conditioning is needed for the on-site deployment, which will be further analyzed in future work.

4.1.3.3 Wireless Communication Test Results

This Paragraph reports the results of the wireless communication tests based on the LoRa® protocol. In Figure 20 there are two different curves: the black one is the distance between the moving RX and the fixed TX against time. The red one instead, is the computed *BER* during the RX movement along the chosen urban/semi-urban track.

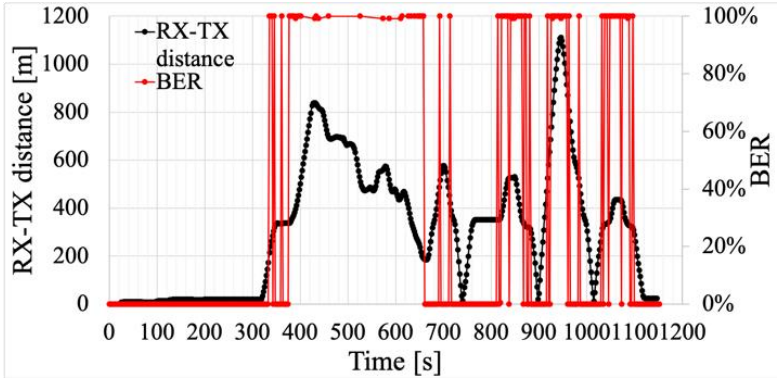

Figure 20 *BER* and distance between RX and TX plotted against time

From this plot three considerations arise: (i) during the time interval 350-650 s the communication was severely impaired due to presence of many buildings in the line-of-sight path between the RX and TX; (ii) if the RX-TX distance is greater than 300 m, then the communication cannot be considered reliable in the considered landscape. This does not compromise the proposed solution because the drone will fly much closer to the PMS than 300 m (few tens of meters); (iii) the RX's relative speed was 70 km/h at 900 s, this means that the LoRa® protocol is capable to successfully transfer data when the RX and the TX are moving at such a relative speed. Considering this last comment, the fixed-wing drones can be conveniently operated at 70 km/h and, in the MV overhead line monitoring applications, the drone shall overfly the line at a 30-40 m altitude, with no obstacles in the middle. The experimental results show that the low-power communication modules under test are a very valid solution for the presented application.

4.1.4 Conclusions

In this Section a measurement system for asset diagnostics composed by an UAV collecting the measurement data, and by an acquisition system has been proposed and validated. The developed system allows measuring the leakage current flowing through the MV surge arresters in charge for the protection of the pole-mounted equipment. The UAV may collect measurement data from the acquisition system by means of wireless communication technology, such as LoRa®. The presented results validate the concept and the feasibility of such an innovative measurement system.

Chapter 5 Measurements for Grid Monitoring

In this Chapter the wide research carried out on the measurements supporting the grid monitoring is discussed. As introduced in Chapter 1, the goal is to provide reliable measurement values of the electric quantities and this is possible thanks to the thorough metrological characterization of the instrumentation and the sensors, such as those presented in Chapter 2. This Chapter is structured as follows: a metrological characterization of the smart energy meters under different realistic off-nominal network conditions, and the proposal of non-standard test procedures are presented in Section 5.1; an investigation on the accuracy behavior of the inductive current transformers in presence of harmonic distortion and the deducible information on the corresponding *THD* uncertainty are shown in Section 5.2; finally, in Section 5.3, a PMU implemented in a real-time simulator (RTS) has been calibrated by means of a PMU calibrator developed by the author, showing the relevance of the accuracy verification of the devices, such as PMUs, modeled in these simulators which are more and more employed for enhancing grid operations and monitoring.

5.1 Energy Meters Characterization in Off-Nominal Network Operation

The observability of the distribution network has become of paramount importance in the context of the network transition towards the Smart Grid concept [55], [62]–[64]. The electric energy measurement is a central task, since knowing accurately the energy consumed/generated by users/producers across the network is a key information to effectively control stability and to carry out fair energy billing [1], [32], [65]. In addition, the knowledge of such critical quantities can be used to run several algorithms used to manage and control the network [66]–[70]. However, the growing presence of connected renewable energy resources and non-linear loads impairs the electric power quality, raising challenges for the ITs and EMs performance. Nowadays the electronic EMs are replacing the old electromechanical induction meters. Although the latter instruments have an acceptable behavior when distortion is present [71], the EMs are preferred because they enable utilities and consumers to perform “smart” operations, such as remote readings, computation of many power quality parameters, managing real-time pricing and smart load control [41]. Still, given the EMs’ complex nature due to the variety of algorithms and technologies that can be implemented, the EMs behavior when exposed to non-nominal yet unexceptional operating conditions shall be carefully evaluated and studied; even with regards to the applicable standards [72]–[74]. To this end, many studies have been conducted on this subject. In [75] EMs’ response to harmonic active power components up to 3 kHz has been tested. In [71] a calibration procedure for EMs based on the generation of randomly distorted signals is proposed, while in [76] a portable instrument for on field EM calibration has been developed. In [77], [78], instead, a metrological characterization of EMs for non-sinusoidal reactive energy was presented. Finally, [79] and [80] have dealt

with the testing of one EM (under non-sinusoidal conditions) and proposed a new set of tests, respectively; whereas [81] has approached the EM uncertainty from the point of view of its model.

The aim of this research is to contribute, in a different way, to the definition of test signals to be applied to the energy meters. The idea came from the current literature and the standards, in which the described signals are stressing specific situation that may happen during the network operation. However, to our knowledge, none of them tackled the issue from a more realistic point of view. Therefore, the goal of the presented research is to propose a possible procedure based on test waveforms that try to emulate as far as possible and with a simple methodology the daily behavior of the network, since it is author's and research group colleagues' firm belief to pursue this testing paradigm. Support to this choice is given by the current literature which is facing the same issue of providing actual or more realistic waveforms to the devices under test. For example, in [82]–[84] has been done on current transformers, while in [85], [86] for the voltage ones.

In this Section, the metrological characterization of different LV off-the-shelf MID-compliant class B single-phase EMs has been investigated and the results have been published in [87], [88]. These EMs, rated as MID Class B, have been chosen because they are the same as the new revenue meters deployed by the main Italian distribution system operators [89]. In particular, the research on the metrological characterization of the EMs has focused on: the effects of long duration frequency variations around the rated frequency, in Sub-Section 5.1.2; the effects of realistic distorted current and voltage waveforms, in Sub-Section 5.1.3. But first, in Sub-Section 5.1.1, an overview of the regulatory context concerning the EMs is given.

5.1.1 Regulatory Context

In March 2014, the European Directive 2014/32/EU [90] was released, amending the previous version issued in 2004. This document is also known as Measuring Instruments Directive (MID) and it concerns all the measuring instruments "*responding to reasons of public interest, public health, safety and order, protection of the environment and the consumer, of levying taxes and duties and of fair trading, which directly and indirectly affect the daily life of citizens*", including the revenue active electrical energy meters. The EN 50470 series [91]–[93] is the harmonized standard in force for electricity metering equipment. It is related to IEC 62052 [94] and IEC 62053 [95], [96] with modifications in order to be compliant with the MID. In particular, the specifications for the electronic active energy meters are stated in the EN 50470-3 [93], where the three accuracy classes C, B and A from the directive are described. Nevertheless, some electronic energy meters are marked also with the IEC accuracy class, thus, a brief comparison between the accuracy requirement of the two standards is carried out. The IEC 62053-22 and 62053-21 prescribe four different accuracy classes: 0.2S, 0.5S, 1, 2 [95], [96]. Both sets of accuracy classes are based on a percentage error *e%*:

$$e\% = \frac{E_m - E_t}{E_t} \times 100 \tag{5.1}$$

where E_t is the reference energy with traceable uncertainty and E_m is the energy registered by the meter.

Table 5.1 Percentage error limits for the accuracy classes A, B, C (EN 50470-3) and 2, 1, 0.5S, 0.2S (IEC 62053-21-22) at reference conditions

	EN 50470						**IEC 62053**							
	Class A		**Class B**		**Class C**		**Class 2**		**Class 1**		**Class 0.5S**		**Class 0.2S**	
	Power Factor						***Power Factor***							
Value of current $i=I/I_{ref}$ [p.u.]	1	0.8 cap, 0.5 ind.	1	0.8 cap, 0.5 ind.	1	0.8 cap, 0.5 ind.	1	0.5 ind.	1	0.8 cap, 0.5 ind.	1	0.8 cap, 0.5 ind.	1	0.8 cap, 0.5 ind.
$0.01 \le i \le 0.02$											±1.0		±0.4	
$0.02 \le i \le 0.03$											±1.0	±1.0	±0.4	±0.5
$0.03 \le i \le 0.05$					±1.0						±1.0	±1.0	±0.4	±0.5
$0.05 \le i \le 0.1$	±2.5		±1.5		±1.0		±2.5		±1.5		±0.5	±1.0	±0.2	±0.5
$0.1 \le i \le 0.2$	±2.0	±2.0	±1.0	±1.0	±0.5	±0.5	±2.0	±2.5	±1.0	±1.5	±0.5	±0.6	±0.2	±0.3
$0.2 \le i \le 5$[a]	±2.0	±2.0	±1.0	±1.0	±0.5	±0.5	±2.0	±2.0	±1.0	±1.0	±0.5	±0.6	±0.2	±0.3

[a] For the IEC standard classes, $i = 5$ as upper limit of the current range is just an arbitrary assumption, since there are no specific mandatory values required.

In Table 5.1 the percentage error limits for the accuracy classes prescribed by EN 50470-3, IEC 62053-21 and IEC 62053-22 at reference conditions are shown as function of the load, expressed as a combination of current and power factor (PF). The per-unit system is adopted for the expression of the current ranges, where the base quantity is the meter rated current I_{ref}. The classes 0.5S, 1, 2 are comparable, respectively, to classes C, B and A. The accuracy requirements for 0.2S are the most demanding. Classes B and A are more demanding than classes 1 and 2, in which higher permissible percentage error is tolerated in the range $0.1 \cdot I_{ref} \le I \le 0.2 \cdot I_{ref}$ when load PF differs from 1. Moreover, there is no accuracy prescriptions for class 2 meters if a capacitive load is present. Therefore, not exceeding the class B and A limits ensure that class 1 and 2 limits are not exceeded. Concerning the classes C and 0.5S, one class does not cover the other: class 0.5S applies accuracy constraints on a current range below the lower limit identified by the class C. Nevertheless, class C demands a smaller percentage error for currents $\ge 0.1 \cdot I_{ref}$ and $PF \ne 1$. The highest current value for which the accuracy requirements are valid is I_{max} which is $\ge 5 \cdot I_{ref}$ for the EN 50470, while a "preferably integer multiple" of I_{ref} is suggested in the IEC 62052-11 [94]. The IEC 62053-22 and EN 50470-3 make no distinctions between transformer operated and direct connected meters, while the IEC 62053-21 does: allowed percentage errors for transformer operated meters are the same as the direct connected ones but are defined over slightly different current ranges. In Table 5.1 only direct connected meters are considered. Please note that the accuracy classes definition is given assuming the validity of some reference conditions, which specify the rated values for the influence quantities, e.g., ambient temperature, voltage, frequency, and electromagnetic

disturbances. The reference conditions for IEC and EN standards are the same for the comparable classes (1 and B, 2 and A, 0.5S and C). The main differences between the two standards can be found in the evaluation of the influence quantity impacts on the accuracy. For instance:

- IEC 62053-22 does not prescribe the "DC and even harmonics" and "odd harmonics" tests.
- IEC 62053-21 and -22 do not specify test settings and disturbance values for RF electromagnetic fields, conducted disturbances induced by RF fields, fast transient burst and damped oscillatory wave immunity.
- IEC 62053-21 and -22 do not require a test with capacitive load when frequency and voltage variations are applied.

However, the most noticeable difference introduced by the MID is the definition of the composite error:

$$e_c = \sqrt{e^2(I,\ cos\varphi) + \delta^2(T,\ I,\ cos\varphi) + \delta^2(U,\ I,\ cos\varphi) + \delta^2(f,\ I,\ cos\varphi)} \tag{5.2}$$

where:

- $e^2(I, cos\varphi)$ is the percentage error at reference conditions and at a certain load;
- $\delta^2(T, I, cos\varphi)$ is the additional error due to the temperature variation at the same load;
- $\delta^2(U, I, cos\varphi)$ is the additional error due to the voltage variation at the same load;
- $\delta^2(f, I, cos\varphi)$ is the additional error due to the variation of frequency at the same load.

The composite error e_c contemporarily considers multiple effects on the accuracy class and it shall not exceed the maximum permissible errors (MPE) detailed in Table 7 of the EN 50470-3 standard [93].

5.1.2 Testing in Off-Nominal Frequency Conditions

The standards overviewed in the Sub-Section 5.1.1 state also the requirements concerning the frequency testing. The prescribed procedure indicates to apply a ±2 % variation on the test waveform frequency in respect of the rated frequency. The maximum percentage error values admitted on the energy measurement induced by the frequency variations are summarized in Table 5.2. Note that no capacitive load is considered for IEC classes, class C current range is wider than class 0.5S one and, foremost, no indications about duration of the test are specified.

Table 5.2 Frequency Variation Test Case

Value of current $i=I/I_{ref}$ [p.u.]	**PF**	**Limits of additional percentage error for meters of class index ± [%]**						
		A	**B**	**C**	**2**	**1**	**0.5S**	**0.2S**
$0.03 \leq i \leq 0.05$	1			0.2				
$0.05 \leq i \leq 5$[a]	1	0.8	0.5	0.2	0.8	0.5	0.2	0.1
$0.1 \leq i \leq 5$[a]	0.5 ind.	1.0	0.7	0.2	1.0	0.7	0.2	0.1
	0.8 cap.	1.0	0.7	0.2				

[b.] For the IEC standard classes, i = 5 as upper limit of the current range is just an arbitrary assumption, since there are no specific mandatory values required.

The present research explored long duration frequency variations around the rated frequency to provide possible alternatives to the test offered by the standards, and that could reproduce somehow a more realistic condition.

5.1.2.1 Test Setup Description

The measurement setup developed to test the active electrical energy meters is shown in Figure 21.

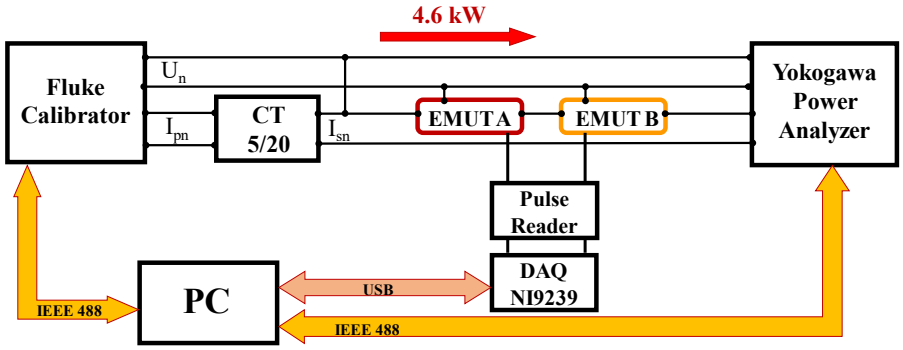

Figure 21 Measurement setup for the EMs off-nominal frequency tests.

It consists of:

- A calibrator Fluke 6105A (1000 V, 20 A). It has an accuracy of 75 ppm for both the current and the voltage amplitudes, while 50 ppm for the frequency and 10 µrad for the phase. It has been used to assure stability for the voltage (230 V), current (5 A) and frequency (see Paragraph 5.1.2.2) inputs.

- A high-accuracy power analyzer Yokogawa WT3000E (1000 V, 30 A). Its accuracy is ± (0.01 % of reading + 0.03 % of range) for power in the 45 Hz ≤ f ≤ 66 Hz range and it has been employed as reference for the active energy measurement.
- A 5 VA current transformer (ICT) with a ratio 20:5. It rises the current generated by the calibrator to 20 A and it feeds the energy meters under test and the power analyzer. The ICT burden is composed of the resistances of shunt resistors in the current measuring channel inside the energy meters under test and inside the power analyzer. The resistance is small enough to let the current to be boosted, there is no interest in maintaining strictly the ICT class performance since the ICT is not involved in the measurement chain.
- The energy meter under test A (EMUT A), which is a single-phase energy meter (U_n=230 V, I_{max}=45 A) certified as MID class B, according to the EN 50470-3, and as class 1, according to the IEC 62053-21. The device has a RS485 serial output and an optical test output at 1000 impulses per unit of energy (imp/kWh).
- The energy meter under test B (EMUT B), which is a single-phase energy meter (U_n=230 V, I_{max}=40 A) certified as MID class B, according to the EN 50470-3. The device has a static pulsed test output at 1000 imp/kWh.
- A pulse reader circuit, made of two simple signal conditioning circuits based on a photodetector (for EMUT A) and a pull-up resistor (for EMUT B) cascaded with logical ports acting as voltage regulators to obtain 0-5V at the output. The pulse reader circuit contribution to uncertainty is negligible compared to the one due to the test outputs over the whole measuring time interval, as detailed in the Sub-Paragraph 5.1.2.1.1 below.
- a NI9239 24-bit data acquisition board (DAQ), to record the test outputs of the two energy meters under test. It is a ±10 V range DAQ which features a sample rate of 50 kSa/s, a gain error of ±0.03 % and an offset error of ± 0.008 %. It has been used to acquire the waveform of the signal coming from the pulse reader circuit output, thus allowing the count of the impulses.
- PC for test automation and measurements analysis.

5.1.2.1.1 Pulse Reader Circuit Uncertainty considerations

It is important to assess the uncertainty affecting the process of acquiring the EMs' test output. The acquisition process can be considered error-free, according to the following considerations.

- The test output signals' features are described in standards EN 62052-11 [94] (for optical test output) and EN 62053-31 [97] (for static test output). The EN 62053-31 prescribe the pulse signal time duration t_{ON} to be ≥ 30 ms and the time between two pulses t_{OFF} ≥ 30 ms; while

the EN 62052-11 prescribe the pulse signal time duration t_{ON} to be ≥0.2 ms and the time between two pulses $t_{OFF} \geq 0.2$ ms. In EMUT A datasheet the minimum flashing light period is declared to be 90 ms, therefore a $t_{ON} \approx 40$ ms could be expected. However, let us assume the worst case where $t_{ON} = 0.2$ ms.

- This pulse is expected to be observed about every 0.78 s, since the power flowing through the meter is 4.6 kW and the test outputs provide with 1 pulse per watthour.

Given these time scales, the pulse reader circuits bandwidth is not a problem. Moreover, the adopted DAQ sampling rate is 50 kSa/s, which allows a finely pulse recording (at least 10 points for each pulse signal time duration t_{ON} are collected in the worst scenario). To prevent bad counting due to noise, the chosen NOT logical port circuits, employed as voltage regulators, features the Schmitt trigger and the threshold to detect the pulse is set at 2.5 V. In such conditions the system "pulse reader circuit + DAQ" is analogous to the performance of a properly implemented digital counter, which accuracy is known to be ± 1 (the least significant bit is the one affected by uncertainty). The DAQ acquiring the EMs' test output and the reference energy meter query are performed as consecutive operations by LabVIEW. Thus, given the expected pulse periodicity of 0.78 s, the expected error of the implemented virtual digital counter described above is ± 1. Reminding that each pulse corresponds to 1 Wh, it means that if the EM measures 36800 Wh, then the error caused by considering the pulsed signal is ± (1/36800) = $3 \cdot 10^{-5}$. Such an error is lower than the accuracy of the reference energy meter.

5.1.2.2 Experimental Tests

In light of what described in the previous sections, a new set of tests on the energy meters has been developed and performed. Such tests are aimed at assessing the meters behavior when the power system frequency differs from the rated value, which is not an uncommon scenario during the actual power network operation. Three different test cases were run on the setup illustrated in Figure 21 and they are detailed in the paragraphs below. In all the three cases, the calibrator generated the EMUTs' reference voltage U_n=230 V and the current I_{pn}= 5 A, with relative phase displacement equal to zero (PF=1). The current I_{pn} was stepped-up by the ICT to I_{sn}= 20 A and then fed to the EMUTs. I_{sn} was chosen since it is representative of the intermediate value of the EMs' current range [I_{ref}, I_{max}]. The potential of the secondary winding of the ICT has been raised to U_n in order to obtain a phantom power supply for the EMUTs, that is, just a very small fraction of the active power measured by the meters (about 4.6 kW) is actually dissipated, without the need of a high-power dummy load. The active energies E_{mA} and E_{mB} measured by EMUT A and EMUT B, respectively, are compared against E_t, the energy measured by the reference power analyzer. The synchronization of the readings from the EMUTs and the power analyzer was implemented by starting the pulse counter acquisition in parallel with the energy

computation performed by the power analyzer. The active energy readings were triggered when the electrical quantities provided by the calibrator are already in steady state.

5.1.2.2.1 Nominal frequency – calibration measurement

The first test case consisted in running the Fluke 6105A at f_r=50 Hz to carry out the calibration of EMUTs at nominal conditions and to check their measurement repeatability. The test end condition is:

$$E_{mA}=36800 \text{ Wh} \vee E_{mB}=36800 \text{ Wh} . \tag{5.3}$$

Since a "phantom" power of 4.6 kW is generated, the test end condition is matched after about 8 hours. Such a long-duration test makes negligible the contribution to uncertainty due to each test output reading compared to the overall energy measured by each EMUT. This procedure was repeated 7 times. Therefore, for each repetition, the calibration coefficients $K_{EM\,A}$ and $K_{EM\,B}$ were computed as:

$$K_{EM\,A}=\frac{E_{mA}}{E_t} , K_{EM\,B}=\frac{E_{mB}}{E_t} , \tag{5.4}$$

where E_{mA} and E_{mB} are the active energy readings from EMUT A and EMUT B, respectively, and E_t is the related reading of the power analyzer reading. Then, the mean values $\overline{K}_{EM\,A}$, $\overline{K}_{EM\,B}$ and the standard deviations of the mean $\sigma_{K_{EM\,A}}$, $\sigma_{K_{EM\,B}}$ over the 7 values were evaluated. Also, a verification of the percentage error defined in (5.1) was carried out.

5.1.2.2.2 Single non-integer frequencies

In the second test case, non-integer frequencies were adopted because also such frequencies can be observed in the network. The adopted values were 48.76 Hz and 50.13 Hz, which fall both in the frequency range 48 ÷ 52 Hz. This range is adopted also in the test described in the next Sub-Paragraph 5.1.2.2.3 and it has been designed starting from the worst-case frequency variations defined by the EN 50160. The choice of the two values 48.76 Hz and 50.13 Hz is arbitrary and aimed at avoiding integer values. Two digits after the decimal point were set because of the calibrator resolution. The test procedure and the test end condition are equal to the one described in the Sub-Paragraph 5.1.2.2.1 above. This test case was repeated for 4 times. After that, the mean calibration coefficients $\overline{K}_{EM\,A}$ and $\overline{K}_{EM\,B}$ were applied to the correspondent readings, obtaining E^*_{mA} and E^*_{mB}. Finally, the percentage error defined in (5.1) was computed for both the EMUTs to check the non-integer frequency impact on the measurement.

5.1.2.2.3 Random multiple frequencies

The third test case goal is to simulate a realistic scenario in which the power frequency randomly oscillates around the nominal frequency. This was achieved by applying for a short time interval a frequency randomly extracted from a uniform probability distribution defined over the range 48 ÷ 52 Hz. After that, a new random frequency was applied, and so on for about 8.5 hours. The following condition was adopted to decide when to generate a new random frequency:

$$E_{mA}=800 \text{ Wh} \vee E_{mB}=800 \text{ Wh} . \tag{5.5}$$

The calibration coefficients were applied to the EMUT readings, obtaining E^*_{mA} and E^*_{mB} and finally the percentage error due to frequency variation was evaluated with (5.1).

5.1.2.3 Experimental Results

5.1.2.3.1 Nominal frequency – calibration measurement

In Table 5.3 the data from the EMUTs calibration is reported. It is possible to notice that calibration coefficients $K_{EM\,A}$ and $K_{EM\,B}$ present a limited variation (considering the standard deviation of the mean) around the mean value, showing good repeatability. Both the EMUTs are compliant with their accuracy class at nominal conditions.

Table 5.3 EMUTs calibration at nominal frequency condition

	E_t [Wh]	E_{mA} [Wh]	E_{mB} [Wh]	$K_{EM\,A}$ [-]	$K_{EM\,B}$ [-]	e_A% [%]	e_B% [%]
	36475.4	36396	36800	0.9978	1.00890	-0.22	0.89
	36472.9	36394	36800	0.9978	1.00897	-0.22	0.90
	36470.7	36403	36800	0.9981	1.00903	-0.19	0.90
	36479.0	36443	36800	0.9990	1.00880	-0.10	0.88
	36480.1	36448	36800	0.9991	1.00877	-0.09	0.88
	36470.9	36380	36800	0.9975	1.009023	-0.25	0.90
	36474.3	36424	36800	0.9986	1.00893	-0.14	0.89
$\bar{K}_{EM}$				0.9983	1.00892		
$\sigma_{K_{EM}}$				$2\cdot10^{-4}$	$4\cdot10^{-5}$		

5.1.2.3.2 Single non-integer frequencies

In Table 5.4 the data obtained from the energy measurements is listed. The magnitude of the percentage error is greater than the standard deviation of the calibration coefficients $\overline{K}_{EM\,A}$, $\overline{K}_{EM\,B}$ determined in Sub-Paragraph 5.1.2.3.1, especially for EMUT B, for whom $e_B\%$ is around 40 times higher than the variation of $\sigma_{K_{EM}\,B}$. This means that the percentage error is not due to the approximation arising from considering a mean value for the calibration coefficients. In other words, it can be stated that a steady off-nominal frequency perturbs the EMUTs active energy measurement, even though they are still compliant with their accuracy class.

Table 5.4 EMUTs percentage error at off-nominal frequency condition

Frequency [Hz]	E_t **[Wh]**	E^*_{mA} **[Wh]**	E^*_{mB} **[Wh]**	$e_A\%$ **[%]**	$e_B\%$ **[%]**
48.76	36419.2	36439.1	36474.8	0.055	0.15
	36414.9	36442.1	36474.8	0.075	0.16
	36414.0	36440.1	36474.8	0.072	0.17
	36405.4	36431.1	36474.8	0.071	0.19
50.13	36428.7	36430.1	36474.8	0.0039	0.13
	36427.4	36447.1	36474.8	0.054	0.13
	36427.6	36450.1	36474.8	0.062	0.13
	36428.7	36419.1	36474.8	-0.026	0.13
	36433.3	36455.2	36474.8	0.060	0.11

5.1.2.3.3 Random multiple frequencies

The randomly generated frequencies are plotted against time in Figure 22 and the corresponding data from the energy measurement are shown in Table 5.5.

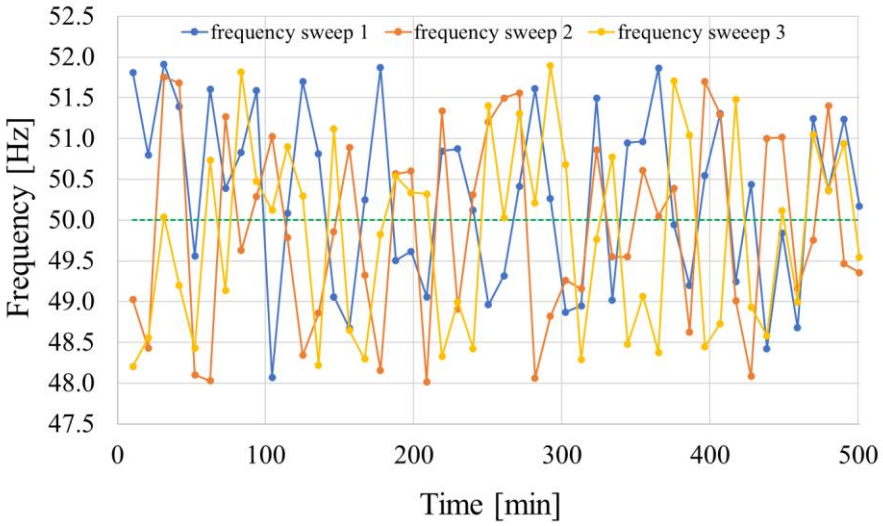

Figure 22 Randomly generated frequency sweeps.

Table 5.5 EMUTs percentage error at random frequency variations

Frequency	E_t **[Wh]**	E^*_{mA} **[Wh]**	E^*_{mB} **[Wh]**	$e_A\%$ **[%]**	$e_B\%$ **[%]**
Sweep 1	38032.8	38039.5	38060.6	0.018	0.073
Sweep 2	38039.6	38056.4	38060.6	0.044	0.055
Sweep 3	38021.1	38039.5	38060.6	0.048	0.10

The variation due to the random frequency sweeps lead to a smaller impact on the percentage error if compared to the one due to the single non-integer frequencies. This behavior can be explained by the fact that in the single non-integer frequency case, the EMUTs could be subjected to a frequency that particularly affects their measurement, as acting on a weak spot. Whereas, when the meters experience the random frequency variation, the percentage error is influenced in different ways: it could be higher with the "critical" frequencies and it could be lower with, for instance, integer frequencies. Consequently, the frequency variation effect on the overall energy measurement is much more mitigated.

5.1.2.4 Conclusions

The presence of distortion and power quality issues are a challenging scenario for the energy meter performance, thus thorough testing procedures shall be developed. The research reported in this Sub-Section, proposes a new test procedure for the assessment of active energy meters behavior in off-nominal frequency conditions, by providing the energy meter with non-integer frequencies and randomly generated frequencies. The presented results show that it is worth to improve the standard testing concerning the frequency variation

effects on active energy measurements. Such tests shall consider (as much as possible) the real-world operating conditions of power networks.

5.1.3 Testing under Realistic Distorted Current and Voltage Distortion

The standards overviewed in the Sub-Section 5.1.1 also deal with the EMs calibration in presence of harmonic disturbances. Three different categories of disturbances can be found in the standards EN 50470-3 and IEC 62053-21: (i) harmonic components in the current and voltage circuits; (ii) DC and even harmonics in the current circuit; (iii) odd harmonics in the current circuit. In the IEC 62053-22 only test (i) is defined. Moreover, a test for current sub-harmonics is prescribed, but it will not be discussed since it deals with a case that is not under the scope of the present research. The additional percentage error limits admitted for the above tests are listed in Table 5.6.

Table 5.6 Additional percentage error limits for the harmonic disturbance tests regarding the accuracy classes A, B, C (EN 50470-3) and 2, 1, 0.5S, 0.2S (IEC 62053-21, -22)

Disturbance	**Value of current**	***PF***	**Limits of additional percentage error for meters of class index ± [%]**						
			A	**B**	**C**	**2**	**1**	**0.5S**	**0.2S**
Harmonic components in the current and voltage circuits	0.5 I_{max}	1 [a]	1.0	0.8	0.5	1.0	0.8	0.5	0.4
DC and even harmonics in the a.c. current circuit	$\frac{I_{max}}{\sqrt{2}}$	1	6.0	3.0	1.5	6.0	3.0	-	-
Odd harmonics in the a.c. current circuit	0.5 I_{ref}	1	6.0	3.0	1.5	6.0	3.0	-	-

a. The PF here is the harmonic PF for the considered harmonic order.

The peculiarity of all the harmonic disturbance tests for the active EMs calibration is the fact that a standard test waveform has been chosen, distinguished by a very specific harmonic content. For instance, in the disturbance category (i) the voltage and current waveforms are both formed by a fundamental and a 5th harmonic component, but with different Total Harmonic Distortion factor (THD): 10 % for the voltage and 40 % for the current. The fundamental and the 5th components of voltage are in phase at the positive zero crossing and the current components are in phase with the same-order voltage components. As for the disturbance category (ii), the standards establish a half-wave rectified current waveform, composed just by even harmonics with a THD ≈ 87 %, while for the disturbance category (iii), a phase-fired alternate current waveform, made

by odd harmonics and characterized by a THD ≈ 113 % is defined. In Figure 23 and Figure 24 the time-domain signal and the magnitude spectrum of the mentioned test waveforms are depicted, respectively.

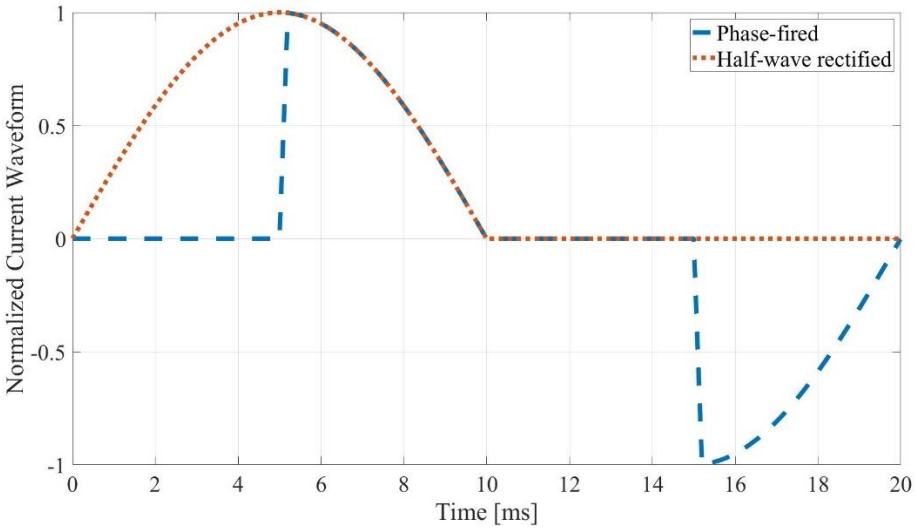

Figure 23 Odd and even harmonic disturbance tests waveforms defined in EN 50470-3 and IEC 62053-21.

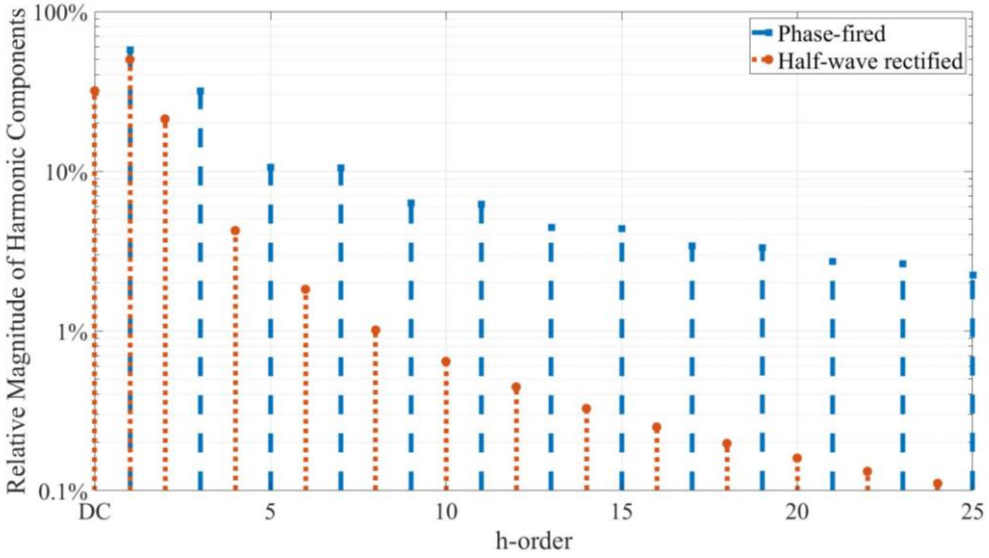

Figure 24 Odd and even harmonic disturbance tests waveforms magnitude spectra defined in EN 50470-3 and IEC 62053-21.

This research has attempted to design realistic test waveforms, starting from the standards [24], [25]. As in Sub-Section 5.1.2 the goal is to provide possible alternatives to the standard tests, pursuing more realistic condition and investigate the EMs accuracy behavior in terms of the error index defined in the standards.

5.1.3.1 Measurement System Description

The experimental tests have been carried out by means of the test setup illustrated in Figure 25, analogous to the one Figure 21, except for an additional energy meter under test (EMUT) connected in series to the current circuit and in parallel to the voltage one.

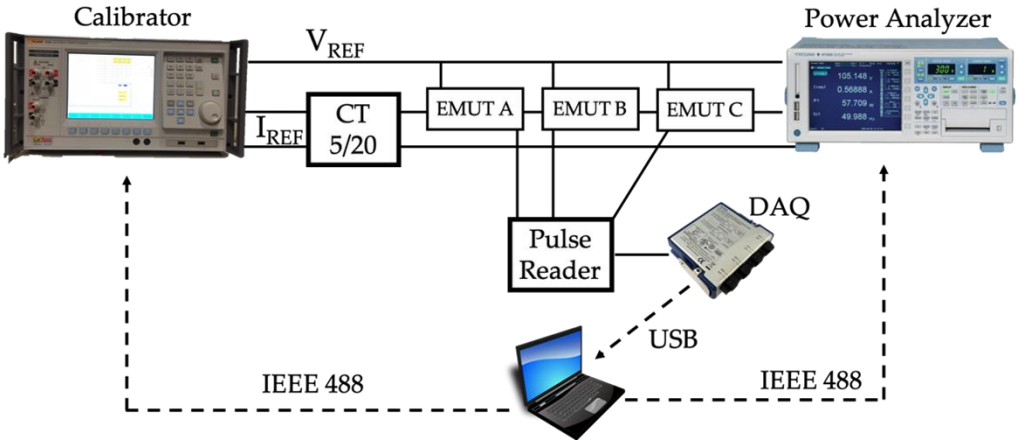

Figure 25 Adopted measurement setup for testing the three off-the-shelf EMs.

The full information concerning the test setup is already described in Paragraph 5.1.3.1, in the following just a brief summary of the employed equipment is reported for readability and the specifications of the new EMUT are listed. A Fluke 6105A calibrator provided the reference voltage and current inputs. The voltage is directly applied across the EMUTs terminals, while the current is stepped-up by means of a 5 VA 5:20 current transformer (ICT), feeding the EMUTs. A high-accuracy power analyzer Yokogawa WT3000E, of which accuracy is ± (0.01 % of reading + 0.03 % of range + 0.02 % of time reading), served as reference for the active energy measurement. The three EMUTs, identified as EMUT A, B and C, are single-phase MID class B compliant, according to the standard EN 50470-3. In spite of the same rated voltage U_n=230 V and the same rated current I_{ref}=5 A, the EMUT C maximum current I_{max} is 100 A (I_{max}=45 A for EMUT A, I_{max}=40 A for EMUT B) and it is equipped with a static pulsed test output at 1000 impulses per unit of energy (imp/kWh). The three test outputs have been connected to a pulse reader, made of three signal conditioning circuits based on a photodetector (for EMUT A) and two pull-up resistors (one for EMUT B and one for the EMUT C), cascaded with logical ports acting as voltage regulators to obtain 0-5 V at the pulse reader output. After that, the three signals coming from the pulse reader output have been acquired through a NI9239 24-bit Data Acquisition board (DAQ) connected to a host PC running the test automation.

5.1.3.2 Experimental Tests

The tests proposed in this Sub-Section are aimed at evaluating the EMs behavior when the voltage and the current are not sinusoidal. It should be highlighted that they are not only distorted waveforms, but they are also distinguished by a realistic harmonic content for a LV distribution network, considering the limits defined in the standards [24], [25]. Three different tests were carried out, all of them are based on the setup sketched in Figure 25:

- sinusoidal waveform test (calibration measurement);
- fixed random harmonics test;
- random time-varying harmonics test.

In these three tests, detailed in the following, the calibrator generated a sinusoidal current and voltage at f_r=50 Hz. Only in the last two tests, an additional harmonic content up to the 25th harmonic has been superimposed to the 50 Hz components. The relative phase displacement between voltage and current has been set equal to zero for all the frequency components (pure resistive load), to focus only on the effect of the harmonic content on the active energy measurements performed by the EMs. Plus, this scenario is meaningful since the loads' power factor is very close to 1 in typical LV power networks. The current from the calibrator I_p has been stepped-up to I_s by a factor of 4 through the ICT and then fed to the EMUTs. The potential of the secondary winding of the ICT has been raised to U in order to obtain a phantom power supply for the EMUTs. The active energies E_{mA}, E_{mB} and E_{mC} measured by EMUT A, EMUT B and EMUT C, respectively, are compared against E_t, the energy measured by the reference power analyzer. The synchronization of the readings from the EMUTs and the power analyzer was implemented by starting the pulse counter acquisition in parallel with the energy computation performed by the power analyzer. The active energy readings were triggered when the electrical quantities provided by the calibrator are already in steady state. An in-depth analysis on the "pulse reader + DAQ" system properties has been already conducted in Paragraph 5.1.2.1.1.

5.1.3.2.1 Sinusoidal current and voltage – calibration measurement

The first test consisted in providing a sinusoidal current (I_p=5 A, rms) and a sinusoidal voltage (U=230 V, rms) by means of the Fluke 6105A to carry out the calibration of the EMUT C at nominal conditions and to check its measurement repeatability. Note that this operation had been already performed for EMUTs A and B in Sub-Section 5.1.2. The time duration of this calibration test is about 8 hours in order to replicate the same conditions under which EMUT A and B were subjected to. Note also that such a long-duration test makes negligible the contribution to uncertainty due to the test output reading compared to the overall energy measured by the EMUT. The chosen value for I_s is 20 A since it lays between I_{ref} and I_{max} for all the three

EMUTs and also because it is representative of a typical current intensity at the node where the EMs are installed in residential applications. This calibration procedure has been repeated for 8 times. For each repetition, the calibration coefficient $K_{EM\,C}$ was computed as:

$$K_{EM\,C} = \frac{E_{mC}}{E_t}\,, \tag{5.6}$$

where E_{mC} is the active energy reading from EMUT C and E_t is the corresponding reading of the reference instrument. Afterwards, the computations of the mean value $\overline{K}_{EM\,C}$ and of the standard deviation of the mean $\sigma_{K_{EM\,C}}$ have been carried out by evaluating the 8 values obtained by each test repetition. The coefficient $\overline{K}_{EM\,C}$ and the ones computed in Sub-Paragraph 5.1.2.3.1, $\overline{K}_{EM\,A}$ and $\overline{K}_{EM\,B}$, for EMUT A and B, respectively, have been then used to correct the E_m in all the following tests (see Sub-Paragraph 0 and 5.1.3.2.3). The correction is performed through:

$$E^*_{m\,i} = \frac{E_{m\,i}}{\overline{K}_{EM\,i}} \tag{5.7}$$

where: i = A, B and C; $E^*_{m\,i}$ is the EMUT i's corrected active energy reading. This procedure allows assessing the effect of the considered harmonic disturbances by means of the additional percentage error $e^*_i\%$:

$$e^*_i\% = \frac{E^*_{m\,i} - E_t}{E_t} \times 100. \tag{5.8}$$

The calibration coefficients $K_{EM\,i}$, where: i = A, B and C, refer the EMUTs' measurements to the reference energy meter's ones and they are obtained in presence of nominal conditions. As the off-nominal conditions are applied to the EMUTs, the possible deviations observed between the energy readings provided by the reference energy meter and the ones provided by the EMUTs (with the correction applied) can be attributed to the off-nominal conditions, because all the other quantities reasonably have not changed since the calibration measurement.

5.1.3.2.2 Fixed random harmonics

In the second test, two sets of current and voltage harmonics have been randomly generated complying with the limits prescribed by [24] for the voltage harmonics up to the 25th order in LV systems. Each voltage harmonic component is drafted from a uniform distribution which ranges from 0 to the corresponding limit presented in the EN 50160 standard. Since a pure resistive load is assumed, as mentioned above, the current harmonic relative amplitudes are analogous to the voltage ones and the overall rms value is set to I_p=5 A. The *THD* of the waveforms obtained according to the described procedure are 4.2 % and 6.4 %, which are realistic values for current and voltage distortion according to those highlighted in the standard [25]. The experiment

based on the test waveform with *THD* = 4.2 % will be addressed as ↯1, while the one based on the test waveform with *THD* = 6.4 % as ↯2. The magnitude spectra of the waveforms are represented in Figure 26 and are normalized to the 50 Hz component magnitude. The time duration of this test is about 8 hours. Finally, the effects of the fixed random harmonic are evaluated by applying (5.7) and (5.8).

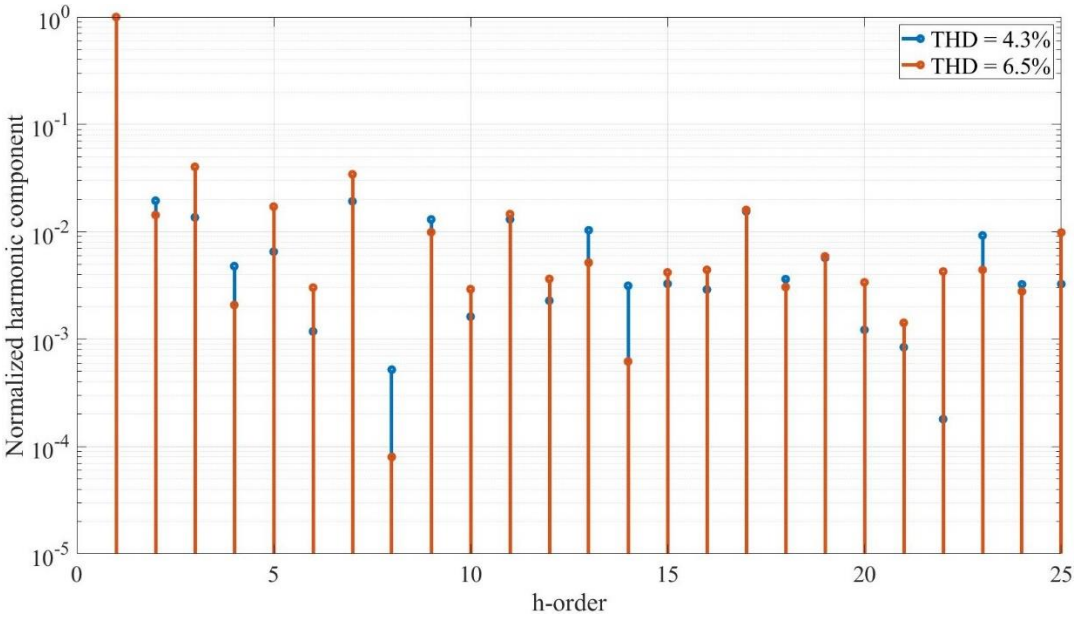

Figure 26 Normalized harmonic components randomly generated for the "Fixed random harmonics" tests ↯1 (*THD* = 4.2 %) and test ↯2 (*THD* = 6.4 %).

5.1.3.2.3 Random Time-Varying Harmonic Distortion

The third test's objective is to simulate a realistic scenario in which the energy meters are subjected to a harmonic distortion that changes unpredictably over time. To achieve this, a distorted voltage and current waveforms both generated with the same technique, illustrated in Sub-Paragraph 0, were applied for a short time interval (about 10 min). After that, another random waveform was applied, and so on for about 8.5 h. This operation was repeated 7 times. Finally, the effects of the random time-varying harmonic distortions are evaluated by applying (5.7) and (5.8).

5.1.3.3 Experimental Results

5.1.3.3.1 Sinusoidal current and voltage – calibration measurement

In Table 5.7 the data from the EMUT C calibration is reported, whereas the summary of the EMUTs' A and B results previously obtained in Sub-Paragraph 5.1.2.3.1 are listed in Table 5.8, for the sake of readability.

The percentage error $e_C\%$ has been computed according to (5.1) and $K_{EM\,C}$ according to (5.6). Note that, even for EMUT C, the standard deviation $\sigma_{K_{EM\,C}}$, associated to the computed average calibration coefficient, is very limited compared to the related average value $\overline{K}_{EM\,C}$ and consistent with the ones for EMUT A and EMUT B in Table 5.8. This result means that the EMUT A, EMUT B and EMUT C calibration measurements are distinguished by a good repeatability (all obtained standard deviations are at least 5000 times lower than the measured quantity). Finally, a check of the accuracy class has been conducted and, since the percentage error is about 0.70 %, the EMUT C has been proved to be widely compliant with the declared class (as for the EMUTs A and B).

Table 5.7 EMUT C calibration at nominal sinusoidal conditions.

	E_t [Wh]	E_{mC} [Wh]	$K_{EM\,C}$ [-]	$e_C\%$ [%]
	36416.0	36648	1.00637	0.64
	36419.5	36658	1.00655	0.65
	36420.8	36660	1.00657	0.66
	36423.7	36663	1.00657	0.66
	36407.3	36657	1.00686	0.69
	36404.6	36658	1.00696	0.70
	36406.7	36662	1.00701	0.70
	36406.9	36662	1.00701	0.70
$\overline{K}_{EM\,C}$			1.00674	
$\sigma_{K_{EM\,C}}$			$9\cdot10^{-5}$	

Table 5.8 EMUTs A and B calibration at nominal sinusoidal conditions, referenced from Table 5.3

	EMUT A	**EMUT B**
$\overline{K}_{EM}$	0.9983	1.00892
$\sigma_{K_{EM}}$	$2\cdot10^{-4}$	$4\cdot10^{-5}$

5.1.3.3.2 Fixed Random Harmonics

In Table 5.9 the readings and the additional percentage errors $e_i^*\%$ (i = A, B, and C) regarding the active energy measurements for the two fixed random harmonics tests are collected. The standard uncertainty $u_{e\,i\,\%}$ of each additional percentage error computed for this test is shown in the top row of Table 5.10.

Table 5.9 EMUTs additional percentage error at random distorted current and voltage condition

Set	***THD*** **[%]**	E_t **[Wh]**	$E_{m\,A}^*$ **[Wh]**	$E_{m\,B}^*$ **[Wh]**	$E_{m\,C}^*$ **[Wh]**	$e_A^*\%$ **[%]**	$e_B^*\%$ **[%]**	$e_C^*\%$ **[%]**
↯1	4.2	36529.1	36528.3	36474.8	36514.0	0.00	-0.15	-0.04
↯2	6.4	36532.2	36539.2	36474.8	36512.0	0.02	-0.16	-0.06

Table 5.10 Evaluation of Standard Uncertainty for the EMUTs additional percentage errors.

	Set	$u_{e\,A\,\%}$ **[%]**	$u_{e\,B\%}$ **[%]**	$u_{e\,C\,\%}$ **[%]**
Fixed random harmonics	↯1	0.09	0.09	0.09
	↯2			
Random time-varying harmonics	#1	0.2	0.2	0.2
	#2			
	#3			
	#4			
	#5			
	#6			
	#7			

Examining also the $e_i^*\%$ values (i=A, B, C) in Table 5.9, it can be noticed that: first, the magnitude of EMUT B's percentage error is greater than $u_{eB\%}$ by around 2 times; second, the values of $e_A^*\%$ and $e_C^*\%$ are of the same order of magnitude of (and even smaller than) $u_{eA\%}$ and $u_{eC\%}$. Given that, the analysis of the presented values is carried out according to the following considerations. Thanks to the average calibration coefficient $\overline{K}_{EM\,C}$ definition, it is possible to express the additional percentage error $e_i^*\%$ (i=A, B, C) by (5.8). $e_i^*\%$ is equal to zero (within the limits of the variation associated with $\overline{K}_{EM\,C}$) if $E^*_{m\,i}$ (i=A, B, C) is measured in conditions analogous to the ones of the calibration procedure. When the current and voltage distortion is introduced, the RMS quantities are the same as the ones related to the sinusoidal quantities used for the calibration. The reference energy meter is assumed to not present a significantly different behavior in the distorted conditions, given its wide bandwidth. Therefore, any value of the $e_i^*\%$ different from zero observed in distorted conditions

may be attributed to a performance downgrade of the EMs in these conditions. But first, the uncertainty associated to $e_i^*\%$ must be considered: if its confidence interval does not include zero, then it is reasonable to state that the EMs' behavior has been affected by the introduced distortion; otherwise, if the interval includes zero, the impact of the distortion is not observable, and nothing can be stated. Finally, the confidence interval has been computed as a double-sided interval centered in $e_i^*\%$ by means of the standard uncertainty. According to the analysis above, only EMUT B shows a slight influence due to the fixed random harmonic presence, given that the relative confidence intervals are [-0.24 %, -0.06 %] and [-0.25 %, -0.07 %].

5.1.3.3.3 Random Time-Varying Harmonic Distortion

In Table 5.11 are listed the observed maximum and minimum *THD* values of the generated current and voltage waveforms for each test sequence.

Table 5.11 THD range maximum and minimum values with random time-varying harmonic distorted current and voltage distortion.

Sequence	***THD* min [%]**	***THD* max [%]**
#1	3.5	6.9
#2	3.5	6.9
#3	3.8	7.0
#4	3.8	7.0
#5	3.2	6.9
#6	4.2	7.0
#7	3.7	7.5

For each sequence, the E^*_{mi} values, the reference energy readings E_t and the $e_i^*\%$ values are shown in Table 5.12, while the standard uncertainties $u_{ei\,\%}$ of the additional percentage errors $e_i^*\%$ are reported in bottom row of Table 5.10.

Table 5.12 . EMUTs additional percentage error with random time-varying harmonic distorted current and voltage distortion.

Sequence	E_t [Wh]	$E^*_{m\,A}$ [Wh]	$E^*_{m\,B}$ [Wh]	$E^*_{m\,C}$ [Wh]	$e^*_A\%$ [%]	$e^*_B\%$ [%]	$e^*_C\%$ [%]
#1	38075.1	38201.9	38060.6	38075.5	0.3	0.0	0.0
#2	38067.3	38194.0	38060.6	38078.5	0.3	0.0	0.0
#3	38059.4	38192.0	38060.6	38067.5	0.3	0.0	0.0
#4	38061.8	38177.2	38060.6	38082.4	0.3	0.0	0.1
#5	38053.8	38167.3	38060.6	38068.5	0.3	0.0	0.0
#6	38050.9	38160.4	38060.6	38072.5	0.3	0.0	0.0
#7	38051.4	38107.9	38060.6	38079.5	0.1	0.0	0.0

The random current and voltage distortion variations lead to percentage error variations that are not significative for EMUT B and C: as a matter of fact, the $u_{e\,i\,\%}$ values define confidence intervals including zero (see observations in Sub-Paragraph 5.1.3.3.2). On the contrary, EMUT A exhibits a [0.1 %, 0.5 %] confidence interval of $e_i^*\%$ for the sequences #1 to #6. Then, it can be concluded that the effect of the test scenario where the harmonic distortion of the current and the voltage waveforms randomly evolves over the time is not negligible for the EMUT A. Finally, observing Table 5.10, one could question the fact that the uncertainties relative to the percentage errors in the random time-varying harmonic test are higher than the ones in the fixed random harmonic test. This results from the test setup. To change the harmonic content of the voltage and current waveforms, the calibrator outputs must be set on standby, and the active energy cannot be measured during the transients between the standby and operational states because they would pollute the measurement. Therefore, considering that each harmonic configuration shall be applied for about 10 minutes, each repetition of the present test consists in performing about 50 different measurements and then to add the readings together. Hence, the uncertainty of the $e_i^*\%$ relative to the cumulative readings is higher than the uncertainty obtained in the fixed random harmonic cases. However, even if this uncertainty is twice the one in the fixed random harmonics case, it is still possible to observe whether the EMUTs' behavior is affected. Of course, the variation of the measured quantity must be evaluated against its confidence interval to judge the experimental result.

5.1.3.4 Conclusion

In this Sub-Section, three off-the-shelf energy meters have been tested by applying distorted current and voltage waveforms distinguished by realistic harmonic content. Their behavior has been assessed computing the index prescribed by the standards to verify whether distorted conditions affect the energy meters accuracy. From the results it is possible to conclude that (i) the adopted waveforms and the measurement setup implemented allow appreciating small variations in the energy meters accuracy; (ii) not all the energy meters are affected by distorted conditions. Therefore, considering the test waveforms prescribed by the standards and the results herein presented, it can be concluded that the Standards should improve in terms of incorporating more realistic test waveforms to better assess the energy meters behavior in realistic conditions.

5.2 ICT Metrological Characterization in presence of Current Distortion

In the recent years, the operation of ITs, both the inductive type and the low-power ones, has been affected by the huge revolution in the power network due to the growing installation of renewable energy sources and static power converters. The poor power quality leads to severe and unwanted consequences, both on the electrical and electronic assets, as well as on the end-users. In order to correctly and properly address such issues, the measuring instruments used for evaluating power quality need to operate accurately in a large frequency bandwidth. Often the primary sensing elements, such as the ITs, represent the weak spot in the measurements chain for such purposes, thus, they shall be verified and tested to provide accurate measurements in the power quality bandwidth. That is why a Standard dedicated to the use of ITs for power quality measurements has been developed: the IEC 61869-103 [98]. Moreover, users and manufacturers should be guided on how to test ITs to verify their correct operation and level of uncertainty, also, in such off-nominal operating conditions (a starting point for the tests is provided in [98]). Concerning ICTs operating under distorted waveform conditions, in literature several works can be found. For example, some testing procedures are described in [82], [99], [100], while error and non-linearity corrections have been studied and proposed in [101]–[104]. Finally, accuracy measurements and calibration procedures are discussed in detail in [105]–[107]. In light of the above, the present research uses the literature as a starting point to raise and to study empirically the issue of the impact of the harmonic distortion on MV ICTs and its consequences.

The first part of this research, presented in Sub-Section 5.2.1 and published in [108], explores how much the ICT accuracy is influenced by a set of currents with a realistic harmonic content, employing as tools the composite error index and a simplified version of it. The second part, presented in Sub-Section 5.2.2 and published in [109], starts from the results obtained in the first part and it ends with a practical metrological application for current distortion measurements.

5.2.1 ICT Accuracy Dependency on Current Distortion

The main aim of this first part of the research is to assess whether the actual distorted conditions of the network are really affecting the accuracy of ICTs. Moreover, a new procedure for this analysis is proposed, since the standards do not provide a uniform set of distorted waveforms to be applied and there is no agreement yet, among the experts, about how to evaluate the uncertainty of the instrument transformer when the operating conditions are different from the rated ones. In particular, a set of steady-state actual distorted waveforms have been collected from the grid, distinguished by different levels of harmonic distortion, and then applied to two typical off-the-shelf MV ICTs. Afterwards, the performance of the ICTs has been evaluated using the composite error index and its approximated version. Such a way to assess the ICT's accuracy is typical of, but not limited to, protective ITs. In literature many examples can be found: a virtual instrument has been

developed in [85]; in [110] a model has been studied to assess ITs affected by power quality issues; [111] and [112] instead, describe the use of ratio error applied to each harmonic component and the application of the frequency response approach, respectively. Finally, the application of the composite error on the evaluation of the ITs' performance in a variety of network conditions is studied in [113]–[115].

This Sub-Section is structured as follows: Paragraph 5.2.1.1 contains the complete description on how the actual steady-state distorted signals have been acquired. Paragraph 5.2.1.2 describes the simple measurement setup implemented to test the ICTs. The main tests performed are listed in Paragraph 5.2.1.3, while in Paragraph 5.2.1.4 the results and the postprocessing analysis are included. Finally, a brief conclusion with the key points is drawn in Paragraph 5.2.1.5.

5.2.1.1 Acquisition of Actual Signals

Two off-the-shelf ICTs have been tested using actual signals. Before describing the ICT testing (see Paragraph 5.2.1.3), it is necessary to describe how such signals have been acquired. First of all, the measurement instrument developed for the current collection is depicted in Figure 27.

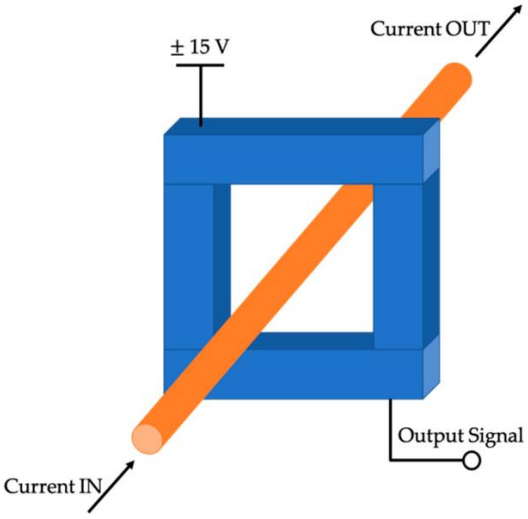

Figure 27 Measurement instrument developed for the acquisition of actual currents.

It simply consists of a Hall-effect-based current sensor, a direct current (DC) generator to supply it, and a data acquisition board (DAQ) to collect the samples. The current sensor is a LEM LA 100-P with a primary measuring range of 0–150 A; a secondary nominal current of 50 mA and an accuracy of ±0.45 %. As for the DAQ, an NI 9238 has been used. Its main characteristics are summarized in Table 5.13.

Table 5.13 Main features of the data acquisition board (DAQ) NI 9238.

Resolution	24 bit	Max Input Signal	± 500 mV
Sample Rate	50 kSa/s/ch	Simultaneous channels	yes
ADC	Delta-Sigma	Temperature range	- 40 to 70 °C
Gain Error	± 0.07 %	Offset Error	± 0.005 %

Since the DAQ supports only voltage inputs, and the LEM LA 100-P provides a current output, a resistor has been inserted as current sensor's load. Then, the voltage across the load has been acquired by means of the DAQ. The setup has been then used, inside the laboratory environment, to acquire currents flowing along the LV network when using different instrumentation; e.g. a thermostatic chamber, air conditioner, calibrator, power source, etc. According to the current sensor's specifications, the measurand expected magnitude and the DAQ's max input signal, a 100 Ω load resistance has been chosen. The acquired signals have been sorted in terms of *THD*, because the aim is to have signals with a variety of actual harmonic content, regardless the source of that content. Hence, values in Table 5.14 are listed from signals *A* to *E* for the sake of simplicity. The collected signals have all a *THD* < 10 %, which is a plausible and realistic distortion for the currents absorbed by users in LV and MV systems, according to IEEE Std. 519-2014 [25].

Table 5.14 List of the acquired signals and their total harmonic distortion (*THD*).

Signal	*THD* [%]
A	4.5
B	7.2
C	7.7
D	8.7
E	9.9

As an example, the waveform of signals *A* and *E* have been plotted and presented in Figure 28.

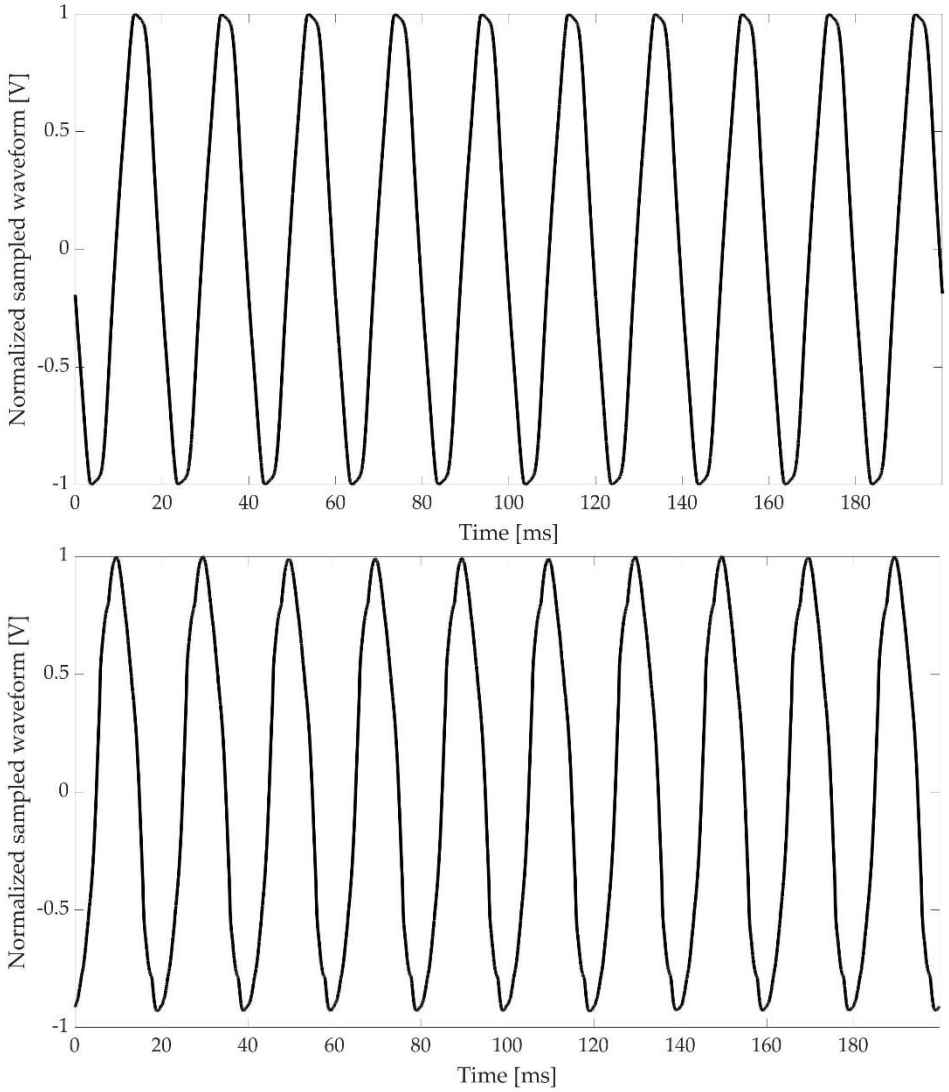

Figure 28 Waveform of the signal *A* (top) and *E* (bottom). The two sampled waveforms are normalized to 1.

5.2.1.2 Measurement Setup for ICT Testing

To inject the current, acquired as described in Paragraph 5.2.1.1, the following measurement setup has been improved and adopted. It consists of:

- A 14-bit Keysight Function/Arbitrary waveform generator 33220A. It features a frequency resolution of 1 µHz, a frequency accuracy of ± (20 ppm + 3 pHz), and a sampling frequency of 50 MSa/s. The function generator has been used to replicate the current waveform previously collected.
- Fluke Transconductance 52120A. Its task is to transduce the output voltage of the generator into a current consistent with the rated values of the transformers under test (TUTs). The main accuracy parameters of the transconductance are listed in Table 5.15.

Table 5.15 Main features of the two transconductance 52120A.

Current Range	% of output	% of range
2	0.015	0.070
5	0.015	0.060
10	0.015	0.020

- The MV TUTs. Their main characteristics are collected in Table 5.16.

Table 5.16 Main features of the two transformers under test (TUTs).

TUT	Ratio [A/A]	Rated Power [VA]	Accuracy Class	Extended Current Rating	
				[%]	[A]
T1	20/5	6	0.5	120	24
T2	100/5	6	0.2	120	120

- Two shunt resistors to measure both the primary and secondary currents of the TUTs. The first, S1, is a 1 mΩ resistor, and it is installed in series to the primary current; the second resistor, S2, has a 10 mΩ resistance, and it is installed in series to the secondary current and to a 220 mΩ/7 W resistive burden to guarantee the TUT's operation under rated conditions. As for their uncertainty, they feature 0.01 % and 0.005 % for S1 and S2, respectively. No other information is available from the manufacturer. Nevertheless, the characterization described in the next Paragraph has provided the information necessary for the TUTs' proper testing. Finally, in [82] the two shunts have been characterized vs frequency to assess whether they are affected from it or not. The results showed that the frequency does not affect both shunts, reporting variations lower than 2×10^{-6} Ω.
- An NI9238 DAQ to acquire the output voltages of both the shunts.

The conceptual scheme of the measurement setup is depicted in Figure 29.

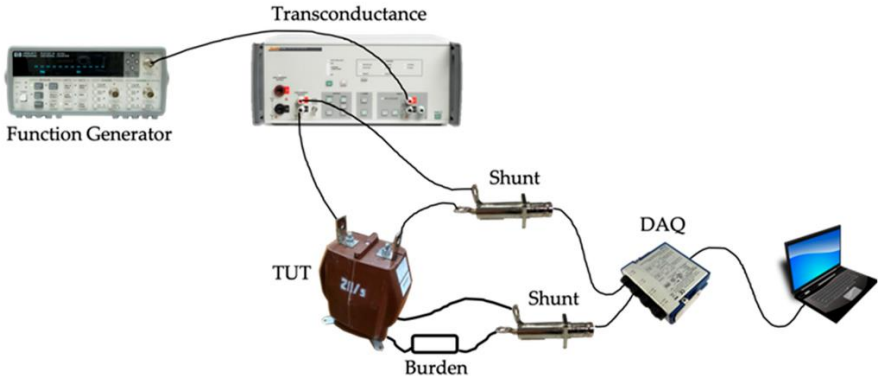

Figure 29 Schematic of the measurement setup used for the tests.

To summarize the operation of the setup, the signals listed in Table 5.14 have been reproduced with the function generator, transduced by the transconductance amplifier 52120A and then injected into the TUT.

5.2.1.3 Description of the Tests

The aim of the test is to acquire both primary and secondary currents of the TUTs. The currents are then used to perform an accuracy evaluation of the TUTs. First, the signals in Table 5.14 have been continuously fed from the function generator to the transconductance. Second, the output of the transconductance has been set to values of currents in accordance with [39]. In particular, [39] states that the ratio and phase errors, used to evaluate the accuracy class of the transformers, are evaluated at 5 %, 20 %, 100 % and 120 % of the transformer's rated primary current. Consequently, for the adopted TUTs, a set of RMS currents of 20, 4 and 1 A for T1 and of 100, 20 and 5 A for T2 have been generated by the transconductance and injected into the TUT. The 120 % current test has been omitted due to the limitations of the transconductance; however, over currents are not the aim of this research, which tackles the normal operation of the network in actual conditions.

To measure the currents, two shunts have been adopted together with a DAQ NI9238 in order to collect the output voltages. The whole measurement chain composed by the shunts and the DAQ has been characterized before and after the tests to ensure its repeatability and to confirm the shunt resistance values. The characterization process has been done by injecting the current of interest I (5 %, 20 % and 100 % of the primary and secondary currents) into the shunts by using a reference calibrator (Fluke 6105A), and then by reading the voltage measurements from the DAQ. One hundred measurements for each current level have been acquired, and the mean value R_m of the "shunts + DAQ" chain conversion factor has been computed, whose measurement unit is the ohm. The results of the characterization provided the estimate values of the equivalent resistances of the "shunts + DAQ" chain for each measured current. Such resistance values, used to compute the currents from the measured voltages, and their related extended uncertainty u_R (coverage factor k=2), are

listed in Table 5.17. The table includes the values of the first characterization, considering that the second characterization provided the same results.

Table 5.17 Results of the characterization of the "shunts + DAQ" measurement chain.

Shunt	I [A]	R_m [mΩ]	u_R [μΩ]
S1	1	0.999	1
	4	0.9995	0.4
	5	0.9994	0.3
	20	0.9994	0.1
	100	0.99941	0.07
S2	0.25	10.028	3
	1	10.029	1
	5	10.0291	0.6

As for u_R, it has been computed by means of the propagation of the uncertainties, as described in the Guide to the expression of Uncertainty in Measurement [47]:

$$u_R = \sqrt{\left(\frac{\partial R}{\partial V}\right)^2 u_{V_a}^2 + \left(\frac{\partial R}{\partial I}\right)^2 u_{I_b}^2} = \sqrt{\left(\frac{u_{V_a}^2}{I^2}\right) + \left(-\frac{V_m}{I^2}\right)^2 u_{I_b}^2}\,. \tag{5.9}$$

Where:

- V_m is the average measured voltage across the shunt;
- u_{V_a} is the uncertainty of the measured voltage evaluated with type A method, as the standard deviation of V_m;
- u_{I_b} is the uncertainty of the generated current evaluated with the type B method starting from the accuracy specification of the calibrator (with transconductance for the case of 100 A).

The type A method is based on the estimation of the expected value of the measurand and of its standard deviation, starting from *N* measurements. In the type B method instead, the contributions to the uncertainty are provided by the manufacturer of the devices in terms of indices. These are basically two: the error on the full scale and the one on the reading. There are few considerations regarding (5.9) to be pointed out: first, the measured voltage V_m and the generated current I are obviously uncorrelated quantities; second, the type B

evaluated uncertainty u_{V_b} does not appear in (5.9), since the whole "shunt + DAQ" measurement chain is the system to be characterized. In other words, the value of R_m already embodies the contribution due to the DAQ's error in every considered current scenario. This operation was possible because of the fact that exactly the same setup has been implemented both in the characterization and in the measurement procedures. Afterwards, for each signal of Table 5.14, 100 measurements of 10 periods of the above-mentioned set of currents have been collected for both the primary and the secondary by acquiring the voltage drop on the shunts S1 and S2 (sampling frequency 50 kSa/s). To complete the set of tests, and to better evaluate the results, the two TUTs have been fed with sinusoidal signals. In particular, the three currents of interest (100, 20, 5 A and 20, 4, 1 A) have been injected as 50 Hz sinusoidal waveforms. Again, 100 measurements of both primary and secondary currents have been collected. This last test has been considered fundamental to assess the performance of the ICTs at rated conditions; hence, to use the results as a comparison with the other operating conditions.

5.2.1.4 Experimental Results

The evaluation of the TUTs accuracy has been carried out by means of the ratio error ε, the phase error $\Delta\varphi$, and the composite error ε_c, defined in [39]. The indices ε and $\Delta\varphi$ are used to assess the performance of the ICTs at sinusoidal conditions, whilst ε_c is introduced after the encouraging results obtained in [82]. In fact, ε_c was used in [82] to assess the ICT's behavior in the presence of fault-derived signals; instead here, ε_c is applied to the evaluate ICTs in presence of steady-state distorted signals. For convenience, the formula of ε_c is reported:

$$\varepsilon_c \triangleq \frac{\sqrt{\frac{1}{T}\int_0^T \left(k_r i_s - i_p\right)^2 dt}}{I_p} \times 100\,. \tag{5.10}$$

Where:

- k_r is the rated transformation ratio
- i_p is the instantaneous value of the primary current;
- i_s is the instantaneous value of the secondary current;
- I_p is the RMS of the primary current;
- T is the duration of one cycle.

If i_p and i_s are sinusoidal waveforms, then the approximated composite error ε_c^* calculated with (see [115]):

$$\varepsilon_c^* \approx \sqrt{\varepsilon^2 + \Delta\varphi^2}\,. \tag{5.11}$$

Attention shall be paid to the usage of ε and $\Delta\varphi$: these two parameters are defined for the instrument transformers only in the presence of sinusoidal quantities. When actual distorted waveforms are considered, as done below, ε and $\Delta\varphi$ are computed for the 50 Hz components. This is a non-conventional procedure, according to the ε and $\Delta\varphi$ definitions, even if commonly adopted. In Table 5.18 and Table 5.19 the results are reported for T1 and T2, respectively. The following quantities are shown: ε and $\Delta\varphi$ for the 50 Hz harmonic component; ε_c computed by the numerical implementation of (5.10) and ε_c^*. Each quantity is averaged over the 100 repeated measurements conducted for each signal of Table 5.14 at 5 %, 20 % and 100 % of the rated primary current I_{pr}.

Table 5.18 Results for T1. Averages of ε, $\Delta\varphi$, ε_c, ε_c^* for the sinusoidal case and all the distorted signals, at 0.05 I_{pr}, 0.2 I_{pr} and I_{pr}.

I_p [A]	Signal	ε [%]	$\Delta\varphi$ [mrad]	ε_c [%]	ε_c^* [%]
1	Sinusoidal	−0.7865	19.53	2.148	2.105
	A	−0.8117	19.49	2.156	2.111
	B	−0.8172	19.81	2.181	2.143
	C	−0.7534	19.42	2.120	2.083
	D	−0.8070	19.47	2.150	2.107
	E	−0.8000	19.38	2.142	2.097
4	Sinusoidal	−0.4752	12.497	1.3398	1.3370
	A	−0.4983	12.460	1.3448	1.3419
	B	−0.5216	12.568	1.3605	1.3607
	C	−0.4667	12.383	1.3239	1.3233
	D	−0.5195	12.324	1.3395	1.3374
	E	−0.4768	12.445	1.3345	1.3327
20	Sinusoidal	−0.2778	7.580	0.8086	0.8073
	A	−0.2966	7.577	0.8181	0.8137
	B	−0.3090	7.598	0.8239	0.8202
	C	−0.2820	7.584	0.8123	0.8092
	D	−0.3027	7.636	0.8274	0.8214
	E	−0.2830	7.592	0.8146	0.8102

Table 5.19 Results for T1. Averages of ε, $\Delta\varphi$, ε_c, ε_c^* for the sinusoidal case and all the distorted signals, at 0.05 I_{pr}, 0.2 I_{pr} and I_{pr}.

I_p [A]	Signal	ε [%]	$\Delta\varphi$ [mrad]	ε_c [%]	ε_c^* [%]
5	Sinusoidal	−0.176	6.04	0.649	0.629
	A	−0.173	5.73	0.617	0.598
	B	−0.192	5.81	0.630	0.612
	C	−0.190	5.77	0.629	0.608
	D	−0.234	5.96	0.659	0.640
	E	−0.219	6.11	0.667	0.649
20	Sinusoidal	−0.0331	3.877	0.391	0.3891
	A	−0.0876	3.639	0.376	0.3743
	B	−0.0937	3.633	0.391	0.3752
	C	−0.0838	3.632	0.381	0.3727
	D	−0.0936	3.636	0.380	0.3754
	E	−0.1040	3.605	0.383	0.3752
100	Sinusoidal	0.0541	2.4116	0.24734	0.24714
	A	−0.0206	2.2879	0.23080	0.22973
	B	0.0292	2.2702	0.22947	0.22889
	C	0.0378	2.2468	0.22811	0.22784
	D	−0.0130	2.2804	0.22875	0.22842
	E	−0.0330	2.2995	0.23260	0.23231

From the graphical representation of Table 5.19 in Figure 30, it emerges that ε_c^* slightly underestimates ε_c for T2. It is also evident that the composite error decreases as the current gets closer to the rated one, which is an expected behavior, and that the composite error variation among the different distortion cases is almost absent. As for T1, the same observations can be drawn from Table 5.18, and consequently, their graphical representation is omitted.

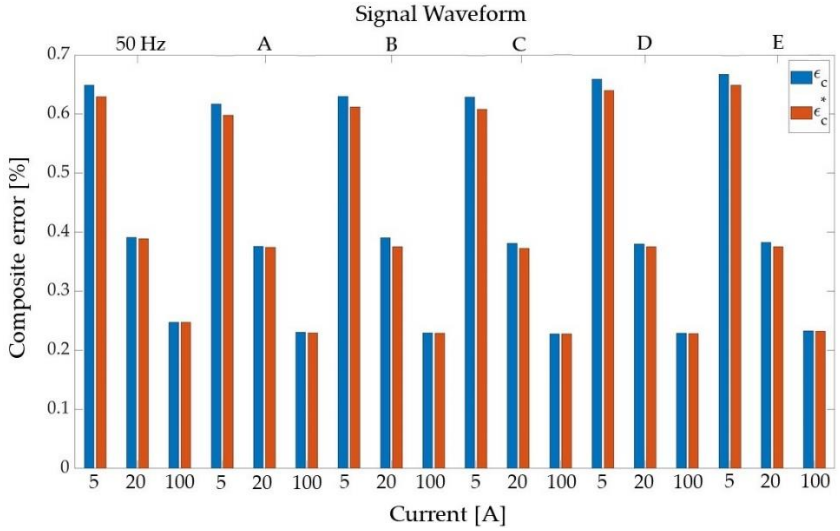

Figure 30 Graphical representation of the results in Table 5.19.

For convenience, the maximum standard deviations of the averages of ε, $\Delta\varphi$, ε_c and ε_c^*, for every current case, is reported in Table 5.20. The standard deviation of each parameter for both the TUTs gets smaller as the primary current gets closer to the rated one. The composite error and the ratio error are defined as dimensionless percentage quantities; thus, their standard deviation shall be expressed accordingly as percentages. The uncertainty of the parameters in the Table, evaluated with the type B method, has been omitted, because, for the comparison of the signals from *A* to *E*, in each current category, the measurement chain involved is the same. Therefore, for the evaluation of the parameters' variation, the uncertainty evaluated with type B method is not significative.

Table 5.20 σ_ε, $\sigma_{\Delta\varphi}$ and $\sigma_{\varepsilon_c^*}$ are maximum standard deviations of the averages of ε, $\Delta\varphi$, ε_c, ε_c^*, respectively, for both the TUTs at 0.05 I_{pr}, 0.2 I_{pr} and I_{pr}.

TUT	I [A]	σ_ε [%]	$\sigma_{\Delta\varphi}$ [mrad]	σ_{ε_c} [%]	$\sigma_{\varepsilon_c^*}$ [%]
T1	1	0.0009	0.01	0.002	0.001
	4	0.0003	0.003	0.0005	0.0003
	20	0.0003	0.002	0.0003	0.0002
T2	5	0.002	0.01	0.002	0.001
	20	0.0004	0.004	0.003	0.0004
	100	0.0002	0.0006	0.00009	0.00007

In Table 5.18 and Table 5.19, note that both T1 and T2 are compliant with their rated accuracy class (0.5 and 0.2, respectively): the measured ratio and phase errors in the sinusoidal case are smaller than the limits prescribed in [39]. The limits for the accuracy classes 0.2 and 0.5 are reported in Table 5.21, showing the maximum admitted ratio error ε_{max} and the phase error $\Delta\varphi_{max}$. Since these limits are defined for sinusoidal waveforms, then it is possible to extend Table 5.21 by applying (5.11) in order to estimate the corresponding composite error limits $\varepsilon_{c\,max}^*$ for each accuracy class. These values have been computed and listed in the last three columns of Table 5.21.

Table 5.21 ε and $\Delta\varphi$, limits for the 0.2 and 0.5 accuracy classes transformers defined in [39]. The table has been extended with $\varepsilon_{c\,max}^*$, obtained from the limits ε_{max} and $\Delta\varphi_{max}$.

Accuracy Class	ε_{max} [%]			$\Delta\varphi_{max}$ [mrad]			$\varepsilon_{c\,max}^*$ [%]		
	0.05 I_{pr}	0.20 I_{pr}	I_{pr}	0.05 I_{pr}	0.20 I_{pr}	I_{pr}	0.05 I_{pr}	0.20 I_{pr}	I_{pr}
0.2	0.75	0.35	0.2	9	4.5	3	1.17	0.57	0.36
0.5	1.5	0.75	0.5	27	13.5	9	3.09	1.54	1.03

At this point, it is interesting to compare the numerically computed values of ε_c with the corresponding value of $\varepsilon_{c\,max}^*$, since it could be a criterion to assess the TUTs accuracy performance in the steady-state distorted conditions. The composite error physical meaning is how well the instrument transformer output matches the measurand, and $\varepsilon_{c\,max}^*$ is the estimate of the worst tolerated scenario in sinusoidal conditions.

Therefore, if ε_c in the distorted cases is smaller than $\varepsilon_{c\,max}^*$, then the TUT accuracy could be considered acceptable. The results in Table 5.18 and Table 5.19 show that both TUTs present a composite error ε_c smaller than the limit value $\varepsilon_{c\,max}^*$ in all of the distorted cases. Additional tests were carried out to support the results herein obtained: the first, at very high THD (25.0 %) with random frequency components up to the 20th harmonic order; the second, at THD = 10 %, but with a single frequency component which was changed from the 20th (1000 Hz) to the 100th (5000 Hz) harmonic order. Under these conditions the TUTs have maintained their accuracy class, showing consistency with the results obtained in Table 5.18 and Table 5.19. As a further comment, the instrument current transformer performance evaluated by means of the composite error suggests that its accuracy is mainly dependent upon the performance at 50 Hz and only (very) slightly affected by the actual harmonic content of the measurand. It is worth highlighting that all the above-mentioned results prove the applicability of (5.11) for two main reasons. First, the set of currents used has an actual harmonic content consistent with the Standards. Second, the peculiarity of using only the 50 Hz component is supported by the fact that common measurement instruments (e.g. phasor measurement units, energy meters, etc.) already extract such a component. To validate the obtained results, the measurements have been repeated after more than a month to ensure also their repeatability. The new set of results completely confirms what was already presented in this investigation. As a final and main comment, it is interesting to assess the obtained results from a practical point of view. Such results allow to state that ICTs maintain their class performance even in presence of realistic distortions/off-nominal conditions of the network up to a 25 % of THD. Furthermore, the use of ε_c^* and ε_c for measuring IT is supported by the results and by the fact that, at off-nominal conditions, they provide a more significant information compared to the ratio and phase errors.

5.2.1.5 Conclusions

The aim of this first part of the research is to raise the issue of whether or not realistic power network conditions affect the accuracy performance of inductive current transformers. This has been done considering that no standard defines how to proceed with such tests, which waveforms have to be injected, and how much they are affected. Therefore, actual distorted currents have been collected from the grid and injected to two off-the-shelf current transformers. Afterwards the results have been evaluated in terms of the composite error and an approximated version of it. From the results it emerges that both transformers show really good behavior at rated and at off-nominal conditions. Hence, in this particular case study, which involves devices adopted by several utilities, it is reasonable to ask whether the influence of distorted signals (with values within the limits suggested by IEEE Std 519-2014) is really affecting the behavior of the transformers. The answer to that question, from the presented results, is no. In other words, in practical cases, hence, when the transformer is operating at actual conditions, their behavior is only slightly affected by the distorted input signals. Such a

conclusion is not to be claimed as obvious, because the common idea is that ICTs operation is quite affected by distorted primary currents. As a consequence, several works in literature deal with how to solve such an issue despite is minor significance in realistic conditions (even if the proposed solutions are typically effective). A secondary conclusion is that, in light of the previous one, the application of the composite error should be encouraged for the assessment of the transformers' accuracy when they operate at off-nominal conditions. As a matter of fact, it provides a more exhaustive information on the accuracy of the transformer, compared to the one of ratio and phase errors. Overall, the standards should include more details for the users regarding how to test the instrument transformers in more realistic conditions, emphasizing on the influence quantities affecting most the accuracy of the transformers.

5.2.2 Practical Estimation of the Total Harmonic Current Distortion Uncertainty

The Total Harmonic Distortion (THD) measurement is among the key elements to assess the power quality of a network. However, the Standards does not provide sufficient information to evaluate the uncertainty related to the THD, neither voltage nor current one. Therefore, this part of the research on the ICTs tackles the practical uncertainty estimation of the current THD measured by two off-the-shelf MV ICTs employing a closed-form expressions developed in [116]. This is performed by comparing actual THD measurements with the estimates obtained from the closed-form expressions. What follows has been structured as: Paragraph 5.2.2.1 briefly describes the closed-form expressions. The main setup used to collect the THD measurements is shown in Paragraph 5.2.2.2. Paragraph 5.2.2.3 deals with the tests and the results, while Paragraph 5.2.2.4 includes the final remarks and comments.

5.2.2.1 The Closed-form Expressions

Starting from the definitions of THD and of the ratio error affecting the rms of the harmonic components X_i of the measured signal, the following expression is obtained:

$$THD = \sqrt{\sum_{i=2}^{N} \left(\frac{X_i(1+\varepsilon_i)}{X_1(1+\varepsilon_1)} \right)^2} . \tag{5.12}$$

In (5.12) the values of the ratio error of the 50 Hz component ε_1 and of the harmonic components ε_i have been taken from the standards [36], [117]. Afterwards, (5.12) can been manipulated and treated like a non-linear combination of uniformly-distributed random variables. The resulting probability density function is described by the expected value μ_{THD} and the variance σ^2_{THD}. Both these parameters have been derived:

$$\mu_{THD} = \mathrm{P}\left(m, \frac{1}{2}\right) * \sqrt{\frac{\Omega}{m}}\ , \tag{5.13}$$

$$\sigma^2_{THD} = \Omega\left\{1 - \frac{1}{m}\left[P\left(m, \frac{1}{2}\right)\right]^2\right\}, \tag{5.14}$$

where P is the Pochhammer function, while m and Ω are two parameters that only depend on the accuracy class of the ITs involved. The reader can refer to [116] for further information.

5.2.2.2 The Measurement Setup

The same measurement setup shown in Paragraph 5.2.1.2 has been employed to acquire the primary and secondary currents of the two off-the-shelf ICTs. The acquired signals have been used to compute the THD associated to the primary current. This setup, recalled in Figure 31, consists of:

- An arbitrary waveform generator (Agilent 33220A) (AWG) which provided the desired waveforms (actual waveforms collected from the grid).
- A Fluke transconductance amplifier 52120A to amplify and convert the waveform generator's output into a current suitable for the ICT under test.
- The two MV ICTs under test (T_1 and T_2). Both features a rated power of 6 VA. T_1 has a ratio of 20/5, while T_2 100/5. Finally, their accuracy classes are 0.5 and 0.2 for T_1 and T_2, respectively.
- Two shunt resistors, S_1 for the primary current is a 1 mΩ resistor; S_2 for the secondary current is a 10 mΩ resistor. The two shunts feature an uncertainty of 0.01 % and 0.005 %, for S_1 and S_2, respectively.
- A NI9238 Data acquisition board (DAQ) to acquire the voltages at the shunt terminals [118].

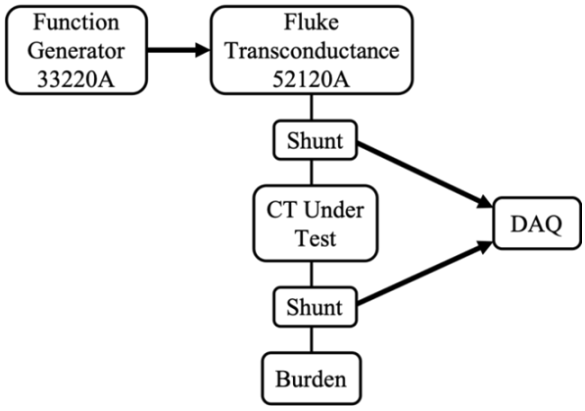

Figure 31 Simple schematic of the measurement setup.

In brief, a set of signals with different THD – as detailed in the following Paragraph – have been reproduced with the waveform generator and transduced into the ICTs under tests. With the shunts + DAQ, the primary and secondary currents have been collected before being further elaborated.

5.2.2.3 Tests & Results

This Paragraph is composed of three Sub-Paragraph: the first is dedicated to the description of the performed tests; the second one is dedicated to the uncertainty evaluation of the acquired quantities; in the last one the obtained results are shown and discussed.

5.2.2.3.1 Tests description

The main idea is to compare the expected value and the variance of THD measured by the two ICTs under test (μ_{THD_CT} and $\sigma^2_{THD\_CT}$) with those estimated with the closed-form expressions (μ_{THD_e} and $\sigma^2_{THD\_e}$). To this purpose, the measurement datasets obtained during the research conducted in Sub-Section 5.2.1 have been employed: five different waveforms, distinguished by ascending THD value, have been acquired in the laboratory environment and loaded into the AWG. Then, the transconductance amplifier, operated with the AWG's output signal, fed the ICTs under test. The primary and secondary currents have been acquired by means of series shunt resistors + DAQ. The waveforms are recalled also here for the sake of readability in Table 5.22.

Table 5.22 List of the acquired signals and their total harmonic distortion (*THD*).

Signal	*THD* [%]
A	4.5
B	7.2
C	7.7
D	8.7
E	9.9

Before moving to assess the quality of the estimated THD uncertainty, there are some considerations that must be done. The first one addresses the distorted primary current waveforms. Their rms is equal to the rated primary current value for each ICT. Then, the harmonic distortion is randomly drawn, yet compliant with the Standard EN 50160. This means that the number of the harmonics involved is limited to the 25th order and their amplitudes relative to the 50 Hz-component are capped according to the values defined by the standard. Turning to the closed form expression, which has to be evaluated in this experimental case study, it requires

just: (i) the accuracy class of T_1 and T_2 and (ii) the rms values of the harmonic components included in the current waveform. Concerning (i), the accuracy class information is readily available on the ICTs' nameplate and it is reported in Paragraph 5.2.2.2 (0.5 for T_1 and 0.2 for T_2). From the accuracy class, the ratio errors at 50 Hz and at the higher harmonic frequencies are completely known from the standards family EN 61869. Concerning (ii), the information is operatively obtained through the processing of the signal coming from the ICT's primary winding. This has been done in order to experimentally validate the THD uncertainty estimation closed-form expressions. Of course, if a practical application is considered, the information (ii) is extracted necessarily from the transduced secondary current. This implies that the THD value of the secondary current must be the same as the one of the current at the primary side, i.e. the ICT must behave as a linear system in the considered frequency range. The results obtained in Sub-Section 5.2.1 support this hypothesis, however, additional tests have been carried out to deepen this analysis. The goal is to verify the repeatability of the ICTs' almost linear behavior among the experimental observations. The Agilent 33220A has been replaced with Fluke Calibrator 6105A: this solution enabled the ICTs' primary winding to be supplied with a random accurate distorted current waveform characterized by a THD = 9.0 %. Consequently, 100 repetitions have been performed. The results have shown that the average THD measured at the primary and the secondary windings of both the ICTs are equal to 9.0 % and the standard deviations are 0.001 % for T_1 and 0.0003 % for T_2. Thus, it is possible to state that (i) the ICTs do not add significant distortion to the secondary current, (ii) the behavior is repeatable, (iii) (2) and (3) can be meaningfully applied on the signal measured at the secondary winding for practical applications.

5.2.2.3.2 Uncertainty evaluation

To validate the quality of the closed-form expressions, a direct comparison with experimental THD uncertainty is needed. The method employed for the evaluation of the uncertainty is the Monte Carlo method described in the GUM and recalled in Paragraph 3.2.1.2. The generated probability distribution function of each primary current harmonic component is a uniform distribution. The mean value is equal to the harmonic component magnitude, whereas the standard deviation is dependent on the gain and offset errors of the transconductance amplifier operated with the AWG. These two errors are shown in Table 5.23 (for the 20 A range) and Table 5.24 (for the 120 A range). No other sources of uncertainty are involved in the MC computation; in fact, aside from the current input, the implementation of (5.12) requires only the ratio error information.

Table 5.23 Fluke Transconductance's gain and offset errors given with 99 % confidence interval for the 20 A range.

Frequency range [Hz]	% of output [%]	% of range [%]
10 ÷ 65	0.015	0.060
65 ÷ 300	0.030	0.060
300 ÷ 1000	0.100	0.060
1000 ÷ 3000	0.300	0.200

Table 5.24 Fluke Transconductance's gain and offset errors given with 99 % confidence interval for the 120 A range.

Frequency range [Hz]	% of output [%]	% of range [%]
10 ÷ 65	0.015	0.020
65 ÷ 300	0.030	0.030
300 ÷ 1000	0.100	0.100
1000 ÷ 3000	0.300	0.250

The 25 uniform distributions have been propagated through the THD formula in order to obtain the THD probability distribution. The Monte Carlo method has been implemented with 10^6 repetitions and the resulting distributions for the case with Signal D are shown in Figure 32 and Figure 33 for T_1 and T_2, respectively. The distributions obtained for the other cases do not differ significantly and so they are not reported. At this point, the standard deviation and the confidence intervals can be easily computed.

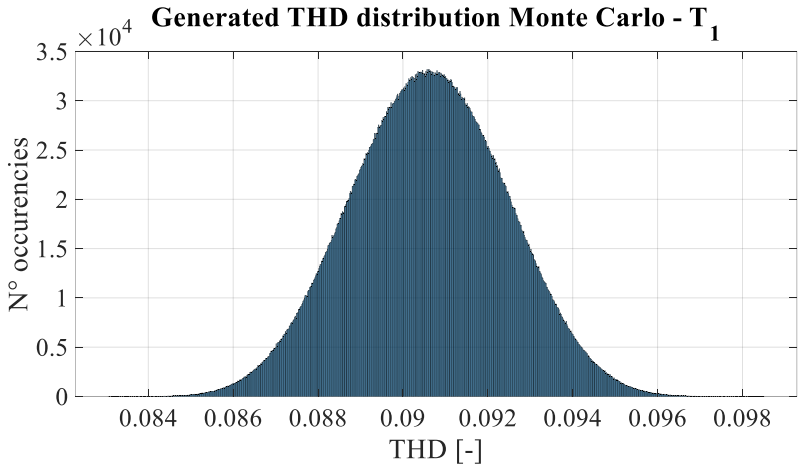

Figure 32 THD distribution of the T_1 primary current generated via Monte Carlo method in the case of Signal D.

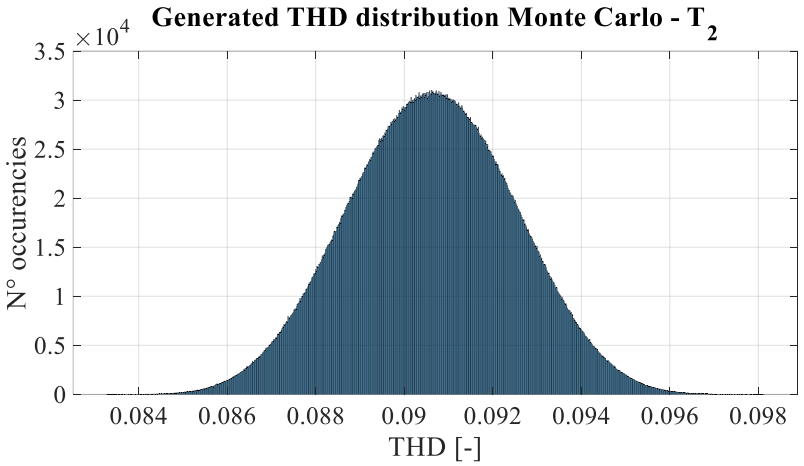

Figure 33 THD distribution of the T_2 primary current generated via Monte Carlo method in the case of Signal D.

5.2.2.3.3 Discussion of results

Now that the simulations run by implementing the MC are performed, the measured THD and its variance can be measured with those obtained by using (5.13) and (5.14). Therefore, Table 5.25 and Table 5.26 list, for both measured and estimate quantities, the mean, standard deviation and standard confidence interval (coverage factor $k = 1$) for T_1 and T_2, respectively.

Table 5.25 Mean, standard deviation and confidence interval upper and lower limits (IC max and IC min, respectively) of the primary current THD for T_1.

Signal	Technique	Mean [%]	Standard deviation [%]	IC min [%]	IC max [%]
A	Estimate	4.43	0.09	4.34	4.51
	MC	4.44	0.03	4.40	4.47
B	Estimate	6.9	0.1	6.8	7.1
	MC	6.93	0.03	6.90	6.97
C	Estimate	7.6	0.1	7.5	7.8
	MC	7.63	0.03	7.59	7.66
D	Estimate	8.7	0.2	8.5	8.9
	MC	8.71	0.04	8.67	8.75
E	Estimate	9.8	0.2	9.7	10.0
	MC	9.85	0.04	9.81	9.88

Table 5.26 Mean, standard deviation and confidence interval upper and lower limits (IC max and IC min, respectively) of the primary current THD for T_2.

Signal	Technique	Mean [%]	Standard deviation [%]	IC min [%]	IC max [%]
A	Estimate	4.40	0.03	4.36	4.43
	MC	4.43	0.03	4.40	4.46
B	Estimate	6.94	0.05	6.89	6.98
	MC	6.95	0.03	6.92	6.98
C	Estimate	7.65	0.06	7.59	7.71
	MC	7.66	0.03	7.63	7.69
D	Estimate	8.71	0.07	8.65	8.78
	MC	8.73	0.03	8.69	8.76
E	Estimate	9.84	0.07	9.76	9.91
	MC	9.85	0.03	9.82	9.88

In Figure 34 and Figure 35, the THD confidence intervals defined by the limits in Table 5.25 and Table 5.26 are depicted just for the case with Signal D, as an example of graphical comparison between the two methods.

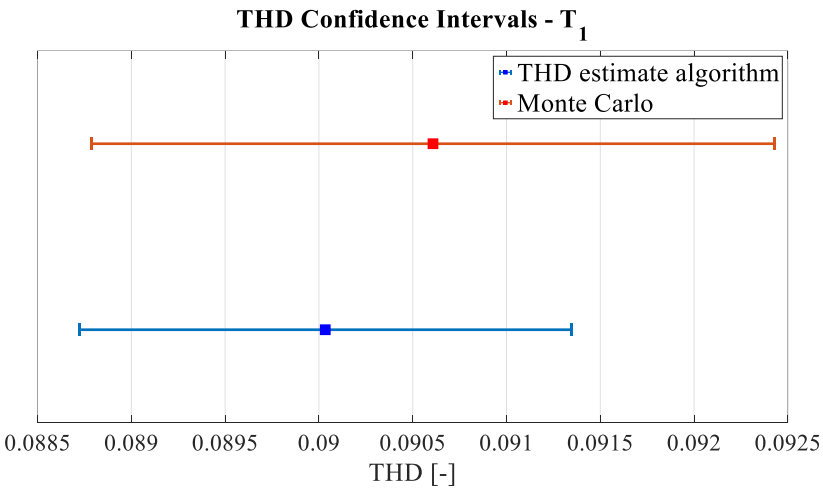

Figure 34 Comparison between the T_1 primary current THD estimate obtained with the proposed algorithm (blue interval) and the THD evaluation through the Monte Carlo method in the case of Signal D.

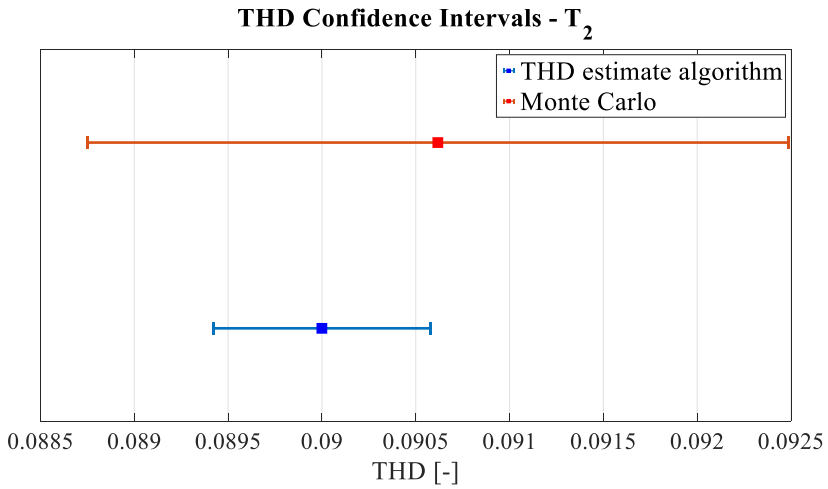

Figure 35 Comparison between the T_2 primary current THD estimate obtained with the proposed algorithm (blue interval) and the THD evaluation through the Monte Carlo method in the case of Signal D.

From the Figures 34, 35 and the Tables 5.25, 5.26, it is possible to confirm the effectiveness of the closed-form expressions. As a matter of fact, the confidence intervals obtained from the Monte Carlo method and the THD estimate algorithm are coherent between each other for both the ICTs under test (with different accuracy class and rated current) and for the different distorted signals. Due to the stochastic nature of the confidence intervals, even the case in which the two confidence intervals are slightly or partially not superimposable because of different lengths or the presence of a relative shift, the test would be still considered as passed and the expressions proved. Finally, it is possible to conclude that the closed-form expressions are a valid tool that can be employed in practical contexts by distribution system operators.

5.2.2.4 Conclusion

This Sub-Section tackles the evaluation of the uncertainty associated to the THD measurements. In particular, the validation of a practical expression has been tested on a real use case involving current transformers currently adopted for the THD measurements in MV networks. After evaluating the uncertainty associated with the THD measurements by using the Monte Carlo approach, it has been compared with those obtained from the referenced closed-form expressions. The obtained results clearly confirm the applicability of this technique and its effectiveness in terms of determining the uncertainty associated to the THD. Therefore, this new developed tool could be of great help for DSOs and utilities to provide uncertainty information along with the THD measurements performed in-field.

5.3 Metrological Characterization of a Virtual PMU

The study and monitoring of the modern power networks are very complex due to the many technological aspects linked to the development of the Smart Grid concept. Nevertheless, the recent introduction of the real-time simulators (RTSs) in power systems application has been a groundbreaking innovation. Thanks to the RTSs, researchers and system operators can simulate elaborate power networks, with their components, in a realistic way and make them interact with real-world components too. The goal is better understanding and predicting the operation of the overall system and its parts, often in critical and off-nominal conditions. The RTSs enables Hardware-in-the-Loop (HIL) and Digital Twin (DT) applications. The former technique consists of exploiting the analog/digital input/outputs of the RTS to interface real devices with the simulated system, which can be beneficial for validating and testing both the real device and the simulated system model. As for the DT, instead, it consists of a such detailed model that can be considered as the virtual copy of a real system and, thus, it can be used to predict the behavior of its real-world counterpart. Such techniques allow for the creation of an infinite number of scenarios. For example, monitoring a grid section under operation together with its DT, could highlight anomalies in the real network and consequently enable the system operator to avoid faults and take corrective actions. Hence, it is important that the simulated network elements and devices (cables, generation, accessories, converters, etc.) are correctly modeled and characterized. This is particularly true if the RTS data acquisition capabilities are used. Here is where the metrological approach of the present research, published in [119], gives its contribution: emphasizing the role of a preliminary characterization of the RTS and the virtual model of a physical device, a PMU, to avoid unexpected sources of uncertainty. The literature already includes several works on virtual PMUs and RTS applications. For example, [120] described a PMU-RTS HIL test bed that aims at characterizing physical PMUs. In [121]–[123], virtual PMUs have been developed and implemented within HIL and DT contexts. Complete DT infrastructure consisting of physical PMUs and RTS-based simulation systems has been described in [124]–[126]. Finally, the impact of time delays in HIL application is studied in [127]. However, the added value of this research work consists of the specific analysis of the contribution to the uncertainty of the RTS system and, in particular, of its virtual elements, which are often neglected. To do this, first, the characterization of a PMU calibrator, aimed at assessing the performance of the RTS and the virtual device, has been described in detail.

This Section is organized as follows. Sub-Section 5.3.1 introduces the developed PMU calibrator and it describes its entire characterization process. The adopted RTS is presented in Sub-Section 5.3.2 together with the virtual PMU. Sub-Section 5.3.3 contains the characterization of the virtual PMU and the uncertainty propagation process aimed at quantifying the characterization accuracy. Finally, the conclusions are given in Sub-Section 5.3.4.

5.3.1 Characterization of the Calibrator

The first operation to be accomplished is the characterization of the calibrator, which is presented herein. The final goal is to assess the uncertainty that can be reasonably associated with the reference test waveform generated by the calibrator. Once this operation has been performed, the virtual PMU performance can finally be evaluated. This study deals only with the steady-state characterization for the M-class PMU, which are in general more stringent than the P-class PMU requirements as far as the TVE, the FE and the RFE are concerned. However, the dynamic performances are outside the present study's scope. The virtual PMU has a reporting rate of 1 frame per second (fps), which is foreseen and tolerated by the standard IEC 60255-118-1 [43]; consequently, the dynamic performance requirements and the out-of-band requirements do not apply. The remainder of this Sub-Section contains: first, the calibrator concept and hardware are presented in Paragraph 5.3.1.1; second, the designed characterization tests for the calibrator are described in Paragraph 5.3.1.2; finally, the characterization results are commented on and arranged to provide the accuracy specifications of the calibrator in Paragraph 5.3.1.3.

5.3.1.1 The Calibrator Hardware Architecture

The standard IEC 60255-118-1 prescribes the verification of some parameters that quantify the deviation of the synchrophasor measured by the tested PMU from the reference one. These parameters are the Total Vector Error (TVE), the Frequency Error (FE), and the Rate Of Change Of Frequency (ROCOF) Error (RFE). The uncertainty affecting the reference synchrophasor should be at least one order of magnitude smaller than the one expected from the tested PMU. To conduct this kind of evaluation, a PMU test system (or PMU calibrator) is needed. In recent years, many have faced the problem of PMU calibration. Besides the research on the definition of accurate phasor estimation algorithms [128]–[131], the implementation of reference class hardware test systems is of key importance to the successful deployment of PMUs in Smart Grids. Researchers and national metrological institutes have developed in-house test facilities [132]–[139] and employed off-the-shelf solutions [140]–[142]. The architecture of PMU calibrators is quite consolidated. Basically, the PMU calibrator generates the test waveforms through an analog output stage and feeds them to the PMU under test; simultaneously, the calibrator returns the generated waveform to produce the reference synchrophasor. Both the generation and the acquisition stages are driven by a timing stage distinguished by stable clocks and triggers referenced to an absolute timing source, such as a GPS clock or an atomic clock. The main reason behind this kind of design, in which a reference PMU is actually implemented, is the fact that it also allows the calibration of other calibrators [135]. For the present research, this aspect is not necessary: thus, the calibrator architecture has been kept as simple as possible. In fact, it is a generator capable of producing an accurate waveform from the magnitude and timing point of view, equivalent to the reference synchrophasor. The components are

sketched in Figure 36: (i) an accurate GPS disciplined oscillator Trimble Thunderbolt E [143] providing the pulse-per second (PPS) signal and a disciplined 10 MHz reference clock signal; (ii) an NI USB-6346 multifunction I/O device [144], which employs as timing and synchronization sources both the PPS and the 10 MHz signals and outputs the test waveforms from the analog output channel; (iii) a PC running the calibrator software and the calibrator characterization test software, both developed in LabVIEW. The characteristics of the analog output channel (OUT) DAC are summarized in Table 5.27, whereas the characteristics of the GPS disciplined oscillator are shown in Table 5.28.

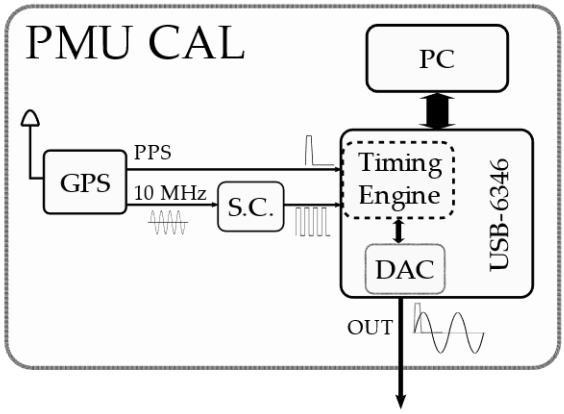

Figure 36 Schematics of the calibrator architecture.

Table 5.27 Calibrator's analog output DAC specifications.

DAC Properties	Value
Resolution	16 bit
Full range	±10 V
Max sampling rate	900 kSa/s

Table 5.28 GPS disciplined oscillator specifications.

GPS Properties	Value
PPS accuracy	15 ns (one sigma)
10 MHz clock accuracy	1.16×10^{-12} Hz (one day average)
10 MHz stability	See Allan deviation graph in [143]

The block denoted as S.C. in Figure 36 is an active electronic circuit that only adapts the 10 MHz AC sinusoidal reference signal to a 10 MHz TTL-compatible digital signal. The internal timing engine of the USB-6346 board is equipped with a phase-locked loop (PLL), which allows deriving the device's main 100 MHz time base from the external 10 MHz reference clock. This means that the DAC sample clock is consequently derived from the external reference clock. The PPS signal serves as a trigger for starting the DAC operations.

5.3.1.2 Characterization and Testing of the Calibrator

In this Paragraph, the adopted test procedures and setups are shown and explained. To characterize the steady-state test waveforms to be applied to the PMU under test, it is necessary to address the magnitude, the phase angle, and the frequency uncertainties. Note that the calibrator hardware is also affected by the timing and the synchronization non-idealities: as defined in [132], the timing non-idealities are the ones related to the deviations from the UTC second rollover, while the synchronization non-idealities are due to the latencies and jitters in the calibrator hardware. These phenomena have direct consequences on the resulting reference waveform phase. In what follows, if not stated otherwise, the test waveform reproduced by the calibrator is a zero-phase, 50 Hz, sinusoidal waveform with a magnitude equal to 5 V (corresponding to 100 % of the rated value for the OPAL RTS analog input, as explained in Sub-Paragraph 5.3.1.2.1). The DAC sampling rate for all the tests discussed in this research is 800 kSa/s.

5.3.1.2.1 Signal Magnitude Test Case

The test waveform magnitude characterization has been considered first. The calibrator analog output is connected directly to the input of a digital multimeter (DMM) HP 3458A. The DMM is set in synchronous sampling mode, which is the most accurate configuration for AC voltage measurement [145]. The standard IEC 60255-118-1 requires that the PMU shall be tested with:

- A voltage signal varying from 80 to 120% of the rated value;
- A current signal varying from 10 to 200% of the rated value.

In a HIL PMU test scenario, the virtual PMU would interact with an electrical power source (voltage and current) by means of proper ITs and signal conditioning stages in between to match the OPAL ADC's full dynamic range (±10 V). Consequently, a successful design would imply the usage of the full ADC range when the current is 200% of the rated value. Given these considerations, the calibrator has been characterized in correspondence with the test points X_1 collected in Table 5.29.

Table 5.29 Steady-state signal magnitude test points.

Set Point (% of Nominal Value)	Peak Set Point (V)	RMS Set Point (V) X_1
10	0.5	≈0.35
20	1	≈0.71
50	2.5	≈1.77
100	5	≈3.54
120	6	≈4.24
150	7.5	≈5.30
200	10	≈7.07

For each test point, 50 repetitions have been performed. Finally, the values measured by the DMM have been compared against the magnitudes set on the calibrator user interface.

5.3.1.2.2 Harmonic Distortion Test Case

To prove the synchrophasor measurement consistency, the PMU under test should be evaluated even in the presence of harmonic disturbances added to the main power frequency signal. The harmonic disturbance is defined as a single harmonic, up to the fiftieth order, with a magnitude equal to 10 % of the power-frequency-signal rated value. Therefore, the calibrator capability of generating this reference waveform has been experimentally checked, connecting its output again to the DMM. It shall be considered that the HP 3458A basic accuracy specifications strictly apply to sinusoidal signals. In [145], an additional "crest-factor error" term can be found. It is well known that the crest-factor error information without any additional indications on the bandwidth is not sufficient to properly evaluate the DMM performance. However, some observations can be made: (i) the harmonic components' amplitudes determine a worst-case crest factor of ≈1.5, resulting in an additional reading error of 0.001 %; (ii) the harmonic components' frequencies are only a few times bigger than the fundamental frequency, and they are contained by far in the bandwidth in which the DMM presents good overall accuracy. In such a scenario, it could be reasonably stated that the DMM accuracy can still be reliably assessed from its specifications. Nevertheless, first, the calibrator has been set to generate only the single harmonic components (X_h in Table 5.30, where h is the harmonic order); second, the test waveform containing both the 50 Hz component and the harmonic component has been produced (X_{1+h} in Table 5.30, where h is the harmonic order). A comparison between the single harmonic signal and the standard harmonic disturbance test waveform has been performed. The test cases are summarized in Table 5.30.

Table 5.30 Steady-state harmonic disturbance test points.

	50 Hz Component (% of Nominal Value)	Harmonic Component Order h	Harmonic Component Magnitude (% of 50 Hz Signal Nominal Value)
Single harmonic component test signal X_h	0	From 2 to 50	10
Standard harmonic distortion test signal X_{1+h}	100	2	10
		3	10
		5	10
		7	10
		11	10
		20	10
		30	10
		50	10

For each test point, 50 repetitions have been performed. Finally, the values measured by the DMM have been compared against the magnitudes set on the calibrator user interface.

5.3.1.2.3 Synchronization Test Case

The synchrophasor measurements are a time-critical application: a timing error of only 31.7 μs causes a 1% TVE error when there is no magnitude error. Thus, it is very important to analyze the behavior of the calibrator from this point of view. The synchronization uncertainty has been evaluated by means of a Tektronix MSO58 12 bits, 3.125 GSa/s oscilloscope [146], as shown in Figure 37. First, the PPS signal from the GPS disciplined clock is also sent to the oscilloscope; second, the USB-6346 has been programmed to also output a square wave from the on-board counter sub-system (CTR); finally, the DAC outputs a square wave (OUT) with the same parameters (amplitude, frequency, and duty-cycle) of the one generated by the counter. This setup allows the evaluation of the calibrator response delay and jitter compared to the PPS signal. Two different square wave frequencies have been examined: 50 Hz and 100 kHz. For each case, 1000 acquisitions have been taken.

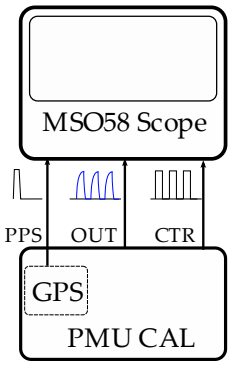

Figure 37 Schematics of the calibrator synchronization test.

Concerning the timing uncertainty, only the GPS disciplined oscillator uncertainty is considered; in fact, the GPS time has been chosen as a UTC time reference. Since the OPAL RTS receives the same PPS signal as the calibrator, there are no additional contributions due to the presence of different timing sources. For instance, if the OPAL RTS and the calibrator had been equipped with different GPS receivers, then the two PPS signals would have been slightly misaligned between each other, even though they would have been under the same sky conditions.

5.3.1.2.4 Frequency and ROCOF Test

The frequency uncertainty has been checked by means of the frequency counter built in the Rigol DG 1022Z arbitrary waveform generator, which provides an accuracy of 1 ppm. The calibrator's test sinusoidal waveform frequency has been tested over the range from 45 to 55 Hz, in steps of 0.5 Hz. For each frequency test point, 100 measurements have been taken. The values measured by the frequency counter have been compared against the frequency value set on the calibrator user interface. Finally, the frequency counter readings have also been used to estimate the calibrator ROCOF since it is basically defined as a variation of the frequency between sequential measurements.

5.3.1.2.5 Phase Displacement Test

An additional investigation has been performed to estimate the calibrator's accuracy in the matter of reproducing the desired initial phase of the sinusoidal test waveform. The test setups are reproduced in Figure 38. To achieve this, the calibrator synthetizes a sinusoidal waveform from each of its two analog output channels (OUT and OUT2), both triggered simultaneously by the PPS. The initial phase of the second sinusoid has been kept fixed and equal to 0 (OUT2), while the initial phase of the first sinusoid has been progressively increased (OUT). In particular, four phase displacements have been tested: 0°, 30°, 45°, 90°. A NI-9239 data

acquisition board (DAQ) has been used to simultaneously acquire the two generated waveforms. The phase displacement has been measured in the frequency domain, and a 10 s long time record has been acquired on each channel to mitigate spectral leakage impairments. Furthermore, a verification of the "actual zero phase displacement" seen by the DAQ channels has been conducted, too, by feeding the same signal to both. A total of 100 repetitions have been carried out for each case. Note that the NI-9239 operation is not triggered by the PPS signal, but this does not matter since the measured quantity is a difference between two steady-state waveforms.

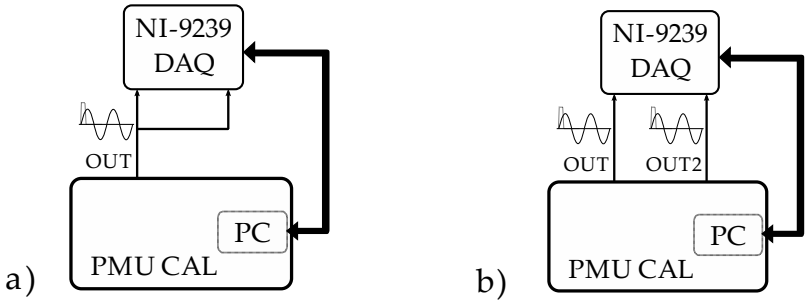

Figure 38 Schematics of the calibrator phase displacement test: (a) "actual zero" test setup; (b) 0, 30, 45, 90° phase-shifted sinusoids test setup.

Finally, the phase displacement values have been compared against the phase displacement set on the calibrator user interface.

5.3.1.3 Results of the Characterization Tests

This Paragraph presents the results obtained from each of the test cases described above.

5.3.1.3.1 Signal Magnitude Test Results

In Table 5.31, the following quantities are reported: $X_1\ RMS^*$ is the ideal RMS value of the sinusoidal test waveform set on the calibrator user interface corresponding to the test points shown in Table 5.29; $\mu_{X_1\ RMS}$ is the average of the RMS values measured by the DMM and $\sigma_{X_1\ RMS}$ is the standard deviation; $u_{A,\ X_1\ RMS}$ and $u_{B,\ X_1\ RMS}$ are the uncertainties evaluated according to the Type A and Type B methods, respectively. Lastly, $\Delta_{X_1\ RMS}$ is a parameter defined as:

$$\Delta_{X_1\ RMS} = X_1\ RMS^* - \mu_{X_1\ RMS} \tag{5.15}$$

Table 5.31 Steady-state signal magnitude characterization results.

$X_1\ RMS^*$ [V]	$\mu_{X_1\ RMS}$ [V]	$\sigma_{X_1\ RMS}$ [V]	$u_{A,\ X_1\ RMS}$ [V]	$u_{B,X_1\ RMS}$ [V]	$\Delta_{X_1\ RMS}$ [V]
0.3535534	0.3535314	2×10^{-6}	3×10^{-7}	3×10^{-5}	2×10^{-5}
0.7071068	0.7070302	2×10^{-6}	3×10^{-7}	4×10^{-5}	8×10^{-5}
1.767767	1.767642	3×10^{-5}	4×10^{-6}	2×10^{-4}	1×10^{-4}
3.535534	3.535152	2×10^{-5}	3×10^{-6}	3×10^{-4}	4×10^{-4}
4.242641	4.242152	2×10^{-5}	3×10^{-6}	3×10^{-4}	5×10^{-4}
5.303301	5.302879	2×10^{-5}	3×10^{-6}	3×10^{-4}	4×10^{-4}
7.071068	7.070681	2×10^{-5}	3×10^{-6}	4×10^{-4}	4×10^{-4}

The main contribution to the uncertainty comes from the DMM a priori evaluation of the measurement uncertainty; in fact, the deviation in the measurement is negligible compared to the former. Moreover, the computed values of $\Delta_{X_1\ RMS}$ show that the deviation between the RMS value of the sinusoidal test waveform produced by the calibrator and the ideal RMS value set on the calibrator user interface is of the same order of magnitude of the uncertainty affecting the DMM measurement.

5.3.1.3.2 Harmonic Distortion Test Results

Given the considerable amount of test points, for readability's sake, only the single harmonic cases which produced the best and the worst results have been reported in Table 5.32. The quantities other than the harmonic order *h* are the same as the ones in Table 5.31, but this time they refer to the tested single harmonic component.

Table 5.32 Steady-state single harmonic component signal characterization results.

h	$X_h\ RMS^*$ [V]	$\mu_{X_h\ RMS}$ [V]	$\sigma_{X_h\ RMS}$ [V]	$u_{A,\ X_h\ RMS}$ [V]	$u_{B,X_h\ RMS}$ [V]	$\Delta_{X_h\ RMS}$ [V]
5	0.3535534	0.3535502	1×10^{-6}	2×10^{-7}	3×10^{-5}	3×10^{-6}
50		0.3535131	1×10^{-6}	1×10^{-7}	4×10^{-5}	4×10^{-5}

The order of magnitude of the $\Delta_{X_h\ RMS}$ values for all the others h cases is 10^{-5}. Not surprisingly, considerations analogous to the ones deduced in Sub-Paragraph 5.3.1.3.1 can be made. In fact, as in the previous case, the DMM acquires sinusoidal signals whose frequency is contained in a bandwidth in which the DMM maintains almost the same accuracy. Table 5.33 is analogous to Table 5.32, but the values for the test signal composed by the power frequency component and the harmonic disturbance are reported.

Table 5.33 Steady-state standard harmonic disturbance signal characterization results.

h	$X_{1+h}\ RMS^*$ [V]	$\mu_{X_{1+h}\ RMS}$ [V]	$\sigma_{X_{1+h}\ RMS}$ [V]	$u_{A,\ X_{1+h}\ RMS}$ [V]	$u_{B,X_{1+h}\ RMS}$ [V]	$\Delta_{X_{1+h}\ RMS}$ [V]
2	3.5531676	3.552858	2×10^{-5}	3×10^{-6}	3×10^{-4}	2.8×10^{-4}
3		3.552888	2×10^{-5}	3×10^{-6}	3×10^{-4}	2.8×10^{-4}
5		3.552913	2×10^{-5}	2×10^{-6}	3×10^{-4}	2.5×10^{-4}
7		3.552886	2×10^{-5}	3×10^{-6}	3×10^{-4}	2.8×10^{-4}
11		3.552876	2×10^{-5}	3×10^{-6}	4×10^{-4}	2.9×10^{-4}
20		3.552886	2×10^{-5}	3×10^{-6}	4×10^{-4}	2.8×10^{-4}
30		3.552893	2×10^{-5}	3×10^{-6}	4×10^{-4}	2.7×10^{-4}
50		3.552720	7×10^{-5}	9×10^{-6}	4×10^{-4}	4.5×10^{-4}

Again, the results obtained are in line with the previous ones, confirming the consistency of the operations.

5.3.1.3.3 Synchronization Test Results

In Figure 39, the PPS signal, the 100 kHz square waveform generated from the analog output (OUT) of the calibrator and the digital square wave reproduced by the digital counter (CTR) are plotted. Figure 40, instead, shows the histograms representing the distribution of the delay measurement between the (a) PPS and the CTR rising fronts and (b) the PPS and the OUT rising fronts.

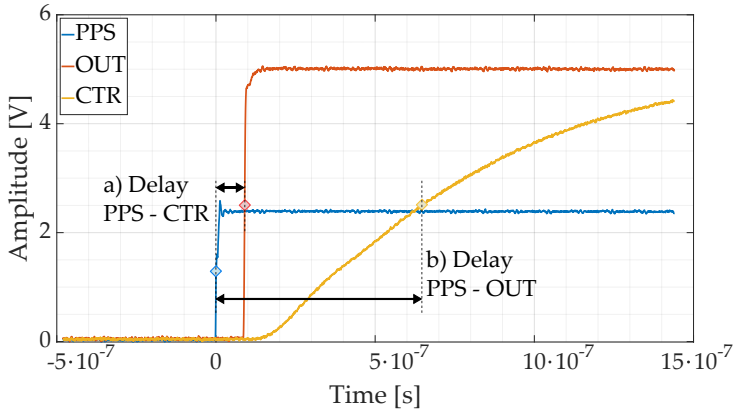

Figure 39 Oscilloscope waveform acquisitions for the board synchronization evaluation. The PPS signal (blue), the CTR signal (red), the OUT signal (yellow).

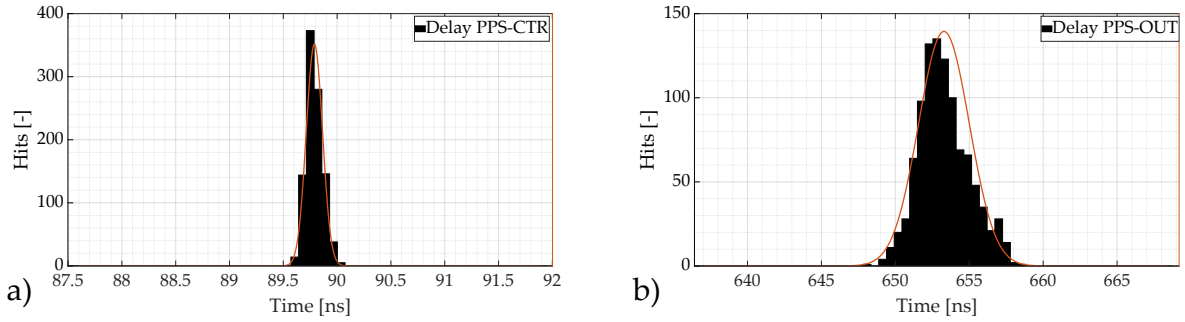

Figure 40 Distribution histograms of the delay measurement between the (a) PPS and the CTR rising fronts and (b) the PPS and the OUT rising fronts.

Other than the locked phase relation among the three waveforms, it is evident that the board outputs the requested signals in a very responsive way. The CTR signal rises almost a single time-base clock tick (≈90 ns) after the detection of the trigger, with low dispersion (less than 100 ps), denoting an immediate response of the board. The OUT signal response behavior shows a systematic delay contribution of ≈ 650 ns and a standard deviation of less than 2 ns (equivalent to ≈ 0.6 µrad). The results for the case of the 50-Hz square waveforms are not reported since they do not differ significantly from the ones already shown.

5.3.1.3.4 Frequency and ROCOF Test Results

Table 5.34 collects the measurements from the frequency characterization of the calibrator. The quantities are: f^* is the frequency reference value set on the calibrator user interface; μ_f is the average frequency measured by the counter; $u_{A,f}$ and $u_{B,f}$ are the corresponding uncertainties evaluated according to Type A and Type B methods, respectively; finally, Δ_f is an error parameter defined as:

$$\Delta_f = f^* - \mu_f, \tag{5.16}$$

Moreover, two parameters that could approximately quantify the ROCOF of the calibrator are represented by μ_{ROCOF} and $\delta_{max\text{-}min}$. The former is defined as:

$$\mu_{ROCOF} = \frac{1}{N-1}\sum_{i=1}^{N\text{-}1}(f_{i+1} - f_i), \tag{5.17}$$

where, $N = 100$ is the number of readings taken by the frequency counter for each value of f^*, and f_i is the *i*-th frequency counter readings. $u_{A,\ ROCOF}$ and $u_{B,\ ROCOF}$ are the associated uncertainty evaluated according to the Type A and Type B method, respectively. In particular, the latter is evaluated as

$$u_{B,\ ROCOF} = \sqrt{2u_{B,f}^2} \tag{5.18}$$

since it is a difference between measured frequency values.

The parameter $\delta_{max\text{-}min}$ is simply the difference between the maximum and the minimum values recorded by the counter at each f^*.

It is well-known that the ROCOF implies a variation of frequency over time. Some considerations about this point can be found below.

Table 5.34 Steady-state signal frequency characterization results.

f^* [Hz]	μ_f [Hz]	$u_{A,f}$ [Hz]	$u_{B,f}$ [Hz]	Δ_f [Hz]	μ_{ROCOF} [Hz]	$u_{A,ROCOF}$ [Hz]	$u_{B,ROCOF}$ [Hz]	$\delta_{max\text{-}min}$ [Hz]
45.0	45.000000	1×10^{-6}	3×10^{-5}	1.5×10^{-7}	0	2×10^{-6}	4×10^{-5}	8×10^{-5}
45.5	45.500002	1×10^{-6}	3×10^{-5}	1.5×10^{-6}	-3×10^{-7}	1×10^{-6}	4×10^{-5}	5×10^{-5}
46.0	46.000001	1×10^{-6}	3×10^{-5}	1.1×10^{-6}	2×10^{-8}	1×10^{-6}	4×10^{-5}	6×10^{-5}
46.5	46.500001	1×10^{-6}	3×10^{-5}	1.4×10^{-6}	9×10^{-8}	1×10^{-6}	4×10^{-5}	6×10^{-5}
47.0	47.000001	1×10^{-6}	3×10^{-5}	1.1×10^{-6}	2×10^{-7}	1×10^{-6}	4×10^{-5}	5×10^{-5}
47.5	47.500002	1×10^{-6}	3×10^{-5}	1.5×10^{-6}	4×10^{-7}	2×10^{-6}	4×10^{-5}	6×10^{-5}
48.0	48.000001	1×10^{-6}	3×10^{-5}	1.4×10^{-6}	2×10^{-7}	1×10^{-6}	4×10^{-5}	5×10^{-5}
48.5	48.500006	1×10^{-6}	3×10^{-5}	5.6×10^{-6}	-1×10^{-7}	1×10^{-6}	4×10^{-5}	6×10^{-5}
49.0	49.000003	1×10^{-6}	3×10^{-5}	2.9×10^{-6}	-2×10^{-7}	1×10^{-6}	4×10^{-5}	5×10^{-5}
49.5	49.500000	1×10^{-6}	3×10^{-5}	4.6×10^{-7}	-4×10^{-8}	2×10^{-6}	4×10^{-5}	7×10^{-5}
50.0	50.000002	8×10^{-7}	3×10^{-5}	2.3×10^{-6}	0	1×10^{-6}	4×10^{-5}	4×10^{-5}
50.5	50.500000	1×10^{-6}	3×10^{-5}	-4.1×10^{-8}	-5×10^{-8}	1×10^{-6}	4×10^{-5}	6×10^{-5}
51.0	51.000001	1×10^{-6}	3×10^{-5}	1.3×10^{-6}	1×10^{-7}	2×10^{-6}	4×10^{-5}	8×10^{-5}
51.5	51.500007	1×10^{-6}	3×10^{-5}	6.6×10^{-6}	2×10^{-7}	2×10^{-6}	4×10^{-5}	6×10^{-5}
52.0	52.000003	1×10^{-6}	3×10^{-5}	3.1×10^{-6}	-2×10^{-8}	2×10^{-6}	4×10^{-5}	7×10^{-5}
52.5	52.500004	1×10^{-6}	3×10^{-5}	4.1×10^{-6}	-1×10^{-7}	2×10^{-6}	4×10^{-5}	7×10^{-5}
53.0	53.000006	1×10^{-6}	3×10^{-5}	5.6×10^{-6}	8×10^{-8}	1×10^{-6}	4×10^{-5}	6×10^{-5}
53.5	53.500004	1×10^{-6}	3×10^{-5}	4.1×10^{-6}	-8×10^{-8}	1×10^{-6}	4×10^{-5}	6×10^{-5}
54.0	54.000005	1×10^{-6}	3×10^{-5}	5.3×10^{-6}	5×10^{-8}	1×10^{-6}	4×10^{-5}	6×10^{-5}
54.5	54.500001	1×10^{-6}	3×10^{-5}	1.3×10^{-6}	-2×10^{-8}	1×10^{-6}	4×10^{-5}	5×10^{-5}
55.0	55.000004	1×10^{-6}	3×10^{-5}	4.0×10^{-6}	7×10^{-8}	2×10^{-6}	4×10^{-5}	6×10^{-5}

The presented results show that the measurement repeatability is less than the frequency counter *a-priori* evaluation of the measurement uncertainty. Additionally, the deviation Δ_f is under that threshold. Even the ROCOF-related quantities suffer the frequency accuracy since they are computed from the measurement uncertainty readings. A final consideration on the evaluation of the ROCOF: since this parameter is the difference between the frequency values at two consecutive reporting instants, in a steady-state scenario, it should ideally be equal to zero. If the waveform synthetized by the calibrator is close to the ideal one, then it is reasonable to expect that its frequency would be almost constant, showing a very small deviation over the entire time interval during which it is examined, not only between two consecutive measurements separated by the reporting interval. In other words, if the reference generator can reproduce a sinusoidal waveform distinguished by a stable frequency over the testing time, then the ROCOF will be small. Hence, this means that an assessment of the stability (expressed in Hz) through the parameters $\delta_{max\text{-}min}$, μ_{ROCOF} and $u_{A,ROCOF}$ can also be used to assess the ROCOF (expressed in Hz/s).

5.3.1.3.5 Phase Displacement Test Results

First, the results obtained from the "actual zero phase displacement" test are shown in Table 5.35.

Table 5.35 "Actual zero phase displacement" characterization results.

$\mu_{\phi 0}$ [rad]	$u_{A,\,\phi 0}$ [rad]
1.27×10^{-7}	4×10^{-9}

Where $\mu_{\phi 0}$ is the average phase displacement between the two DAQ channels when they are sampling the same sinusoidal signal generated by the first analog output channel (OUT) of the calibrator, whereas $u_{A,\,\phi 0}$ is its associated standard uncertainty evaluated by means of the Type A method. This measurement shows the threshold of what can be considered as null phase displacement. Then, the results obtained from the tested four phase displacements are shown in Table 5.36.

Table 5.36 Phase displacement characterization results.

ϕ^*_{OUT} [rad]	ϕ^*_{OUT2} [rad]	μ_{ϕ} [rad]	$u_{A,\,\phi}$ [rad]	Δ_{ϕ} [rad]
0	0	2.690×10^{-6}	4×10^{-9}	-2.7×10^{-6}
0.523598776	0	0.5236015	2×10^{-7}	-2.8×10^{-6}
0.785398163	0	0.7854010	3×10^{-7}	-2.9×10^{-6}
1.570796327	0	1.5707995	4×10^{-7}	-3.2×10^{-6}

The quantities μ_{ϕ} and $u_{A,\,\phi}$ are the same quantities as $\mu_{\phi 0}$ and $u_{A,\,\phi 0}$, but this time they are related to the measurement of the phase displacement between the sinusoidal waveforms generated by the calibrator's two analog output channels, OUT and OUT2. The angles ϕ^*_{OUT} and ϕ^*_{OUT2} are the values of the synthetized sinusoids' initial phases set in the calibrator user interface. Finally, Δ_{ϕ} is:

$$\Delta_{\phi} = (\phi^*_{OUT} - \phi^*_{OUT2}) - \mu_{\phi} \tag{5.19}$$

Looking at Table 5.35 and Table 5.36, the first noticeable thing is the difference between μ_{ϕ} and $\mu_{\phi 0}$ other than their relatively small dispersion, which underlines an actual difference between the two scenarios, probably because the two calibrator analog outputs are not identical to each other. Shifting the focus on Table

5.36, the value Δ_ϕ is substantially the same for all the four phase displacement cases, suggesting the presence of a phase offset between the output channels.

5.3.1.3.6 Characterization Conclusions

After the presentation of the calibrator characterization results in this sub-section, it is possible to summarize them with the goal of drawing an overall picture of the device's performances. Concerning magnitude, the calibrator has proved to be very accurate and precise in terms of reproducing waveforms with the desired RMS value. In the sinusoidal steady-state case, there are no appreciable deviations between the DMM measurement result and the ideal value set on the calibrator user interface. Moreover, the worst relative uncertainty is $1 \cdot 10^{-4}$. The results are also similar in the harmonic test cases. This fact ensures us that the calibrator can provide the virtual PMU with the designed harmonic test waveform. Analogously, the calibrator performs well also under the frequency point of view. No significant deviation has been observed from the frequency counter measurement results, and the worst relative standard uncertainty is 6×10^{-7}. Instead, the ROCOF absolute standard uncertainty is 4×10^{-5} Hz/s (or Hz, according to the considerations made at the end of Sub-Paragraph 5.3.1.3.4). Instead, different main contributions shall be considered for the phase accuracy. First, the 15 ns (≈5 μrad) introduced by the GPS disciplined oscillator; second, the 2 ns deviation (≈0.7 μrad) measured between the rising front of the PPS signal and the analog output step waveform; third, the 0.4 μrad deviation measured with the DAQ; finally, since errors on frequency directly affect the phase, it is possible to also add a contribution which translates the worst frequency uncertainty in an angle, resulting in a ≈6 μrad term. All the conversions from time and frequency to angles have been carried out considering the most precautionary scenario: for example, the phase angle corresponding to a 1-ns time variation, when the frequency is equal to 55 Hz, is greater than the phase angle corresponding to the same 1-ns variation when the frequency is equal to 45 Hz. On the other hand, given the same time window, the phase angle corresponding to a 10-μHz frequency variation, when the frequency is equal to 45 Hz, is greater than[5] the phase angle corresponding to the same 10-μHz variation when the frequency is equal to 55 Hz. Combining all these components as the root of the sum of the squares and considering a 3σ interval, the phase uncertainty is equivalent to $\approx 2 \times 10^{-5}$ rad.

Let us take under examination the equation below shown in [43]:

$$TVE = \sqrt{2(1+ME)(1-cos(PE)) + ME^2} \tag{5.20}$$

[5] relative to the synchrophasor's phase angle.

where ME is the synchrophasor magnitude error and PE is the synchrophasor phase error. Given the conclusions of the analysis presented above, if $ME = 1 \times 10^{-4}$ and $PE = 2 \times 10^{-5}$ rad, then the equivalent TVE of the calibrator is approximately ≈ 0.01 %. This result is compliant with what is recommended in [43] for PMU test systems.

5.3.2 RTS Environment

This Sub-Section aims at briefly presenting the RTS environment in which the virtual PMU is implemented. In particular, the main features of the OPAL simulator are summarized in Paragraph 5.3.2.1, while in Paragraph 5.3.2.2, the virtual PMU to be tested is presented and commented on.

5.3.2.1 Description of the RTS

The adopted RTS system is the OPAL-RT OP 4510 Simulator, which allows running real-time simulations and HIL applications via RT-LAB software. Its main components are depicted in Figure 41, in which each color has a specific meaning. Green is used for the internal components and yellow for the interfaces and connections.

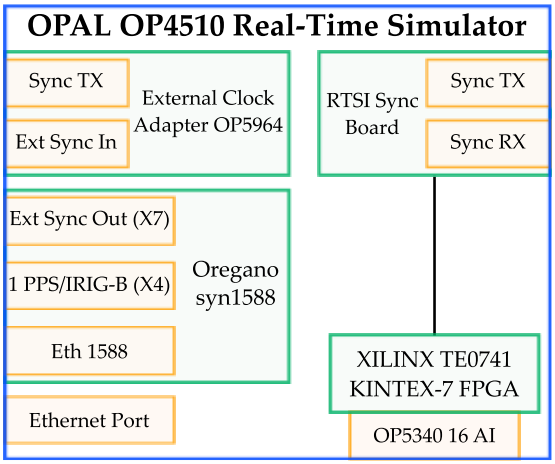

Figure 41 Main components of the OPAL OP4510 RTS.

A brief description of the main components is given in what follows:

- Oregano syn1588 PCIe NIC. It is a PCI Express Ethernet network interface that provides highly accurate clock synchronization via the IEEE 1588 Standard (accuracy of its oscillator higher than 0.05 ppm). The Oregano card can be synchronized with either a PPS signal or an IRIG-B signal from a GPS source (3.3 V signal).
- External Clock Adapter OP5964. It is used to receive and transmit the synchronization signal from the outside to the interfaces.

- RTSI (Real-Time System Interface) Synchronization Board. This board directly communicated with the FPGA, as can be seen from Figure 41 (black line).
- XILINX TE0741 KINTEX-7 FPGA. It can be connected to analog/digital input/output boards. As optional, it can be connected to an extra digital input/output board compatible with RS422 signals. The types of synchronization allowed are LVDS and fiber optic.
- Analog input (AI) card OP5340. It features 16 synchronous differential analog input channels with a maximum voltage range of ±20 V, sampled at 400 kSa/s. The analog to digital converter (ADC) has a 16-bit resolution, and the minimum acquisition time is 2.5 µs per channel. The declared maximum noise of the analog card is 20 mV peak-to-peak. The ADC already includes anti-aliasing filters to remove frequencies higher than 600 kHz.
- Ethernet port. It is used to interface a laptop to the OP4510 RTS.

5.3.2.2 Description of the PMU

Since the discussed PMU is a model implemented within the OPAL-RT, concise considerations regarding the phasor estimation algorithm are given in the following, completing the introduction given in Section 2.3. The easiest method is using the Discrete Fourier Transform (DFT), which allows obtaining the magnitude and phase of the signal. Nevertheless, it must be highlighted that the relevant international standards, such as IEC 60255-118-1, do not provide a specific phasor algorithm to be implemented in PMUs. In scientific literature, many estimation techniques have been investigated and reported. Two main algorithm categories can be distinguished: DFT-based and non-DFT-based algorithms. Examining the first category, the classic DFT-based methods work well when the system frequency is close to the nominal frequency but, due to spectral leakage, significant errors arise when the frequency drifts from its rated value. For this reason, much effort has been made to improve the accuracy of DFT-based estimation algorithms under off-nominal frequency conditions. Among these, it is worth mentioning interpolated-DFT approaches (IpDFT) [147], [148] and dynamic DFT ones [149]. On the other hand, the majority of non-DFT-based algorithms are based on different techniques, such as the sine-fit, demodulation & filtering, and Kalman filters (KFs) [150], [151]. A small number of other approaches are based on different techniques such as Taylor Weighted Least-Squares (TWLS) [152], Space Vectors (SVs) [153], and wavelets [154]. Given the broadness of the topic enveloping several techniques, comparative studies between PMU estimation algorithms have also been presented in the literature. Assessments between different algorithms and techniques are typically performed, as in [151], [155]. These analyses are based on simulations to evaluate and compare the performance of the different estimators. In [151] it is shown that Extended KFs are optimal in changing harmonics and narrowband interference scenarios. On the contrary, DFT approaches do not suffer from instabilities, and they are generally simpler than the latter, resulting in a significantly reduced computational burden. In light of these considerations, and

since the aim of this research is not the achievement of the best estimating algorithm, a simple DFT algorithm is chosen. Next, in Paragraph 5.3.3.1, the characterization tests are described.

5.3.3 Characterization of the PMU

This Sub-Section contains the metrological tests performed on the virtual PMU, to highlight its significant contribution to the uncertainty. The set of tests designed for assessing the performance of the virtual PMU considering the RTS contribution is described in accordance with the standard IEC 60255-118-1. The goal of the tests is an increased awareness by more RTS users in performing preliminary characterization of their virtual models.

5.3.3.1 PMU Testing

The tests performed on the virtual PMU hosted inside the RTS aim to assess the quality of its measurements, focusing on the amplitude, the phase, the frequency, and the harmonic distortion of the signals. For each aspect, a specific test has been performed. For all tests, the time step of the simulator is 50 μs, and the sampling frequency of the analog input DAC is 20 kSa/s.

5.3.3.1.1 Amplitude Tests

The amplitude tests have been designed considering both the current and voltage limits defined in [43]. In fact, the current variation is wider (from 10 % to 200 %); therefore, the RTS DAC max input (10 V) has been associated with 200 % of the rated signal. Consequently, five tests, referred to as A1 to A5, from 200 % to 10 % of the rated signal, are designed and described in Table 5.37. The table contains the phase, the frequency, and the amplitude (peak and RMS) of the adopted signals.

Table 5.37 Settings of the amplitude tests.

Test Name	Peak [V]	RMS [V]	% of Rated [%]	Phase [rad]	Frequency [Hz]
A1	10	7.0710	200	0	50
A2	5	3.5355	100	0	50
A3	2.5	1.7677	50	0	50
A4	1	0.7071	20	0	50
A5	0.1	0.0707	10	0	50

5.3.3.1.2 Frequency Tests

In accordance with [43], nine different tests, referred to as F1 to F9, have been designed for testing the virtual PMU behavior vs. frequency. They are collected in Table 5.38. Adopting 100 % of the rated signal, nine frequency values from 48 Hz to 52 Hz, with steps of 0.5 Hz, have been used. For the frequency tests, the initial phase of the signals is always set to zero.

Table 5.38 Settings of the frequency tests.

Test Name	Peak [V]	RMS [V]	% of Rated [%]	Phase [rad]	Frequency [Hz]
F1	5	3.5355	100	0	48
F2	5	3.5355	100	0	48.5
F3	5	3.5355	100	0	49
F4	5	3.5355	100	0	49.5
F5	5	3.5355	100	0	50
F6	5	3.5355	100	0	50.5
F7	5	3.5355	100	0	51
F8	5	3.5355	100	0	51.5
F9	5	3.5355	100	0	52

5.3.3.1.3 Harmonic Tests

The aim of these tests is to verify the performance of a PMU when a single harmonic component is superimposed to the main frequency signal. In detail, the harmonic component has an amplitude corresponding to the 10 % of the main signal. The defined tests are listed in Table 5.39. For each test, referred to as H1 to H16, the table contains the amplitude of both the main signal and the harmonic component. The tested harmonic components range from the third to the forty-ninth odd harmonics.

Table 5.39 Settings of the harmonic tests.

Test Name	Peak [V]	RMS [V]	% of Rated [%]	Order [-]	% of 50-Hz component [%]
H1	5	3.5355	100	3	10
H2	5	3.5355	100	5	10
H3	5	3.5355	100	7	10
H4	5	3.5355	100	9	10
H5	5	3.5355	100	11	10
H6	5	3.5355	100	15	10
H7	5	3.5355	100	19	10
H8	5	3.5355	100	21	10
H9	5	3.5355	100	25	10
H10	5	3.5355	100	29	10
H11	5	3.5355	100	31	10
H12	5	3.5355	100	35	10
H13	5	3.5355	100	39	10
H14	5	3.5355	100	41	10
H15	5	3.5355	100	45	10
H16	5	3.5355	100	49	10

5.3.3.1.4 Phase Tests

Typical laboratory tests use 0 as the initial phase. However, considering real applications, a set of tests tackling the performance of the virtual PMUs when the phase is not null is necessary. Therefore, Table 5.40 presents 11 tests, referred to as P1 to P11, in which the phase varies from 0° to 100° with steps of 10°. The table also contains the amplitude of the signal (always 100 % of the rated) and the frequency (50 Hz).

Table 5.40 Settings of the phase tests.

Test Name	Peak [V]	RMS [V]	% of Rated [%]	Frequency [Hz]	Phase [°]	Phase [rad]
P1	5	3.5355	100	50	0	0
P2	5	3.5355	100	50	10	0.1745
P3	5	3.5355	100	50	20	0.3490
P4	5	3.5355	100	50	30	0.5235
P5	5	3.5355	100	50	40	0.6981
P6	5	3.5355	100	50	50	0.8726
P7	5	3.5355	100	50	60	1.0471
P8	5	3.5355	100	50	70	1.2217
P9	5	3.5355	100	50	80	1.3962
P10	5	3.5355	100	50	90	1.5707
P11	5	3.5355	100	50	100	1.7453

5.3.3.2 PMU Tests Results

Each test described in Paragraph 5.3.3.1 had a duration of 20 s, during which the quantities have been collected and then averaged to obtain the final results. The mean values and the corresponding standard deviations of the mean are collected in Tables 5.41 – 5.44 for the amplitude, frequency, harmonic, and phase, respectively. Every table contains the RMS value of the measured voltage RMS, its standard deviation of the mean σ_{RMS}, the phase, its standard deviation of the mean σ_{Ph}, the measured frequency, its standard deviation of the mean σ_{Fr}, the ROCOF, and its standard deviation of the mean σ_R.

Table 5.41 Measurement results of the amplitude tests.

Test Name	RMS [V]	σ_{RMS} [V]	Phase [rad]	σ_{Ph} [rad]	Frequency [Hz]	σ_{Fr} [Hz]	ROCOF [Hz/s]	σ_R [Hz/s]
A1	7.0692976	1×10^{-7}	0.0054920	4×10^{-7}	50.0000000	3×10^{-7}	3.24×10^{-7}	2×10^{-5}
A2	3.53433398	9×10^{-8}	0.0088586	4×10^{-7}	50.0000002	3×10^{-7}	1.77×10^{-6}	3×10^{-5}
A3	1.76701027	8×10^{-8}	0.0093632	4×10^{-7}	50.0000000	3×10^{-7}	-4.19×10^{-6}	7×10^{-5}
A4	0.70625170	8×10^{-8}	−0.0035345	3×10^{-7}	50.0000004	3×10^{-7}	1.25×10^{-6}	2×10^{-4}
A5	0.06985583	8×10^{-8}	0.007932	3×10^{-6}	49.999975	2×10^{-6}	-1.35×10^{-5}	2×10^{-3}

Table 5.42 Measurement results of the frequency tests.

Test Name	RMS [V]	σ_{RMS} [V]	Phase [rad]	σ_{Ph} [rad]	Frequency [Hz]	σ_{Fr} [Hz]	ROCOF [Hz/s]	σ_R [Hz/s]
F1	3.5343752	1×10^{-7}	0.0073137	4×10^{-7}	48.0000000	3×10^{-7}	-9.19×10^{-7}	5×10^{-5}
F2	3.5344621	1×10^{-7}	0.0119328	4×10^{-7}	48.4999925	2×10^{-7}	3.94×10^{-5}	5×10^{-5}
F3	3.53431802	9×10^{-8}	0.0092100	4×10^{-7}	48.9999999	3×10^{-7}	-1.17×10^{-6}	5×10^{-5}
F4	3.5344581	1×10^{-7}	0.008737	1×10^{-6}	49.5000027	3×10^{-7}	-2.72×10^{-6}	5×10^{-5}
F5	3.53448223	8×10^{-8}	−0.0031022	4×10^{-7}	49.9999971	3×10^{-7}	4.90×10^{-5}	3×10^{-5}
F6	3.5344243	1×10^{-7}	−0.0027930	6×10^{-7}	50.4999894	2×10^{-7}	-3.13×10^{-7}	5×10^{-5}
F7	3.5342794	1×10^{-7}	0.0034803	5×10^{-7}	50.9999988	3×10^{-7}	1.24×10^{-5}	5×10^{-5}
F8	3.5344108	1×10^{-7}	0.0072208	4×10^{-7}	51.4999955	3×10^{-7}	9.18×10^{-7}	6×10^{-5}
F9	3.5342751	1×10^{-7}	−0.0047451	4×10^{-7}	52.0000001	3×10^{-7}	-2.46×10^{-6}	6×10^{-5}

Table 5.43 Measurement results of the harmonic tests.

Test Name	RMS [V]	σ_{RMS} [V]	Phase [rad]	σ_{Ph} [rad]	Frequency [Hz]	σ_{Fr} [Hz]	ROCOF [Hz/s]	σ_R [Hz/s]
H1	3.53444568	8×10^{-8}	0.0055126	4×10^{-7}	50.0000008	3×10^{-7}	-1.60×10^{-6}	3×10^{-5}
H2	3.53421753	9×10^{-8}	0.0076177	8×10^{-7}	50.0000070	3×10^{-7}	-1.51×10^{-6}	4×10^{-5}
H3	3.53443023	9×10^{-8}	0.0089869	7×10^{-7}	50.0000075	3×10^{-7}	-1.17×10^{-6}	4×10^{-5}
H4	3.5342145	1×10^{-7}	0.0082917	9×10^{-7}	50.0000136	3×10^{-7}	1.65×10^{-6}	4×10^{-5}
H5	3.53439991	8×10^{-8}	0.0091382	5×10^{-7}	49.9999942	2×10^{-7}	1.99×10^{-6}	4×10^{-5}
H6	3.5343785	1×10^{-7}	0.0054355	5×10^{-7}	50.0000072	3×10^{-7}	2.26×10^{-6}	4×10^{-5}
H7	3.5343746	1×10^{-7}	0.0072207	4×10^{-7}	50.0000003	3×10^{-7}	3.37×10^{-8}	4×10^{-5}
H8	3.5343741	2×10^{-7}	0.0076282	4×10^{-7}	50.0000000	3×10^{-7}	3.14×10^{-7}	4×10^{-5}
H9	3.5342377	2×10^{-7}	0.0085004	9×10^{-7}	49.9999873	2×10^{-7}	-2.13×10^{-7}	5×10^{-5}
H10	3.5356639	1×10^{-7}	0.005984	6×10^{-6}	50.0000197	7×10^{-7}	-4.50×10^{-6}	7×10^{-5}
H11	3.5350865	1×10^{-7}	0.0081300	5×10^{-7}	50.0000089	3×10^{-7}	2.50×10^{-6}	5×10^{-5}
H12	3.5349436	1×10^{-7}	0.0070349	3×10^{-7}	49.9999980	2×10^{-7}	-2.99×10^{-6}	5×10^{-5}
H13	3.5348042	2×10^{-7}	0.0097929	3×10^{-7}	49.9999977	2×10^{-7}	-1.06×10^{-6}	5×10^{-5}
H14	3.5347333	1×10^{-7}	0.008859	2×10^{-6}	50.0000258	3×10^{-7}	7.53×10^{-7}	6×10^{-5}
H15	3.53484464	9×10^{-8}	0.0043363	4×10^{-7}	49.9999995	3×10^{-7}	9.23×10^{-7}	5×10^{-5}
H16	3.5346480	2×10^{-7}	0.008433	1×10^{-6}	50.0000127	3×10^{-7}	-1.27×10^{-6}	6×10^{-5}

Table 5.44 Measurement results of the phase tests.

Test Name	RMS [V]	σ_{RMS} [V]	Phase [rad]	σ_{Ph} [rad]	Frequency [Hz]	σ_{Fr} [Hz]	ROCOF [Hz/s]	σ_R [Hz/s]
P1	3.53407799	9×10^{-8}	0.0113214	8×10^{-7}	50.0000045	3×10^{-7}	2.46×10^{-7}	3×10^{-5}
P2	3.53414587	8×10^{-8}	0.1757891	4×10^{-7}	49.9999982	3×10^{-7}	1.93×10^{-6}	3×10^{-5}
P3	3.53423390	8×10^{-8}	0.3574863	4×10^{-7}	49.9999988	3×10^{-7}	-4.54×10^{-6}	3×10^{-5}
P4	3.53424212	8×10^{-8}	0.5307076	4×10^{-7}	49.9999991	3×10^{-7}	-1.11×10^{-6}	3×10^{-5}
P5	3.5341987	1×10^{-7}	0.7064876	7×10^{-7}	50.0000064	3×10^{-7}	-1.29×10^{-5}	3×10^{-5}
P6	3.53416886	9×10^{-8}	0.8733776	4×10^{-7}	49.9999999	3×10^{-7}	-9.72×10^{-6}	3×10^{-5}
P7	3.53417573	9×10^{-8}	1.0548074	4×10^{-7}	49.9999991	3×10^{-7}	-3.91×10^{-6}	3×10^{-5}
P8	3.5340813	1×10^{-7}	1.224595	2×10^{-6}	50.0000105	4×10^{-7}	-5.17×10^{-6}	4×10^{-5}
P9	3.5340916	1×10^{-7}	1.4034948	4×10^{-7}	49.9999980	3×10^{-7}	-7.36×10^{-6}	3×10^{-5}
P10	3.5340525	1×10^{-7}	1.5760936	8×10^{-7}	49.9999852	3×10^{-7}	-5.18×10^{-6}	3×10^{-5}
P11	3.53407339	8×10^{-8}	1.7542494	4×10^{-7}	49.9999982	3×10^{-7}	-9.10×10^{-6}	3×10^{-5}

From these Tables, it can be observed that the results are quite coherent, and, in particular, the standard deviation of the mean (the absolute one) is always in the order of 10^{-8}, 10^{-7}, 10^{-7}, and 10^{-5} for the amplitude, phase, frequency, and ROCOF, respectively. For the sake of readability of the results, Figure 42 shows the RMS vs. frequency (left) and the RMS for each harmonic test (right) taken from Tables 5.42 and 5.43, respectively.

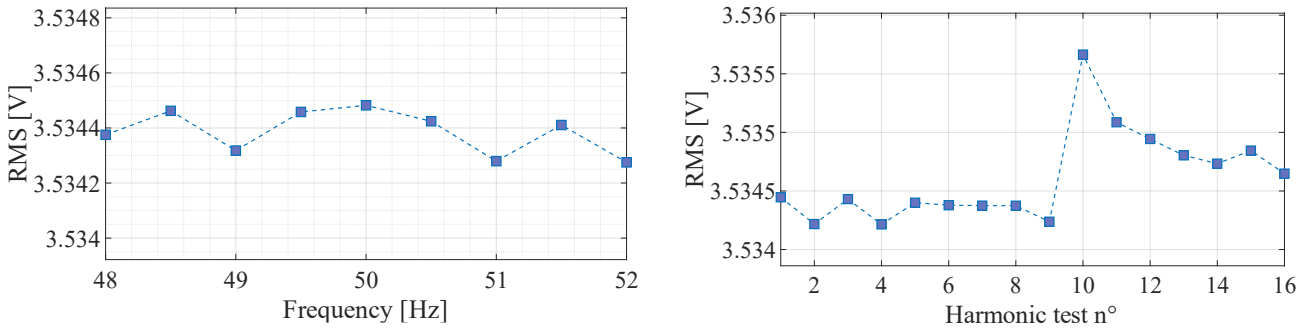

Figure 42 RMS vs frequency test results from Table 5.42 (left) and RMS for each harmonic test (right) from Table 5.43.

Despite the good preliminary results, it is necessary to evaluate them according to the indices defined in [43]. Furthermore, the propagation of the uncertainty process is fundamental to quantify and assess the accuracy of the presented results. To this purpose, the results presented in Tables 5.41 – 5.44, along with the reference values provided and set by the reference calibrator, are used to compute the TVE, FE, and RFE for each of the performed tests. The obtained indices are collected in Tables 5.45–5.48 for the amplitude,

frequency, harmonics, and phase, respectively. The tables are coherent among each other, and they contain: TVE, FE, RFE, and their combined uncertainties u_{TVE}, u_{FE}, and u_{RFE}, respectively. The uncertainty associated with TVE u_{TVE} has been computed from the following contributions to the uncertainty: the measured synchrophasors' rms and phase uncertainties (Type A evaluation), directly obtained from the corresponding standard deviations of the mean (see Tables 5.41 – 5.44); the reference synchrophasor's magnitude and phase uncertainties, obtained from the results of calibrator characterization in Paragraph 5.3.1.3. Instead, u_{FE} has been computed from: the measured frequency uncertainty and the calibrator's frequency uncertainty. Finally, for u_{RFE} is the same as per u_{FE}, but with the ROCOF contributions to the uncertainty. Concerning the propagation of the uncertainties, they are straightforward for u_{FE} and u_{RFE}, since the indexes' formula is a subtraction, while for u_{TVE} the Monte Carlo method has been used (10^5 trials).

Table 5.45 Accuracy indices for the amplitude tests.

Test Name	TVE [%]	u_{TVE} [-]	FE [Hz]	u_{FE} [Hz]	RFE [Hz/s]	u_{RFE} [Hz/s]
A1	0.551	2×10^{-5}	-3×10^{-8}	3×10^{-5}	3×10^{-7}	5×10^{-5}
A2	0.312	2×10^{-5}	-3×10^{-6}	3×10^{-5}	5×10^{-5}	5×10^{-5}
A3	0.937	1×10^{-5}	-3×10^{-8}	3×10^{-5}	-4×10^{-6}	8×10^{-5}
A4	0.373	2×10^{-5}	4×10^{-7}	3×10^{-5}	1×10^{-6}	2×10^{-4}
A5	1.4432	7×10^{-6}	-3×10^{-5}	3×10^{-5}	-1×10^{-5}	2×10^{-3}

Table 5.46 Accuracy indices for the frequency tests.

Test Name	TVE [%]	u_{TVE} [-]	FE [Hz]	u_{FE} [Hz]	RFE [Hz/s]	u_{RFE} [Hz/s]
F1	0.732	1×10^{-5}	-4×10^{-8}	3×10^{-5}	-9×10^{-7}	7×10^{-5}
F2	1.194	1×10^{-5}	-7×10^{-6}	3×10^{-5}	4×10^{-5}	6×10^{-5}
F3	0.922	1×10^{-5}	-5×10^{-8}	3×10^{-5}	-1×10^{-6}	6×10^{-5}
F4	0.874	1×10^{-5}	3×10^{-6}	3×10^{-5}	-3×10^{-6}	6×10^{-5}
F5	0.312	2×10^{-5}	-3×10^{-6}	3×10^{-5}	5×10^{-5}	5×10^{-5}
F6	0.282	3×10^{-5}	-1×10^{-5}	3×10^{-5}	-3×10^{-7}	6×10^{-5}
F7	0.350	2×10^{-5}	-1×10^{-6}	3×10^{-5}	1×10^{-5}	7×10^{-5}
F8	0.723	1×10^{-5}	-4×10^{-6}	3×10^{-5}	9×10^{-7}	7×10^{-5}
F9	0.476	2×10^{-5}	1×10^{-7}	3×10^{-5}	-2×10^{-6}	7×10^{-5}

Table 5.47 Accuracy indices for the harmonic tests.

Test Name	TVE [%]	u_{TVE} [-]	FE [Hz]	u_{FE} [Hz]	RFE [Hz/s]	u_{RFE} [Hz/s]
H1	0.552	2×10^{-5}	8×10^{-7}	3×10^{-5}	-2×10^{-6}	5×10^{-5}
H2	0.763	1×10^{-5}	7×10^{-6}	3×10^{-5}	-2×10^{-6}	5×10^{-5}
H3	0.899	1×10^{-5}	7×10^{-6}	3×10^{-5}	-1×10^{-6}	5×10^{-5}
H4	0.830	1×10^{-5}	1×10^{-5}	3×10^{-5}	2×10^{-6}	5×10^{-5}
H5	0.914	1×10^{-5}	-6×10^{-6}	3×10^{-5}	2×10^{-6}	5×10^{-5}
H6	0.545	2×10^{-5}	7×10^{-6}	3×10^{-5}	2×10^{-6}	6×10^{-5}
H7	0.723	1×10^{-5}	3×10^{-7}	3×10^{-5}	3×10^{-8}	6×10^{-5}
H8	0.764	1×10^{-5}	3×10^{-9}	3×10^{-5}	3×10^{-7}	6×10^{-5}
H9	0.851	1×10^{-5}	-1×10^{-5}	3×10^{-5}	-2×10^{-7}	6×10^{-5}
H10	0.599	1×10^{-5}	2×10^{-5}	3×10^{-5}	-5×10^{-6}	8×10^{-5}
H11	0.813	1×10^{-5}	9×10^{-6}	3×10^{-5}	2×10^{-6}	6×10^{-5}
H12	0.704	1×10^{-5}	-2×10^{-6}	3×10^{-5}	-3×10^{-6}	6×10^{-5}
H13	0.980	1×10^{-5}	-2×10^{-6}	3×10^{-5}	-1×10^{-6}	6×10^{-5}
H14	0.886	1×10^{-5}	3×10^{-5}	3×10^{-5}	8×10^{-7}	7×10^{-5}
H15	0.435	1×10^{-5}	-5×10^{-7}	3×10^{-5}	9×10^{-7}	6×10^{-5}
H16	0.844	1×10^{-5}	1×10^{-5}	3×10^{-5}	-1×10^{-6}	7×10^{-5}

Starting from Table 5.45, different comments arise. In the table, but also for the following ones, when the module of the mean value is smaller than the obtained combined uncertainty, it has been chosen to report the number with one significant digit and not to put a zero. Such a choice is supported by the aim of showing the discrepancies between the order of magnitude of the quantity and its combined uncertainty. Therefore, the significant digits are coherent only in the case of combined uncertainty lower than the mean value. Another comment involves the indices. While FE and RFE are always below the limits defined by [43] (even if a test involving the amplitude variation is not defined), the TVE exceeds the limits in test A5. Such a test is the one with the smallest input test signal (10 % of the rated value). It is important then to understand the capabilities of the RTS system before using them for simulating purposes. As in the case of the tests, it is demonstrated from the results of Table 5.45 that the characterization of the virtual PMU in terms of amplitude is fundamental to know and correct the values during normal operations. For the results in Table 5.46, what is stated for RFE

and FE in the case of Table 5.45 still applies. However, the TVE does not always remain within the limits of the standard. In particular, it exceeds 1% in test F2 and is 0.922 in test F3. On average, all frequency test results are not really satisfactory, and the reason can be attributed to the acquisition process of the RTS. Table 5.47 lists the indices computed in the case of the harmonic tests. From the results, it emerges that FE and RFE are far below the defined limits. As for TVE, it is below the 1% limits in all tests, but on average is always higher than 0.6%. For a better overview of the TVE results, considering the number of digits involved, Figure 43 has been used.

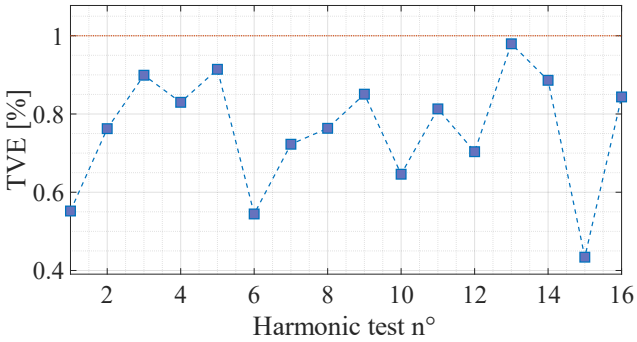

Figure 43 TVE obtained in each harmonic test from H1 to H16.

Identical comments can be made for the results in Table 5.48, which contain the indices computed for the phase tests.

Table 5.48 Accuracy indices for the phase tests.

Test Name	TVE [%]	u_{TVE} [-]	FE [Hz]	u_{FE} [Hz]	RFE [Hz/s]	u_{RFE} [Hz/s]
P1	0.312	2×10^{-5}	-3×10^{-6}	3×10^{-5}	5×10^{-5}	5×10^{-5}
P2	0.133	6×10^{-5}	-2×10^{-6}	3×10^{-5}	2×10^{-6}	5×10^{-5}
P3	0.843	1×10^{-5}	-1×10^{-6}	3×10^{-5}	-5×10^{-6}	5×10^{-5}
P4	0.712	2×10^{-5}	-9×10^{-7}	3×10^{-5}	-1×10^{-6}	5×10^{-5}
P5	0.837	1×10^{-5}	6×10^{-6}	3×10^{-5}	-1×10^{-5}	5×10^{-5}
P6	0.08	1×10^{-4}	-8×10^{-8}	3×10^{-5}	-1×10^{-5}	5×10^{-5}
P7	0.762	1×10^{-5}	-9×10^{-7}	3×10^{-5}	-4×10^{-6}	5×10^{-5}
P8	0.290	3×10^{-5}	1×10^{-5}	3×10^{-5}	-5×10^{-6}	5×10^{-5}
P9	0.724	2×10^{-5}	-2×10^{-6}	3×10^{-5}	-7×10^{-6}	5×10^{-5}
P10	0.532	2×10^{-5}	-1×10^{-5}	3×10^{-5}	-5×10^{-6}	5×10^{-5}
P11	0.893	1×10^{-5}	-2×10^{-6}	3×10^{-5}	-9×10^{-6}	5×10^{-5}

In light of all results presented in the previous tables, it can be concluded that the characterization of a virtual PMU inside an RTS environment is fundamental for accuracy purposes (see Figure 44 for a simplified block diagram of the conducted research). In fact, what was obtained clearly emphasizes the need for a priori knowledge of the performance of each component to be used within a measurement setup. This is to avoid unnecessary propagation of uncertainties from one component to another. In the specific case considered, the single contribution of the RTS is not negligible, and in some cases, the limits defined by the standard [43] are not satisfied. In addition, the results must be assessed considering that the source of the test signals was generated by an accurate calibrator (see Sub-Paragraph 5.3.1.3.6). Consequently, if real sensors with typical accuracy ranging from accuracy class 0.5–1 are considered, the overall uncertainty propagated in the final results would significantly increase.

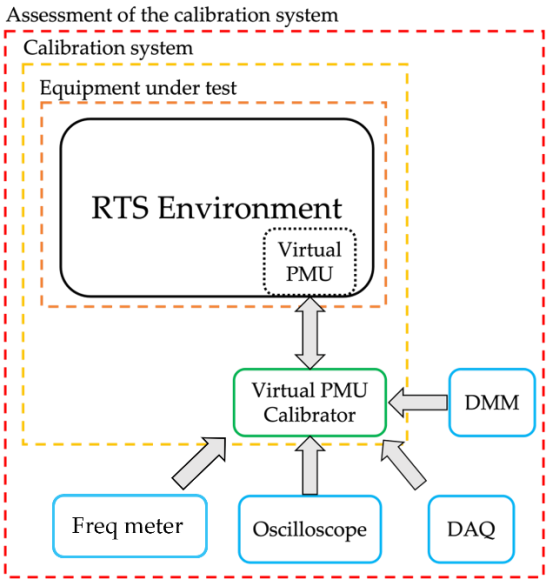

Figure 44 Block diagram of the complete research.

5.3.4 Conclusions

The use of real-time simulators among researchers and utilities is increasing day after day. This allows enhancing the simulation capabilities, including the possibility to recreate complete digital models of the power network and its components. However, the RTSs must ensure a high level of accuracy for their results to be reliable enough for the final users. This aspect is not always considered and sufficiently treated. The research discussed in this Section has the aim of emphasizing and supporting, with rigorous experimental activity, the lack of methodology found in the literature. A virtual PMU implemented within an OPAL RTS has been characterized, according to the IEEE 60255-118-1 standard. To do this, first, a PMU calibrator has been developed and characterized. The main result of the virtual PMU characterization is not the index remaining within or exceeding the limits. The main result is the experimental evidence that the preliminary characterization of the virtual PMU is mandatory when an RTS environment is used. Such a result is confirmed by the performed tests, and its importance can be extended to all activities involving an RTS, not necessarily correlated to power networks or electrical engineering in general.

Conclusions

This dissertation presents the 3-year research work that has been conducted on the measurements applied to the modern power system's issues. In particular, an attempt to add new knowledge with respect to the existing literature has been made, in terms of the characterization of sensors and instrumentation, which are important in the contexts of the distribution grid monitoring and the electrical assets diagnostics. Before the discussion of the research activity and the related main results, the theoretical background has been described in the first three chapters: first, the "Smart Grid" concept and some of the issues faced by the distribution system operators, in which the role of measurements is important for the optimal system operation; second, the sensors and the instrumentation mostly involved in the metrological characterization studies; after that, the methodology for the measurement uncertainty evaluation adopted in the research characterization activities has been shown. Finally, Chapter 4 and Chapter 5 contain the core of the research work.

Chapter 4 reports the research on the measurement applied to the electrical asset diagnostics, which has involved the development and the characterization of an innovative measurement system. One major issue of the distribution system operators is the diagnostics of the electrical assets deployed across the grid, especially the outdoor ones installed in rural areas. To face this problem, an innovative drone-based measurement system has been proposed for monitoring medium voltage surge arresters. This system can detect the surge arrester leakage current, by means of an acquisition system equipped with a toroidal current transformer, which has been characterized. The acquisition system is installed on the ground, and, during the flight, the drone-mounted system collects the information from the field through a wireless radiofrequency communication link.

Chapter 5, instead, deals with the research regarding the measurements applied to the grid monitoring, in which a thorough metrological characterization of MV inductive current transformers, low-voltage energy meters and virtual PMU has been carried out. The distribution system operators need to know how much accurate the primary information employed as input for the system control management are. This information comes from the sensors and instrumentation installed across the grid, but, recently, also the usage of information coming from real-time simulators, such as in digital twin and hardware-in-the-loop applications, has been proposed.

As for the low-voltage electronic energy meters, their behavior under off-nominal power conditions and the relevant standards have been studied. Non-conventional test procedures have been designed for frequency, for current and voltage harmonic distortions, considered as influence quantities: the idea has been to create a new set of test waveforms to test the energy meters in more realistic scenarios, compared to the ones offered by the standards' procedures. Consequently, these tests have been performed and the effects on the energy meters' performance has been evaluated by using the percentage error index. The results show that the different

test conditions allow to detect variations of energy meters accuracy and each one of the devices under test respond differently.

Regarding the MV inductive current transformers, two off-the-shelf units have been characterized in terms of their accuracy in presence of current distortion. To do this, an original procedure has been followed, consisting in sampling the test waveforms directly from the network and then applying them to the current transformers' primary winding. The accuracy has been evaluated by means of the composite error index, and its approximated version, which have been proved to be useful indexes in presence of harmonic distortion. Moreover, this study shows that the inductive current transformers' accuracy is practically not affected by the current distortion levels that can be found in the medium voltage networks. These results also allowed the experimental validation of a closed-form expression for the measured THD uncertainty estimation, which has been confirmed to be a tool that could be useful to derive the THD uncertainty in the on-field measurements by the system operators.

Finally, the metrological characterization of a virtual PMU has been tackled as last part of the research work in Chapter 5. First, a PMU calibrator has been designed, and the uncertainty associated with its steady-state reference phasor has been assessed in terms of amplitude, frequency, and phase. Then, the PMU calibrator acted as a reference, and it has been employed to characterize the PMU implemented within a real-time simulator. After that, the TVE, FE and RFE for the virtual PMU have been computed. It has been observed that the overall virtual PMU performance is far from being ideal, but, nevertheless the main result of this research is highlighting the importance of characterizing such systems before their usage in power system applications.

References

[1] H. Farhangi, “The path of the smart grid,” *IEEE Power Energy Mag.*, vol. 8, no. 1, pp. 18–28, Jan. 2010, doi: 10.1109/MPE.2009.934876.

[2] X. Fang, S. Misra, G. Xue, and D. Yang, “Smart Grid — The New and Improved Power Grid: A Survey,” *IEEE Commun. Surv. Tutor.*, vol. 14, no. 4, pp. 944–980, 2012, doi: 10.1109/SURV.2011.101911.00087.

[3] C. Cecati, G. Mokryani, A. Piccolo, and P. Siano, “An overview on the smart grid concept,” in *IECON 2010 - 36th Annual Conference on IEEE Industrial Electronics Society*, Nov. 2010, pp. 3322–3327. doi: 10.1109/IECON.2010.5675310.

[4] European Commission, “Commission staff working document - Definition, expected services, functionalities and benefits of Smart Grids,” EC, Brussels, Apr. 2011. Accessed: Aug. 04, 2021. [Online]. Available: https://eur-lex.europa.eu/legal-content/EN/TXT/?uri=CELEX%3A52011SC0463

[5] L. Peretto, “The role of measurements in the smart grid era,” *IEEE Instrum. Meas. Mag.*, vol. 13, no. 3, pp. 22–25, Jun. 2010, doi: 10.1109/MIM.2010.5475163.

[6] G. Rietveld *et al.*, “Measurement Infrastructure to Support the Reliable Operation of Smart Electrical Grids,” *IEEE Trans. Instrum. Meas.*, vol. 64, no. 6, pp. 1355–1363, Jun. 2015, doi: 10.1109/TIM.2015.2406056.

[7] R. K. Aggarwal, A. T. Johns, J. A. S. B. Jayasinghe, and W. Su, “An overview of the condition monitoring of overhead lines,” *Electr. Power Syst. Res.*, vol. 53, no. 1, pp. 15–22, Jan. 2000, doi: 10.1016/S0378-7796(99)00037-1.

[8] J. Armitt, M. Cojan, C. Manuzio, and P. Nicolini, “Calculation of wind loadings on components of overhead lines,” *Proc. Inst. Electr. Eng.*, vol. 122, no. 11, pp. 1247–1252, Nov. 1975, doi: 10.1049/piee.1975.0306.

[9] P. Carer and C. Briend, “Weather Impact on Components Reliability: A Model for MV Electrical Networks,” in *Proceedings of the 10th International Conference on Probablistic Methods Applied to Power Systems*, May 2008, pp. 1–7.

[10] S. M. Gubanski, A. Dernfalk, J. Andersson, and H. Hillborg, “Diagnostic Methods for Outdoor Polymeric Insulators,” *IEEE Trans. Dielectr. Electr. Insul.*, vol. 14, no. 5, pp. 1065–1080, Oct. 2007, doi: 10.1109/TDEI.2007.4339466.

[11] D. Kind, *High-Voltage Insulation Technology: Textbook for Electrical Engineers*. Vieweg+Teubner Verlag, 1985. doi: 10.1007/978-3-663-14090-0.

[12] S. Chakravorti, D. Dey, and B. Chatterjee, *Recent Trends in the Condition Monitoring of Transformers: Theory, Implementation and Analysis*. London: Springer-Verlag, 2013. doi: 10.1007/978-1-4471-5550-8.

[13] X. Li, L. Jin, J. Cai, and H. Shi, “Surface discharge detection of external insulation of outdoor vacuum circuit breaker based on ultraviolet imaging,” in *2016 27th International Symposium on Discharges and Electrical Insulation in Vacuum (ISDEIV)*, Sep. 2016, vol. 1, pp. 1–4. doi: 10.1109/DEIV.2016.7748688.

[14] S. Tao *et al.*, “Transient Earth Voltage detection technique for switchgears in distribution network,” in *2016 International Conference on Condition Monitoring and Diagnosis (CMD)*, Sep. 2016, pp. 542–545. doi: 10.1109/CMD.2016.7757882.

[15] Hydroelectric Research and Technical Services Group, Denver Office, and Bureau of Reclamation, *Transformers: basics, maintenance, and diagnostics*. Denver, USA: U.S. Dept. of the Interior, Bureau of Reclamation, 2005. Accessed: Aug. 10, 2021. [Online]. Available: https://purl.fdlp.gov/GPO/LPS113746

[16] D. Jones, “Power line inspection - a UAV concept,” in *2005 The IEE Forum on Autonomous Systems (Ref. No. 2005/11271)*, Nov. 2005, p. 8 pp.-. doi: 10.1049/ic:20050472.

[17] J. Katrasnik, F. Pernus, and B. Likar, “A Survey of Mobile Robots for Distribution Power Line Inspection,” *IEEE Trans. Power Deliv.*, vol. 25, no. 1, pp. 485–493, Jan. 2010, doi: 10.1109/TPWRD.2009.2035427.

[18] A. R. Ungaro and P. Sartori, “I velivoli a pilotaggio remoto e la sicurezza europea,” *IAI Istituto Affari Internazionali*, Jul. 15, 2016. https://www.iai.it/it/pubblicazioni/i-velivoli-pilotaggio-remoto-e-la-sicurezza-europea (accessed Aug. 10, 2021).

[19] L. F. Luque-Vega, B. Castillo-Toledo, A. Loukianov, and L. E. Gonzalez-Jimenez, “Power line inspection via an unmanned aerial system based on the quadrotor helicopter,” in *MELECON 2014 - 2014 17th IEEE Mediterranean Electrotechnical Conference*, Apr. 2014, pp. 393–397. doi: 10.1109/MELCON.2014.6820566.

[20] R. Z. Homma, A. Cosentino, and C. Szymanski, “Autonomous inspection in transmission and distribution power lines – methodology for image acquisition by means of unmanned aircraft system and its treatment and storage,” *CIRED - Open Access Proc. J.*, vol. 2017, no. 1, pp. 965–967, Oct. 2017, doi: 10.1049/oap-cired.2017.0290.

[21] e-distribuzione S.p.A., “Il volo tecnologico | e-distribuzione.” https://www.e-distribuzione.it/progetti-e-innovazioni/droni.html (accessed Aug. 10, 2021).

[22] A. Cavallini, D. Fabiani, G. Mazzanti, and G. C. Montanari, “Models for degradation of self-healing capacitors operating under voltage distortion and temperature,” in *Proceedings of the 6th International Conference on Properties and Applications of Dielectric Materials (Cat. No.00CH36347)*, Jun. 2000, vol. 1, pp. 108–111 vol.1. doi: 10.1109/ICPADM.2000.875641.

[23] P. Caramia, G. Carpinelli, P. Verde, G. Mazzanti, A. Cavallini, and G. C. Montanari, “An approach to life estimation of electrical plant components in the presence of harmonic distortion,” in *Ninth International Conference on Harmonics and Quality of Power. Proceedings (Cat. No.00EX441)*, Oct. 2000, vol. 3, pp. 887–892 vol.3. doi: 10.1109/ICHQP.2000.896846.

[24] “EN 50160:2010+A3:2019 Voltage characteristics of electricity supplied by public electricity networks,” CENELEC, European Standard, Sep. 2019.

[25] “IEEE Recommended Practice and Requirements for Harmonic Control in Electric Power Systems,” *IEEE Std 519-2014 Revis. IEEE Std 519-1992*, pp. 1–29, Jun. 2014, doi: 10.1109/IEEESTD.2014.6826459.

[26] S. K. Rönnberg *et al.*, “On waveform distortion in the frequency range of 2kHz–150kHz—Review and research challenges,” *Electr. Power Syst. Res.*, vol. 150, pp. 1–10, Sep. 2017, doi: 10.1016/j.epsr.2017.04.032.

[27] A. Abur and A. G. Expósito, *Power System State Estimation Theory and Implementation*, 1st ed. CRC Press, 2004.

[28] A. von Meier, E. Stewart, A. McEachern, M. Andersen, and L. Mehrmanesh, “Precision Micro-Synchrophasors for Distribution Systems: A Summary of Applications,” *IEEE Trans. Smart Grid*, vol. 8, no. 6, pp. 2926–2936, Nov. 2017, doi: 10.1109/TSG.2017.2720543.

[29] M. Pignati *et al.*, “Real-time state estimation of the EPFL-campus medium-voltage grid by using PMUs,” in *2015 IEEE Power Energy Society Innovative Smart Grid Technologies Conference (ISGT)*, Feb. 2015, pp. 1–5. doi: 10.1109/ISGT.2015.7131877.

[30] M. Pau *et al.*, “Design and Accuracy Analysis of Multilevel State Estimation Based on Smart Metering Infrastructure,” *IEEE Trans. Instrum. Meas.*, vol. 68, no. 11, pp. 4300–4312, Nov. 2019, doi: 10.1109/TIM.2018.2890399.

[31] A. A. M. Raposo, A. B. Rodrigues, and M. da Guia da Silva, "Robust meter placement for state estimation considering Distribution Network Reconfiguration for annual energy loss reduction," *Electr. Power Syst. Res.*, vol. 182, p. 106233, May 2020, doi: 10.1016/j.epsr.2020.106233.

[32] A. Al-Wakeel, J. Wu, and N. Jenkins, "State estimation of medium voltage distribution networks using smart meter measurements," *Appl. Energy*, vol. 184, pp. 207–218, Dec. 2016, doi: 10.1016/j.apenergy.2016.10.010.

[33] C. Muscas, M. Pau, P. A. Pegoraro, and S. Sulis, "Uncertainty of Voltage Profile in PMU-Based Distribution System State Estimation," *IEEE Trans. Instrum. Meas.*, vol. 65, no. 5, pp. 988–998, May 2016, doi: 10.1109/TIM.2015.2494619.

[34] N. G. Bretas and J. B. A. London, "Recovering of masked errors in power systems state estimation and measurement gross error detection and identification proposition," in *IEEE PES General Meeting*, Jul. 2010, pp. 1–6. doi: 10.1109/PES.2010.5589577.

[35] M. Asprou, E. Kyriakides, and M. Albu, "The Effect of Variable Weights in a WLS State Estimator Considering Instrument Transformer Uncertainties," *IEEE Trans. Instrum. Meas.*, vol. 63, no. 6, pp. 1484–1495, Jun. 2014, doi: 10.1109/TIM.2013.2292138.

[36] "EN 61869-1:2009 Instrument transformers - Part 1: General requirements," CENELEC, Brussels, 2009.

[37] G. Pasini, "Appunti di Misure Elettriche," 2014.

[38] B. A. Gregory, *An Introduction to Electrical Instrumentation and Measurement Systems*, 2nd ed. Macmillan, 1985.

[39] "EN 61869-2:2012 Instrument transformers - Part 2: Additional requirements for current transformers," CENELEC, Brussels, 2012.

[40] "EN 61869-3:2011 Instrument transformers - Part 3: Additional requirements for inductive voltage transformers," CENELEC, Brussels, 2011.

[41] Q. Sun *et al.*, "A Comprehensive Review of Smart Energy Meters in Intelligent Energy Networks," *IEEE Internet Things J.*, vol. 3, no. 4, pp. 464–479, Aug. 2016, doi: 10.1109/JIOT.2015.2512325.

[42] "PD IEC/TR 61850-1:2013 Communication networks and systems for power utility automation - Part 1: Introduction and overview," IEC, 2013.

[43] "IEEE/IEC International Standard - Measuring relays and protection equipment - Part 118-1: Synchrophasor for power systems - Measurements," *IECIEEE 60255-118-12018*, pp. 1–78, Dec. 2018, doi: 10.1109/IEEESTD.2018.8577045.

[44] A. Monti, C. Muscas, and F. Ponci, *Phasor Measurement Units and Wide Area Monitoring Systems*. Academic Press, 2016.

[45] "JCGM 200:2012 International vocabulary of metrology-Basic and general concepts and associated terms (VIM) 3rd edition 2008 version with minor corrections," BIPM, 2012. [Online]. Available: https://www.ceinorme.it/en/normazione-en/vim-en/vim-content-en.html?

[46] A. Ferrero, D. Petri, P. Carbone, and M. Catelani, *Modern Measurements Fundamentals and Applications*. Wiley-IEEE Press, 2015.

[47] "JCGM 100:2008 Evaluation of measurement data - Guide to the expression of uncertainty in measurement (GUM)," BIPM, 2008. [Online]. Available: http://www.bipm.org/en/publications/guides/gum.html

[48] "JCGM 101:2008 Evaluation of measurement data – Supplement 1 to the 'Guide to the expression of uncertainty in measurement' – Propagation of distributions using a Monte Carlo method," BIPM, 2008. [Online]. Available: http://www.bipm.org/en/publications/guides/gum.html

[49] D. Cavaliere, A. Mingotti, G. Pasini, L. Peretto, and R. Tinarelli, “MV surge arresters monitoring using drone technology,” in *2019 IMEKO TC4 International Symposium Electrical and Electronic Measurements Promote Industry 4.0*, 2019, pp. 140–145.

[50] T. Taskin, “Introduction of a measurement system to monitor the condition of ZnO surge arresters,” in *2000 IEEE Power Engineering Society Winter Meeting. Conference Proceedings (Cat. No.00CH37077)*, Jan. 2000, vol. 3, pp. 1553–1557 vol.3. doi: 10.1109/PESW.2000.847573.

[51] S. M. Arshad and Asanka. S. Rodrigo, “Modified Phase Shifting of Leakage Current to Condition Monitoring of Metal Oxide Surge Arresters in Power System,” in *2018 Moratuwa Engineering Research Conference (MERCon)*, May 2018, pp. 300–305. doi: 10.1109/MERCon.2018.8421967.

[52] Z. Abdul-Malek, N. Yusoff, and M. F. Mohd Yousof, “Field experience on surge arrester condition monitoring - Modified Shifted Current Method,” in *45th International Universities Power Engineering Conference UPEC2010*, Aug. 2010, pp. 1–5.

[53] H. Kayan, R. Eslampanah, F. Yeganli, and M. Askar, “Heat leakage detection and surveiallance using aerial thermography drone,” in *2018 26th Signal Processing and Communications Applications Conference (SIU)*, May 2018, pp. 1–4. doi: 10.1109/SIU.2018.8404366.

[54] Novizon and Z. Abdul-Malek, “Electrical and temperature correlation to monitor fault condition of ZnO surge arrester,” in *2016 3rd International Conference on Information Technology, Computer, and Electrical Engineering (ICITACEE)*, Oct. 2016, pp. 182–186. doi: 10.1109/ICITACEE.2016.7892436.

[55] L. Bartolomei *et al.*, “Performance evaluation of an energy meter for low-voltage system monitoring,” *J. Phys. Conf. Ser.*, vol. 1065, p. 052032, Aug. 2018, doi: 10.1088/1742-6596/1065/5/052032.

[56] P. Daponte, L. De Vito, G. Mazzilli, F. Picariello, S. Rapuano, and M. Riccio, “Metrology for drone and drone for metrology: Measurement systems on small civilian drones,” in *2015 IEEE Metrology for Aerospace (MetroAeroSpace)*, Jun. 2015, pp. 306–311. doi: 10.1109/MetroAeroSpace.2015.7180673.

[57] F. N. Murrieta-Rico *et al.*, “Resolution improvement of accelerometers measurement for drones in agricultural applications,” in *IECON 2016 - 42nd Annual Conference of the IEEE Industrial Electronics Society*, Oct. 2016, pp. 1037–1042. doi: 10.1109/IECON.2016.7793466.

[58] J. Baeza, D. Valencia, and A. Baeza, “Use of Drones for Remote Management of the Close Measure of Radioactivity Sources,” in *IGARSS 2018 - 2018 IEEE International Geoscience and Remote Sensing Symposium*, Jul. 2018, pp. 7914–7917. doi: 10.1109/IGARSS.2018.8518180.

[59] S. S. Altman, V. Vulfin, H. Leibovich, R. Heinrich, and R. Ianconescu, “Lighting strike analysis for drones,” in *2017 IEEE International Conference on Microwaves, Antennas, Communications and Electronic Systems (COMCAS)*, Nov. 2017, pp. 1–4. doi: 10.1109/COMCAS.2017.8244806.

[60] O. B. A. Seller and N. Sornin, “Low power long range transmitter,” EP2763321B1, Apr. 08, 2020 Accessed: Sep. 15, 2021. [Online]. Available: https://patents.google.com/patent/EP2763321B1/de?oq=EP2763321

[61] C. A. Hornbuckle, “Fractional-N synthesized chirp generator,” US7791415B2, Sep. 07, 2010 Accessed: Sep. 15, 2021. [Online]. Available: https://patents.google.com/patent/US7791415B2/en?oq=US7791415B2

[62] Y. Qianjun, W. Guichu, Y. Fenqun, and X. Hongyan, “Design and applications of intelligent low voltage distribution system based on ZigBee,” in *2011 International Conference on Electronics, Communications and Control (ICECC)*, Sep. 2011, pp. 791–794. doi: 10.1109/ICECC.2011.6066383.

[63] A. Löf, S. Repo, M. Pikkarainen, S. Lu, and T. Pöhö, “Low voltage network monitoring in RTDS environment,” in *IEEE PES ISGT Europe 2013*, Oct. 2013, pp. 1–5. doi: 10.1109/ISGTEurope.2013.6695459.

[64] S. Lu, S. Repo, D. D. Giustina, F. A.-C. Figuerola, A. Löf, and M. Pikkarainen, "Real-Time Low Voltage Network Monitoring—ICT Architecture and Field Test Experience," *IEEE Trans. Smart Grid*, vol. 6, no. 4, pp. 2002–2012, Jul. 2015, doi: 10.1109/TSG.2014.2371853.

[65] R. Sanchez, F. Iov, M. Kemal, M. Stefan, and R. Olsen, "Observability of low voltage grids: Actual DSOs challenges and research questions," in *2017 52nd International Universities Power Engineering Conference (UPEC)*, Aug. 2017, pp. 1–6. doi: 10.1109/UPEC.2017.8232008.

[66] A. Mingotti, L. Peretto, and R. Tinarelli, "An Equivalent Synchronization for Phasor Measurements in Power Networks," in *2017 IEEE International Workshop on Applied Measurements for Power Systems (AMPS)*, Sep. 2017, pp. 1–5. doi: 10.1109/AMPS.2017.8078338.

[67] A. Mingotti, L. Peretto, and R. Tinarelli, "A novel equivalent power network impedance approach for assessing the time reference in asynchronous measurements," in *2017 IEEE International Instrumentation and Measurement Technology Conference (I2MTC)*, May 2017, pp. 1–6. doi: 10.1109/I2MTC.2017.7969760.

[68] S. Nasrollahi, A. Sardarabadi, Y. Khoshian, and A. Gharib, "A novel hybrid algorithm for reconfiguration problem of the distribution networks," in *22nd International Conference and Exhibition on Electricity Distribution (CIRED 2013)*, Jun. 2013, pp. 1–4. doi: 10.1049/cp.2013.1226.

[69] Y. Liu, Z. Wang, X. Meng, and W. Sheng, "Distribution network planning considering distributed generations based on genetic algorithm," in *2011 IEEE Power Engineering and Automation Conference*, Sep. 2011, vol. 3, pp. 42–45. doi: 10.1109/PEAM.2011.6135041.

[70] J. Zhang, T. Huang, and H. Zhang, "The Reactive Power Optimization of Distribution Network Based on an Improved Genetic Algorithm," in *2005 IEEE/PES Transmission Distribution Conference Exposition: Asia and Pacific*, Aug. 2005, pp. 1–4. doi: 10.1109/TDC.2005.1546960.

[71] A. Ferrero, M. Faifer, and S. Salicone, "On Testing the Electronic Revenue Energy Meters," *IEEE Trans. Instrum. Meas.*, vol. 58, no. 9, pp. 3042–3049, Sep. 2009, doi: 10.1109/TIM.2009.2016821.

[72] R. Q. Cetina, A. J. Roscoe, and P. S. Wright, "A review of electrical metering accuracy standards in the context of dynamic power quality conditions of the grid," in *2017 52nd International Universities Power Engineering Conference (UPEC)*, Aug. 2017, pp. 1–5. doi: 10.1109/UPEC.2017.8231871.

[73] A. Ferrero, L. Peretto, and R. Sasdelli, "Revenue metering in the presence of distortion and unbalance: myths and reality," in *8th International Conference on Harmonics and Quality of Power. Proceedings (Cat. No.98EX227)*, Oct. 1998, vol. 1, pp. 42–47 vol.1. doi: 10.1109/ICHQP.1998.759837.

[74] A. Bernieri, G. Betta, L. Ferrigno, and M. Laracca, "Electrical energy metering in compliance with recent european standards," in *2012 IEEE International Instrumentation and Measurement Technology Conference Proceedings*, May 2012, pp. 1541–1545. doi: 10.1109/I2MTC.2012.6229455.

[75] J. Novotny, J. Drapela, and D. Topolanek, "Frequency response of revenue meters in measured active energy," in *2016 17th International Conference on Harmonics and Quality of Power (ICHQP)*, Oct. 2016, pp. 524–529. doi: 10.1109/ICHQP.2016.7783309.

[76] A. Delle Femine, D. Gallo, C. Landi, and M. Luiso, "Advanced Instrument For Field Calibration of Electrical Energy Meters," *IEEE Trans. Instrum. Meas.*, vol. 58, no. 3, pp. 618–625, Mar. 2009, doi: 10.1109/TIM.2008.2005079.

[77] A. Cataliotti, V. Cosentino, and S. Nuccio, "Static Meters for the Reactive Energy in the Presence of Harmonics: An Experimental Metrological Characterization," *IEEE Trans. Instrum. Meas.*, vol. 58, no. 8, pp. 2574–2579, Aug. 2009, doi: 10.1109/TIM.2009.2015633.

[78] A. Cataliotti, V. Cosentino, A. Lipari, and S. Nuccio, "Metrological Characterization and Operating Principle Identification of Static Meters for Reactive Energy: An Experimental Approach Under

Nonsinusoidal Test Conditions," *IEEE Trans. Instrum. Meas.*, vol. 58, no. 5, pp. 1427–1435, May 2009, doi: 10.1109/TIM.2008.2009134.

[79] D. Gallo, C. Landi, N. Pasquino, and N. Polese, "A New Methodological Approach to Quality Assurance of Energy Meters Under Nonsinusoidal Conditions," *IEEE Trans. Instrum. Meas.*, vol. 56, no. 5, pp. 1694–1702, Oct. 2007, doi: 10.1109/TIM.2007.903607.

[80] D. Georgakopoulos and P. S. Wright, "Calibration of energy and power meters under non-sinusoidal conditions," *IEE Proc. - Sci. Meas. Technol.*, vol. 153, no. 6, pp. 241–247, Nov. 2006.

[81] D. Gallo, C. Landi, R. Langella, and A. Testa, "On the Accuracy of Electric Energy Revenue Meter Chain Under Non-Sinusoidal Conditions: A Modeling Based Approach," in *2007 IEEE Instrumentation Measurement Technology Conference IMTC 2007*, May 2007, pp. 1–6. doi: 10.1109/IMTC.2007.379101.

[82] A. Mingotti, L. Peretto, R. Tinarelli, and J. Zhang, "Use of COMTRADE Fault Current Data to Test Inductive Current Transformers," in *2019 II Workshop on Metrology for Industry 4.0 and IoT (MetroInd4.0 IoT)*, Jun. 2019, pp. 103–107. doi: 10.1109/METROI4.2019.8792871.

[83] G. Rietveld *et al.*, "Performance evaluation of HV CTs subjected to actual operating conditions in substations and its impact on smart metering infrastructure within smart grids," in *2012 IEEE Power and Energy Society General Meeting*, Jul. 2012, pp. 1–2. doi: 10.1109/PESGM.2012.6345031.

[84] E. So, R. Arseneau, D. Bennett, and M. Frigault, "A current-comparator-based system for calibrating high voltage conventional and non-conventional current transformers under actual operating conditions of high voltage and distorted current waveforms up to 100 kV and 2000 A," in *CPEM 2010*, Jun. 2010, pp. 561–562. doi: 10.1109/CPEM.2010.5544830.

[85] G. Mahesh, B. George, V. Jayashankar, and V. J. Kumar, "Instrument transformer performance under distorted-conditions," in *Proceedings of the IEEE INDICON 2004. First India Annual Conference, 2004.*, Dec. 2004, pp. 468–471. doi: 10.1109/INDICO.2004.1497797.

[86] T. Lei *et al.*, "Behavior of voltage transformers under distorted conditions," in *2016 IEEE International Instrumentation and Measurement Technology Conference Proceedings*, May 2016, pp. 1–6. doi: 10.1109/I2MTC.2016.7520344.

[87] L. Bartolomei, D. Cavaliere, A. Mingott, L. Peretto, and R. Tinarelli, "Testing of Electrical Energy Meters in Off-Nominal Frequency Conditions," in *2019 IEEE 10th International Workshop on Applied Measurements for Power Systems (AMPS)*, Sep. 2019, pp. 1–6. doi: 10.1109/AMPS.2019.8897781.

[88] L. Bartolomei, D. Cavaliere, A. Mingotti, L. Peretto, and R. Tinarelli, "Testing of electrical energy meters subject to realistic distorted voltages and currents," *Energies*, vol. 13, no. 8, 2020, doi: 10.3390/en13082023.

[89] e-distribuzione S.p.A., "Dichiarazione di conformità alla direttiva 2014/53/UE 'RED.'" Jun. 2017. Accessed: Nov. 03, 2021. [Online]. Available: https://www.e-distribuzione.it/content/dam/e-distribuzione/documenti/open-meter/dichiarazione_conformit%C3%A0/Dichiarazione_conformit%C3%A0_Direttiva_Europa2014_53_UE_Direttiva_RED.pdf

[90] "European Directive 2014/32/EU on Measuring Instruments (MID)," European Parliament and of the Council, 2014.

[91] "EN 50470-1:2006+A1:2018 'Electricity metering equipment (a.c.). Part 1: General requirements, tests and test conditions - Metering equipment (class indexes A, B and C),'" CENELEC, 2019.

[92] "EN 50470-2:2006+A1:2018 'Electricity metering equipment (a.c.). Part 2: Particular requirements - Electromechanical meters for active energy (class indexes A and B),'" CENELEC, 2019.

[93]"EN 50470-3:2006+A1:2018 'Electricity metering equipment (a.c.). Part 3: Particular requirements - Static meters for active energy (class indexes A, B and C),'" CENELEC, 2019.

[94]"IEC 62052-11:2003+A1:2017 Electricity metering equipment (AC). General requirements, tests and test conditions. Part 11: Metering equipment," IEC, 2017.

[95]"IEC 62053-21:2003+A1:2017 'Electricity metering equipment (a.c.). Particular requirements. Part 21: Static meters for active energy (classes 1 and 2),'" IEC, 2018.

[96]"IEC 62053-22:2003+A1:2017 'Electricity metering equipment (a.c.). Particular requirements. Part 22: Static meters for active energy (classes 0,2 S and 0,5 S),'" IEC, 2018.

[97]"IEC 62053-31:1998 'Electricity metering equipment (a.c.). Particular requirements. Part 31: Pulse output devices for electromechanical and electronic meters (two wires only),'" IEC, 1998.

[98]"IEC/TR 61869-103:2012 'Instrument transformers – The use of instrument transformers for power quality measurements.,'" IEC, Geneva, 2012.

[99]M. Kaczmarek and E. Stano, "Proposal for extension of routine tests of the inductive current transformers to evaluation of transformation accuracy of higher harmonics," *Int. J. Electr. Power Energy Syst.*, vol. 113, pp. 842–849, Dec. 2019, doi: 10.1016/j.ijepes.2019.06.034.

[100] L. Cristaldi, M. Faifer, C. Laurano, R. Ottoboni, S. Toscani, and M. Zanoni, "A Low-Cost Generator for Testing and Calibrating Current Transformers," *IEEE Trans. Instrum. Meas.*, vol. 68, no. 8, pp. 2792–2799, Aug. 2019, doi: 10.1109/TIM.2018.2870264.

[101] A. J. Collin, A. D. Femine, D. Gallo, R. Langella, and M. Luiso, "Compensation of Current Transformers' Nonlinearities by Tensor Linearization," *IEEE Trans. Instrum. Meas.*, vol. 68, no. 10, pp. 3841–3849, Oct. 2019, doi: 10.1109/TIM.2019.2905908.

[102] M. S. Ballal, M. G. Wath, and H. M. Suryawanshi, "A Novel Approach for the Error Correction of CT in the Presence of Harmonic Distortion," *IEEE Trans. Instrum. Meas.*, vol. 68, no. 10, pp. 4015–4027, Oct. 2019, doi: 10.1109/TIM.2018.2884575.

[103] C. Laurano, S. Toscani, and M. Zanoni, "Improving the Accuracy of Current Transformers through Harmonic Distortion Compensation," in *2019 IEEE International Instrumentation and Measurement Technology Conference (I2MTC)*, May 2019, pp. 1–6. doi: 10.1109/I2MTC.2019.8826877.

[104] A. Cataliotti *et al.*, "Compensation of Nonlinearity of Voltage and Current Instrument Transformers," *IEEE Trans. Instrum. Meas.*, vol. 68, no. 5, pp. 1322–1332, May 2019, doi: 10.1109/TIM.2018.2880060.

[105] S. Wu, Q. Xu, and Y. Huang, "Research on Harmonic Error Characteristics of Electromagnetic Current Transformers," in *2019 2nd Asia Conference on Energy and Environment Engineering (ACEEE)*, Jun. 2019, pp. 59–63. doi: 10.1109/ACEEE.2019.8816925.

[106] A. E. Emanuel and J. A. Orr, "Current Harmonics Measurement by Means of Current Transformers," *IEEE Trans. Power Deliv.*, vol. 22, no. 3, pp. 1318–1325, Jul. 2007, doi: 10.1109/TPWRD.2007.900108.

[107] G. Crotti *et al.*, "Calibration of Current Transformers in distorted conditions," *J. Phys.: Conf. Ser.*, vol. 1065, p. 052033, Aug. 2018, doi: 10.1088/1742-6596/1065/5/052033.

[108] A. Mingotti, L. Peretto, L. Bartolomei, D. Cavaliere, and R. Tinarelli, "Are inductive current transformers performance really affected by actual distorted network conditions? An experimental case study," *Sens. Switz.*, vol. 20, no. 3, 2020, doi: 10.3390/s20030927.

[109] A. Mingotti, D. Cavaliere, L. Peretto, and R. Tinarelli, "THD uncertainty estimation for inductive current transformers using the accuracy class information," in *24th IMEKO TC4 International Symposium and 22nd International Workshop on ADC and DAC Modelling and Testing*, 2020, pp. 39–43.

[110] M. Brehm, D. Slomovitz, A. Santos, G. Aristoy, and L. Trigo, “Modeling capacitive voltage transformers for distorted waveforms measurements,” in *2016 IEEE PES Transmission Distribution Conference and Exposition-Latin America (PES T D-LA)*, Sep. 2016, pp. 1–5. doi: 10.1109/TDC-LA.2016.7805662.

[111] G. Aristoy, L. Trigo, A. Santos, M. Brehm, and D. Slomovitz, “Measuring system for calibrating high voltage instrument transformers at distorted waveforms,” in *2016 Conference on Precision Electromagnetic Measurements (CPEM 2016)*, Jul. 2016, pp. 1–2. doi: 10.1109/CPEM.2016.7540742.

[112] D. W. Ackermann, “Current transformer measurements of distorted current waveforms with secondary load impedance,” in *1999 IEEE Africon. 5th Africon Conference in Africa (Cat. No.99CH36342)*, Sep. 1999, vol. 2, pp. 765–768 vol.2. doi: 10.1109/AFRCON.1999.821864.

[113] M. Kaczmarek, “A practical approach to evaluation of accuracy of inductive current transformer for transformation of distorted current higher harmonics,” *Electr. Power Syst. Res.*, vol. 119, pp. 258–265, Feb. 2015, doi: 10.1016/j.epsr.2014.10.009.

[114] N. Locci and C. Muscas, “Comparative analysis between active and passive current transducers in sinusoidal and distorted conditions,” *IEEE Trans. Instrum. Meas.*, vol. 50, no. 1, pp. 123–128, Feb. 2001, doi: 10.1109/19.903889.

[115] R. Sasdelli, C. Muscas, L. Peretto, and R. Tinarelli, “On the characterization of voltage and current transducers in steady-state distorted conditions,” *ETEP Eur. Trans. Electr. Power*, vol. 11, no. 6, pp. 365–370, Dec. 2001.

[116] A. Mingotti, L. Peretto, and R. Tinarelli, “A Closed-form Expression to Estimate the Uncertainty of THD Starting from the LPIT Accuracy Class,” *Sensors*, vol. 20, no. 6, Art. no. 6, Jan. 2020, doi: 10.3390/s20061804.

[117] “EN 61869-6:2016 Instrument transformers - Part 6: Additional general requirements for low-power instrument transformers,” CENELEC, Brussels, 2016.

[118] National Instrument, “NI 9238.” 2016. [Online]. Available: https://www.ni.com/pdf/manuals/376138a_02.pdf

[119] A. Mingotti, F. Costa, D. Cavaliere, L. Peretto, and R. Tinarelli, “On the Importance of Characterizing Virtual PMUs for Hardware-in-the-Loop and Digital Twin Applications,” *Sensors*, vol. 21, no. 18:6133, 2021, doi: 10.3390/s21186133.

[120] M. Stifter, J. Cordova, J. Kazmi, and R. Arghandeh, “Real-Time Simulation and Hardware-in-the-Loop Testbed for Distribution Synchrophasor Applications,” *Energies*, vol. 11, no. 4, Art. no. 4, Apr. 2018, doi: 10.3390/en11040876.

[121] F. Quintero-Zuluaga *et al.*, “Hardware in the Loop Design and Testing of a PMU-Based Special Protection Scheme: Case Study of Colombia-Ecuador Interconnection,” in *2020 IEEE PES Transmission Distribution Conference and Exhibition - Latin America (T D LA)*, Sep. 2020, pp. 1–6. doi: 10.1109/TDLA47668.2020.9326098.

[122] A. T. Al-Hammouri, L. Nordström, M. Chenine, L. Vanfretti, N. Honeth, and R. Leelaruji, “Virtualization of synchronized phasor measurement units within real-time simulators for smart grid applications,” in *2012 IEEE Power and Energy Society General Meeting*, Jul. 2012, pp. 1–7. doi: 10.1109/PESGM.2012.6344949.

[123] G. Frigo, A. Derviškadić, Y. Zuo, A. Bach, and M. Paolone, “Taylor-Fourier PMU on a Real-Time Simulator: Design, Implementation and Characterization,” in *2019 IEEE Milan PowerTech*, Jun. 2019, pp. 1–6. doi: 10.1109/PTC.2019.8810660.

[124] M. M. Amin, “Experimental Validation of High Performance HIL-based Real-time PMU Model for WAMS,” in *2019 IEEE Industry Applications Society Annual Meeting*, Sep. 2019, pp. 1–8. doi: 10.1109/IAS.2019.8912441.

[125] Q. Xu, P. Li, Z. Yuan, and L. Yu, “Comprehensive and Adaptive Synchrophasor Estimator and Hardware-in-Loop Test,” in *2019 IEEE Sustainable Power and Energy Conference (iSPEC)*, Nov. 2019, pp. 1321–1326. doi: 10.1109/iSPEC48194.2019.8975216.

[126] Y. Gao *et al.*, “Development of a Hardware in-the-Loop Co-Simulation Platform for Smart Distribution Networks,” in *2020 Fifteenth International Conference on Ecological Vehicles and Renewable Energies (EVER)*, Sep. 2020, pp. 1–10. doi: 10.1109/EVER48776.2020.9243051.

[127] J. Ihrens, S. Möws, L. Wilkening, T. A. Kern, and C. Becker, “The Impact of Time Delays for Power Hardware-in-the-Loop Investigations,” *Energies*, vol. 14, no. 11, Art. no. 11, Jan. 2021, doi: 10.3390/en14113154.

[128] G. Barchi, D. Macii, and D. Petri, “Synchrophasor Estimators Accuracy: A Comparative Analysis,” *IEEE Trans. Instrum. Meas.*, vol. 62, no. 5, pp. 963–973, May 2013, doi: 10.1109/TIM.2012.2236776.

[129] G. Frigo, D. Colangelo, A. Derviškadić, M. Pignati, C. Narduzzi, and M. Paolone, “Definition of Accurate Reference Synchrophasors for Static and Dynamic Characterization of PMUs,” *IEEE Trans. Instrum. Meas.*, vol. 66, no. 9, pp. 2233–2246, Sep. 2017, doi: 10.1109/TIM.2017.2698709.

[130] C. Qian and M. Kezunovic, “Synchrophasor reference algorithm for PMU Calibration System,” in *2016 IEEE/PES Transmission and Distribution Conference and Exposition (T D)*, May 2016, pp. 1–5. doi: 10.1109/TDC.2016.7520024.

[131] S. Xu, H. Liu, T. Bi, and K. E. Martin, “A High-Accuracy Phasor Estimation Algorithm for PMU Calibration and Its Hardware Implementation,” *IEEE Trans. Smart Grid*, vol. 11, no. 4, pp. 3372–3383, Jul. 2020, doi: 10.1109/TSG.2020.2965195.

[132] D. Colangelo *et al.*, “Architecture and characterization of a calibrator for PMUs operating in power distribution systems,” in *2015 IEEE Eindhoven PowerTech*, Jun. 2015, pp. 1–6. doi: 10.1109/PTC.2015.7232792.

[133] G. Frigo, A. Derviškadić, D. Colangelo, J. P. Braun, and M. Paolone, “Characterization of uncertainty contributions in a high-accuracy PMU validation system,” *Measurement*, vol. 146, pp. 72–86, Nov. 2019, doi: 10.1016/j.measurement.2019.06.013.

[134] R. Meyur, G. N. Stenbakken, and V. Centeno, “A LabVIEW based test system to characterize phasor measurement units,” in *2017 North American Power Symposium (NAPS)*, Sep. 2017, pp. 1–6. doi: 10.1109/NAPS.2017.8107185.

[135] Y. Tang, G. N. Stenbakken, and A. Goldstein, “Calibration of Phasor Measurement Unit at NIST,” *IEEE Trans. Instrum. Meas.*, vol. 62, no. 6, pp. 1417–1422, Jun. 2013, doi: 10.1109/TIM.2013.2240951.

[136] J.-P. Braun and C. Mester, “Reference grade calibrator for the testing of the dynamic behavior of phasor measurement units,” in *2012 Conference on Precision electromagnetic Measurements*, Jul. 2012, pp. 410–411. doi: 10.1109/CPEM.2012.6250977.

[137] D. Colangelo, D. Hoogenboom, E. Dierikx, G. Rietveld, and G. Frigo, “Metrological characterization of a PMU calibrator in the 25 Hz to 3 kHz range,” in *2017 IEEE Manchester PowerTech*, Jun. 2017, pp. 1–6. doi: 10.1109/PTC.2017.7981109.

[138] D. Georgakopoulos and S. Quigg, “Precision Measurement System for the Calibration of Phasor Measurement Units,” *IEEE Trans. Instrum. Meas.*, vol. 66, no. 6, pp. 1441–1445, Jun. 2017, doi: 10.1109/TIM.2017.2653518.

[139] B. Trinchera, D. Serazio, and U. Pogliano, “Asynchronous Phase Comparator for Characterization of Devices for PMUs Calibrator,” *IEEE Trans. Instrum. Meas.*, vol. 66, no. 6, pp. 1139–1145, Jun. 2017, doi: 10.1109/TIM.2017.2648598.

[140] P. Castello, C. Muscas, P. A. Pegoraro, S. Sulis, and S. Toscani, “Experimental characterization of dynamic methods for synchrophasor measurements,” in *2014 IEEE International Workshop on Applied Measurements for Power Systems Proceedings (AMPS)*, Sep. 2014, pp. 1–6. doi: 10.1109/AMPS.2014.6947709.

[141] M. S. Almas, J. Kilter, and L. Vanfretti, “Experiences with steady-state PMU compliance testing using standard relay testing equipment,” in *2014 Electric Power Quality and Supply Reliability Conference (PQ)*, Jun. 2014, pp. 103–110. doi: 10.1109/PQ.2014.6866793.

[142] M. Luiso, D. Macii, P. Tosato, D. Brunelli, D. Gallo, and C. Landi, “A Low-Voltage Measurement Testbed for Metrological Characterization of Algorithms for Phasor Measurement Units,” *IEEE Trans. Instrum. Meas.*, vol. 67, no. 10, pp. 2420–2433, Oct. 2018, doi: 10.1109/TIM.2018.2852940.

[143] Trimble, “Trimble Thunderbolt E Disciplined Clock.” 2011. [Online]. Available: https://timing.trimble.com/wp-content/uploads/thunderbolt-e-gps-disciplined-clock-datasheet.pdf

[144] National Instrument, “NI USB-6346.” 2019. [Online]. Available: https://www.ni.com/pdf/manuals/377316d.pdf

[145] Keysight Technologies, “3458A.” [Online]. Available: https://www.keysight.com/it/en/assets/7018-06796/data-sheets/5965-4971.pdf

[146] Tektronix, “5 Series Mixed Signal Oscilloscope.” [Online]. Available: https://www.tek.com/datasheet/5-series-mso

[147] D. Belega and D. Petri, “Accuracy Analysis of the Multicycle Synchrophasor Estimator Provided by the Interpolated DFT Algorithm,” *IEEE Trans. Instrum. Meas.*, vol. 62, no. 5, pp. 942–953, May 2013, doi: 10.1109/TIM.2012.2236777.

[148] T. Jin and W. Zhang, “A Novel Interpolated DFT Synchrophasor Estimation Algorithm With an Optimized Combined Cosine Self-Convolution Window,” *IEEE Trans. Instrum. Meas.*, vol. 70, pp. 1–10, 2021, doi: 10.1109/TIM.2020.3033073.

[149] T. Bi, H. Liu, Q. Feng, C. Qian, and Y. Liu, “Dynamic Phasor Model-Based Synchrophasor Estimation Algorithm for M-Class PMU,” *IEEE Trans. Power Deliv.*, vol. 30, no. 3, pp. 1162–1171, Jun. 2015, doi: 10.1109/TPWRD.2014.2353816.

[150] Y. Seferi, R. G. Q. Cetina, and S. M. Blair, “Review of PMU Algorithms Suitable for Real-Time Operation With Digital Sampled Value Data,” in *2021 IEEE 11th International Workshop on Applied Measurements for Power Systems (AMPS)*, Sep. 2021, pp. 1–6. doi: 10.1109/AMPS50177.2021.9586034.

[151] I. Kamwa, S. R. Samantaray, and G. Joos, “Wide Frequency Range Adaptive Phasor and Frequency PMU Algorithms,” *IEEE Trans. Smart Grid*, vol. 5, no. 2, pp. 569–579, Mar. 2014, doi: 10.1109/TSG.2013.2264536.

[152] S. Xu, H. Liu, T. Bi, and K. E. Martin, “An improved Taylor weighted least squares method for estimating synchrophasor,” *Int. J. Electr. Power Energy Syst.*, vol. 120, p. 105987, Sep. 2020, doi: 10.1016/j.ijepes.2020.105987.

[153] S. Toscani, C. Muscas, and P. A. Pegoraro, “Design and Performance Prediction of Space Vector-Based PMU Algorithms,” *IEEE Trans. Instrum. Meas.*, vol. 66, no. 3, pp. 394–404, Mar. 2017, doi: 10.1109/TIM.2016.2636438.

[154] C. Qian and M. Kezunovic, “A Power Waveform Classification Method for Adaptive Synchrophasor Estimation,” *IEEE Trans. Instrum. Meas.*, vol. 67, no. 7, pp. 1646–1658, Jul. 2018, doi: 10.1109/TIM.2018.2803938.

[155] Y. Amirat, Z. Oubrahim, H. Ahmed, M. Benbouzid, and T. Wang, “Phasor Estimation for Grid Power Monitoring: Least Square vs. Linear Kalman Filter,” *Energies*, vol. 13, no. 10, Art. no. 10, Jan. 2020, doi: 10.3390/en13102456.